Coronal and transition region intensities as seen in 3d numerical models and from Hinode/EIS

Kosovare Olluri
Master's thesis
Institute of Theoretical Astrophysics
University of Oslo
Norway

June 2008

Acknowledgments

First of all I would like to thank my supervisor Viggo Hansteen for great guidance over the past year in the progress of this thesis. Thank you very much for taking me to Japan and giving me an opportunity to observe with the Hinode satellite. I am very grateful for all the help and encouragement you have given me.
I also would like to thank my co-supervisor Mats Carlsson for giving me the opportunity to work with SOT data during the summer of 2007.
Thanks to Øystein Langangen for taking me to The Swedish Solar Telescope in august 2007 and getting me involved in observational astronomy. Thanks for all the answers to my silly questions. This thanks goes to Juan Martinez Sykora as well.
I would also like to thank all the people around Fysikkforeningen for giving me unforgettable memories over the last five years. Thank to all the people at stjernekjelleren for all the chats and laughs over the last 2 years. Especially I would like to thank my dear friends Thomas, Lillian, Gunn and Eirik for proof reading my thesis and for being there for me when I needed it the most. It meant the world to me.

Most of all I thank my parents, Selman and Shpresa Olluri, for encouraging me to carry on with these studies. Thanks to my sisters and my brother for making me think about other things than physics once in a while.

Finally,
thanks to Egil Leer and Tore Sandnes for all the inspiration!

Kosovare Olluri
June 2008

Contents

Chapter 1

Introduction

The nearest star, and the star for which we have the greatest amount of observational data is our Sun. By examining the layers of the solar atmosphere we can test theoretical models of stellar dynamics. It is our understanding of the Sun itself that will validate our picture of the relationship between stellar activity and other stellar parameters. With ground based and space based observatories we are able to measure with high precision the exterior composition of the Suns surface. With observations of its luminosity and effective temperature we can classify the sun as a typical main sequence star of spectral type G2 V. Observations of other main sequence stars show that they are similar to the Sun. If we understand the detailed structure and energy balance of the Sun, then we understand the same structures in other main sequence stars.

At present the Sun is being investigated by the Hinode satellite. This Japanese satellite, launched in September 2006, has as its main goal to figure out the the connection between the different layers of the solar atmosphere; photosphere, chromosphere, transition region and corona.

During the last decade a three dimensional numerical model has been developed at the Institute for Theoretical Astrophysics, where for the first time models comprising the entire solar atmosphere; from convection zone to corona, can be constructed.

The conjunction of these two developments puts us in a unique opportunity to compare the observations of Hinode with synthetic observations from the Oslo Stagger Code (OSC). The subject of this thesis lies in analysis of the similarities and differences between transition region and coronal intensities as predicted by the OSC and as observed by Hinode. This work should thus lead to insight into what elements of our understanding of the Sun are correct and which elements are lacking.

1.1 The sun and the solar atmosphere

As we move from the hot center of the Sun energy is carried by radiation. Eventually the density, pressure and temperature become low enough so convection can take over as the energy mechanism from the solar interior. Above the convection zone, which fills the outer third of the solar interior, lies the photosphere, from where we are able to observe the dynamics of the solar atmosphere. This point also marks the beginning of our research.

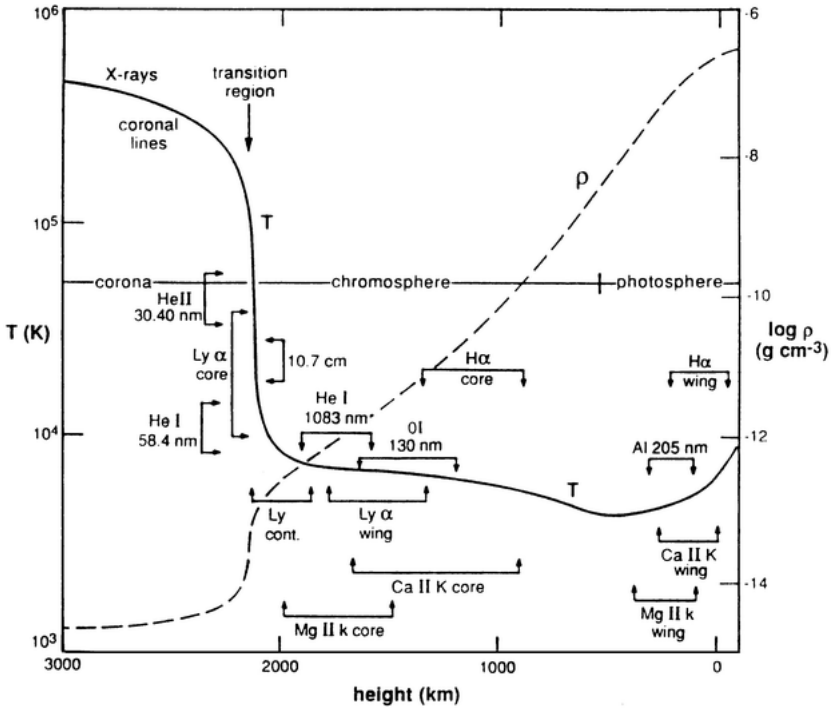

Figure 1.1: Logarithmic plot of the temperature and the density distribution in the solar atmosphere, [figure adapted from Ostlie and Carroll (2007)].

The photosphere shows a relatively homogeneous granular pattern of bright emission at visible wavelengths with typical horizontal scales of a thousand kilometers (1 Mm) or so. In addition to the upper, fading, granulation pattern, a larger horizontal pattern, with scales of order 20 Mm continues through the chromosphere forming what is known as the chromospheric network, which extends through most of the transition region. This network structure correlates well with the distribution of magnetic flux in the outer layers. Observations show magnetic flux concentrations beneath the network structures, in the photosphere. In addition, larger concentra-

tions of magnetic flux are observed in the photosphere.

Figure 1.1 shows a schematic description of the solar atmosphere. We define the photosphere to extend upward to the temperature minimum. In a purely radiative atmosphere the temperature would continue to fall beyond this minimum, but because of the presence of non-radiative energy and momentum deposition the temperature increases beyond this point. This temperature minimum is defined as the beginning of the chromosphere, which extends to the end of the temperature plateau seen in figure 1.1. It is followed by the transition region immediately after, given by the steep temperature curve in the figure. When the temperature is of order 1 MK the temperature gradient decreases as we have reached the corona.

The Sun has a effective temperature of 5770 K, viewed as a black body this gives a temperature peak at a wavelength of 5000Å. The visible emission from the Sun is therefore dominated by strong continuum emission. However, in the ultraviolet the continuum is reduced roughly by a factor of 10^5 and emission lines dominate the spectrum.

To cover the upper chromosphere, transition region and corona, we look at the emission lines formed at the corresponding temperatures. According to figure 1.1 this is temperatures above $\log T \sim 4.7$. With this in mind, we use the EUV Imaging Spectrometer (EIS) onboard Hinode to investigate the upper solar atmosphere emission. The selected observable lines are He II 256.320 Å ($\log T = 4.9$), Mg VI 269.000 Å ($\log T = 5.7$), Mg VI 269.800 Å ($\log T = 5.7$), Si VII 275.350 Å ($\log T = 5.8$), Fe VIII 185.250 Å ($\log T = 5.9$), Fe X 184.540 Å ($\log T = 6.0$), Fe X 190.040 Å ($\log T = 6.0$), Fe XII 195.120 Å ($\log T = 6.2$) and Fe XV 268.160 Å ($\log T = 6.3$).

1.2 The Hinode mission

The Hinode satellite was launched 22 September 2006 21:36 UT. The circular Sun-synchronous orbit of 680 km over the Earths day/night determinater allows near-continuous observation of the Sun.

The scientific aims of the Hinode mission are as follows (Culhane et al., 2007);

- Determine the mechanisms responsible for heating the corona in active regions and quiet Sun.
- Establish the mechanisms that cause transient phenomena e.g. flares, CMEs.
- Investigate processes for energy transfer from photosphere to corona.

The satellite carries three instruments, The Solar Optical Telescope (SOT), the X-Ray Telescope (XRT) and the EUV Imaging Spectrometer (EIS). All instruments onboard the satellite are designed to achieve these goals.

SOT

SOT consist of two main parts; the Optical Telescope Assembly (OAT) and its Focal Plane Package (FPP). The OAT is a 0.5 m diffraction-limited telescope, the largest solar optical instrument yet deployed in space. It has a wavelength coverage of 3870-6680 Å, making it capable of observing the photosphere and chromosphere.

The radiation is analyzed in the FPP, which has four optical paths: The Narrowband Filter Imager (NFI) which can compute the four Stokes parameters, magnetograms and dopplergrams. The Broadband Filter Imager (BFI) produce high spatial and temporal images and measures horizontal flow and temperature in the photosphere. The Spectro Polarimeter (SP) records polarization spectra for Stokes polarimetry. While the Correction Tracker (CT) is a image stabilization system, recording jitter in the solar features.

XRT

The X-Ray Telescope is a grazing incidence telescope. XRT images the solar corona in the temperature ranges of 1MK $<$ T $<$ 30 MK. Radiation is passed through nine X-ray analyses filters, passing light through wavelength bands with different lower cutoff energy. In this way the XRT is capable of observing plasmaes with temperatures as low as $\log T = 6$ in the lower corona. The wide temperature range allows for detestations of magnetic energy dissipation in the form of flares and coronal mass ejection. The XRT can also observe in visible light with a G-band filter, making it possible for co-alignment of SOT and XRT images.

EIS

The EUV observations are made by the EUV Imaging Spectrometer , studying emission lines of highly ionized elements in the wavelength band of 170-210Å and 250-290Å, covering the plasma temperatures of a wide range (0.04MK, 0.25MK, 1.0MK $<$ T 20MK). EIS will be discussed in greater detail in chapter three.

1.3 The Oslo Stagger Code

The Oslo Stagger Code is a three dimensional numerical model of the solar atmosphere, modeling the convection zone, photosphere, chromosphere, transition region and corona.

The code is developed at the Institute of Theoretical Astrophysics at the University of Oslo over the last decade.

The main idea with the code is to combine magneto-hydrodynamics and radiative transfer, with the aim to recreate the solar atmosphere in the best possible way. We describe the code in grater detail in chapter four.

1.4 The Thesis

The subject of this thesis lies in analysis of the similarities and differences between transition region and coronal intensities as predicted by the OSC and as observed by Hinode. In this work we calculate the EUV spectra from the numerical model and do a intensity comparison to EUV spectra obtained by EIS with the aim of describe the validity of the spectral line emission of the Oslo Stagger code.

1.4.1 Methods

We will identify active regions a swell as quiet Sun regions on observations obtained by EIS and from Oslo Stagger Code simulations. Spectral line emission from several upper atmospheric lines will be retrieved with the purpose of intensity analysis.

Useful tools will be data analysis software developed at the Institute for Theoretical Astrophysics for treatment of Hinode/EIS data, as well as analysis software developed for the study of Oslo Stagger code data. In addition we have written software for line intensity calculation from both EIS and the OSC based on the CHIANTI database and software package (Landi et al., 2006).

A schematic overview of the work is given by;

1. Level '1' reduction of the Hinode/EIS data; including dark current subtraction, cosmic ray removal, bad pixel correction and absolute calibration.
2. Further reduction to spectral line moments; total intensity, spectral line shift, spectral line widths and correction for continuum contribution.
3. Construction of software for intensity map creation and intensity calculations for the Hinode/EIS observations.
4. Identify important spectral lines in the upper transition region due to Hinode/EIS observations and intensity analysis of these.
5. Study spectral line formation from the three dimensional numerical model.
6. Construction of software for intensity map creation and intensity calculations for the synthetic data from the three dimensional numerical model using CHIANTI.

7. Comparison of the emergent intensity from the Hinode/EIS observations and from the Oslo Stagger Code numerical model.

1.4.2 Thesis outline

The remainder of this thesis is divided into five chapters. We start by going through the basic spectral line formation and the magneto-hydrodynamic equations in chapter two. We continue with a description of the EIS instrument in chapter three, where we discuss the apparatus, the observational data reduction and intensity analysis of this data. In chapter four we investigate numerical model of the Oslo Stagger Code, the synthetic atmosphere of the run and do intensity analysis of the emergent emission. In chapter five we compare the intensities retrieved from the Hinode/EIS observations and the synthetic intensities retrieved from the OSC, discussing the results and the validity of the emergent synthetic spectra. Finally, in chapter six we summarize what we have done and which result we have obtained, as well as give suggestions for further work.

Chapter 2

Basic line formation

Atomic transitions in the transition region and corona caused by various processes of excitation and de-excitation of the energy levels of each ion, result in emission line formation.

Since the region of interest emits in EUV, we only have to consider a few of these processes. A weak radiation field makes even more processes negligible. We will investigate the processes of excitation, ionization and recombinations of atmospheric plasma and the resulting spectral line formation throughout this chapter.

2.1 The specific intensity

By considering the amount of energy transported by the radiation field through an area at a specific location we can define the intensity. More precisely, the amount of energy $\mathrm{d}E_\nu$ transported through the area $\mathrm{d}A$, at a location $\vec{r}$, with $\vec{n}$ the normal to $\mathrm{d}A$, between time t and $t+\mathrm{d}t$, in the frequency band between ν and $\nu + \mathrm{d}\nu$, over the solid angle $\mathrm{d}\Omega$ around the direction $\vec{l}$, gives the specific intensity I_ν as the proportionality coefficient. That is

$$\mathrm{d}E_\nu \equiv I_\nu(\vec{r}, \vec{l}, t)(\vec{l} \cdot \vec{n})\mathrm{d}A\mathrm{d}t\mathrm{d}\nu\mathrm{d}\Omega \tag{2.1}$$

By the cgs unit convention, this gives the specific intensity with units of erg s^{-1} cm^{-2} Hz^{-1} sr^{-1}. We then define the total intensity as the specific intensity integrated over all frequencies, $I \equiv \int_0^\infty I_\nu \mathrm{d}\nu$.

We gain the energy from quantum mechanical processes regarding the electron behavior in a specific energy level of an atom. When an electron moves from an energy level to another, it either consumes energy when exciting to a higher level or disposes energy when de-exciting to a lower level. Looking at the energy gaining processes, we denote the current atomic con-

figuration of the higher energy level as E_u for upper and the lower energy level as E_l, we then gain the energy amount

$$\Delta E = E_u - E_l \tag{2.2}$$

as an emitting photon, This energy amount is detected as a emission line with the frequency ν from $\Delta E = h\nu$.

For a specific intensity I_ν at frequency ν, we have to consider the number density of elements and ions in the desired energy level and the rate of which these excite and de-excite.

For reasons explained later the specific intensity is given by

$$I_\nu = \frac{h\nu}{4\pi} \int_0^s \phi_\nu n_u A_{ul} \mathrm{d}s \tag{2.3}$$

where s is the line of sight, and where we divided by the sphere solid angle 4π to account for the fact that the photons can be sent out in any direction. The line broadening is included in the intensity calculation through the emission line profile ϕ_ν. n_u is upper energy level ('u') density, and the rate at which these ions de-excite to a lower energy level 'l' by emitting a photon is given by A_{ul}.

The transition rate A_{ul} and the upper energy level density n_u are the unknowns. To solve this we need to find out what contributes to the radiation and emission line formation along the line of sight. We will look closer into the processes of excitation, de-excitation, ionization and recombination inn the following sub-chapters. A_{ul} and n_u

2.2 Radiative processes

By radiative processes we mean processes involving photons from a electromagnetic radiation field interacting with bound electrons from various ions in the plasma, or emitting photons from spontaneous decay of the bound electron. We have three radiative processes:

Induced absorption / photoabsorption: When an ion or atom surrounded by an electromagnetic radiation field absorbs a photon. This results in the electron exciting from a lower energy level, X_l, to a higher one, X_u,

$$X_l + h\nu \Rightarrow X_u \tag{2.4}$$

Stimulated emission / radiative excitation: When a bypassing photon interacts with a bound electron causing the electron to decay to lower energy level and emit another photon.

$$X_u + h\nu_i \Rightarrow X_l + h\nu_i + h\nu_j \tag{2.5}$$

where ν_i is the frequency of the bypassing photon interacting with the bound electron.

Spontaneous emission / spontaneous radiative de-excitation: This is the opposite of induced absorption. Here the electron will spontaneously decay from an upper energy level, X_u, to a lower energy level, X_l, and emit a photon in the process.

$$X_u \Rightarrow X_l + h\nu \tag{2.6}$$

If we assume thermal equilibrium(TE) the process of emission versus absorption will settle into equilibrium. Meanwhile the radiation will settle into a blackbody spectrum. For further investigations we need the transition probabilities for the above processes. Einstein made three assumptions when calculating the transition probability P_{ul} per unit time

1. the rate of induced absorption of photons is proportional to the energy density J_ν of the radiation field
2. the distribution of atomic energy level is assumed to be in equilibrium
3. the statistical distribution of the energy level population is given by Boltzmann probability distribution (2.11).

For spontaneous emission the probability coefficient for transition is A_{ul}, and for stimulated emission B_{ul} which is induced by the energy density J_ν. The total probability for emission processes per unit time is then

$$P_{ul} = A_{ul} + B_{ul}J_\nu \tag{2.7}$$

For the opposite action, absorption, we have the probability of transition to a higher level is B_{lu} induced by the energy density J_ν in the plasma.

$$P_{lu} = B_{lu}J_\nu \tag{2.8}$$

Because the transitions are bound-bound transitions, we have the requirement of detailed balance, which states that the net exchange between to energy levels will be balanced given a thermal equilibrium situation.Therefore

$$n_u P_{ul} = n_l P_{lu} \tag{2.9}$$

$$n_u(A_{ul} + B_{ul}J_\nu) = n_l B_{lu} J_\nu \tag{2.10}$$

where n_u and n_l, represent the total number of particles in energy level 'u' and 'l', respectively.

The population density of a exited state, given a fixed temperature T, is given by the Boltzmann equation;

$$n_i = \frac{g_i}{g_0} n_0 \exp(-\frac{\chi_i}{k_B T}) \tag{2.11}$$

where n_i represent the population density of excited state 'i', with n_0 as the population density of the ground state and χ_i the excitation energy from the ground state to state 'i'. The statistical weight of the ground state is denoted by g_0, and the statistical weight of the excited state 'i' is g_i.

From Boltzmann's equation (2.11) we derive a ratio equation between the particle-number in the respective 'u' and 'l' level.

$$\frac{n_l}{n_u} = \frac{g_l}{g_u} \exp(-\frac{\chi_l - \chi_u}{k_B T}) \tag{2.12}$$

where g_l and g_u are the statistical weights of state 'l' and 'u', respectively.

Incorporating this in the equation of detailed balance (2.9) results in;

$$(A_{ul} + B_{ul} J_\nu) \exp(-\frac{\chi_u}{k_B T}) = \frac{g_l}{g_u} \exp(\frac{\chi_l}{k_B T}) B_{lu} J_\nu \tag{2.13}$$

with the photon energy between the states 'u' and 'l' as $h\nu = \chi_u - \chi_l$.

Because of the thermal equilibrium assumption , the energy density J_ν can be described by Plancks function of blackbody radiation B_ν, given by

$$B_\nu = \frac{2h\nu^3}{c^2} \frac{1}{\exp(\frac{h\nu}{k_B T}) - 1} \tag{2.14}$$

where h is Planck's constant, k_B Boltzmann's constant, c the speed of light and ν and T as the frequency and temperature, respectively. Substitution for J_ν in equation 2.13 results in

$$\exp(\frac{h\nu}{k_B T})(1 - \frac{A_{ul}}{B_{ul}}) + \frac{A_{ul}}{B_{ul} F(\nu)} = \frac{g_l}{g_u} \frac{B_l u}{B_u l}$$

where $F(\nu) = 2h\nu^3/c^2$. For this equation to hold for all possible temperatures T, we get the Einstein relations

$$\frac{A_{ul}}{B_{ul}} = F(\nu) \tag{2.15}$$

$$\frac{g_l}{g_u} = \frac{B_{ul}}{B_{lu}} \tag{2.16}$$

The probability coefficients A_{ul}, B_{ul} and B_{lu} are the Einstein Probability coefficients for transition between energy level 'u' and 'l'. Although the relations where determined under the assumption of black body radiation and thermal equilibrium they are independent of temperature, and therefor they must be fundamental properties of the elements, regardless of the nature of the radiation.

2.3 Collisional processes

By collisional processes we mean processes involving free electrons interacting with ions in the plasma, so-called bound-free interactions. The most important of these processes are;

Collisional excitation: When a free electron interacts with a bound electron in an ion, making the bound electron jump from a lower energy level 'l', to a higher energy level 'u'. The bound electron will here strip the free electron of some of its kinetic energy to be able to make the transition. There is a transition rate C_{ul} for this process. The process can be described in the following way;

$$X_l + e^- \Rightarrow X_u + e^- \tag{2.17}$$

with the energy

$$\chi_l + \frac{1}{2} m_e {v_e}^2 \Rightarrow \chi_u + \frac{1}{2} m_e {v'_e}^2 \tag{2.18}$$

where m_e is the free electrons mass, v_e its velocity, with the interacting ion marked as X. The free electron will have lower velocity v'_e after the interaction, because of loss of some energy, $h\nu = \chi_u - \chi_l$.

Collisional de-excitation: The opposite of collisional excitation with transition rate C_{ul}, described by this particle notation;

$$X_u + e^- \Rightarrow X_l + e^- \tag{2.19}$$

and energy

$$\chi_u + \frac{1}{2} m_e {v_e}^2 \Rightarrow \chi_l + \frac{1}{2} m_e {v'_e}^2 \tag{2.20}$$

where m_e is the free electrons mass, v_e its velocity, with the interacting ion marked as X. The free electron will have higher velocity v'_e after the interaction, because of energy gain $h\nu = \chi_u - \chi_l$.

We have the transition rate C_{lu} for collisonal excitation and C_{ul} for the collision de-excitation.

The collision transition rate for excitation is related to the collisional cross section σ_{lu} and the velocity distribution function $f(v)$ through

$$C_{lu} = n_e \int_0^\infty \sigma_{lu}(v) v f(v) dv \tag{2.21}$$

where n_e is electron density.

For further derivations we assume a Maxwellian distribution given by

$$f(v) = (\frac{m}{2\pi k_B T})^{3/2} 4\pi v^2 \exp(-\frac{mv^2}{2k_B T}) \tag{2.22}$$

where k_B is the Boltzmann constant, v the velocity of the particle, m the mass and T the temperature.

If we assume that the scattering is not particularly strong, we can further assume that the wave function of the colliding system is approximately equal to the incident wave function, which is the Born approximation. Applying a Coulomb potential in the wave function, and expanding it in surface harmonics, the collisional cross section can according to Lang (1999) and Hebb and Menzel (1940) be derived to

$$\sigma_{lu} = \frac{\pi}{g_l} (\frac{h}{2\pi m_e v})^2 \Gamma(T_e, v) \tag{2.23}$$

where h is Planck's constant, m_e the electron mass, v the electron velocity and Γ the collisional strength (dependent on electron temperature, T_e, and velocity v). If we do not include the electric dipole moment in our calculations the collisional strength becomes independent of velocity (Lang, 1999). This gives the transition rate for collisional induced excitation from state 'l' to state 'u'

$$\begin{aligned} C_{lu} &= n_e \Gamma(T_e) \, \frac{\pi}{g_l} \, (\frac{h}{2\pi m_e})^2 \, (\frac{2m_e}{\pi k_B T})^{1/2} \int_0^\infty \exp(-x) dx & (2.24) \\ &= \frac{h^2}{(2\pi m_e)^{3/2}} \, \frac{1}{(k_B T)^{1/2}} n_e \, \frac{\Gamma(T_e)}{g_l} & (2.25) \\ &\approx 8.63 \times 10^{-6} \, T^{-1/2} \, n_e \, \frac{\Gamma(T_e)}{g_l} & (2.26) \end{aligned}$$

We have used the substitution $x = \frac{m_e v^2}{2k_B T}$ in the Maxwell distribution (eq. 2.22), C_{lu} have units [s^{-1}]. We get the same expression for C_{ul} only with

the the statistical weight g_u instead of g_l.

The equation of detailed balance for collisional excitation transitions is

$$n_u C_{ul} = n_l C_{lu}. \tag{2.27}$$

Given the particle density n_u for energy state 'u' and n_l for energy state 'l' from the Boltzmann distribution 2.11 we get the relation between the collisional transition rates

$$\frac{C_{lu}}{C_{ul}} = \frac{g_l}{g_u}\exp(-\frac{h\nu}{k_B T}), \tag{2.28}$$

where $h\nu$ is the excitation energy between state upper 'u' and lower state 'l'. The equation holds as long as we have a Maxwellian velocity distribution.

2.4 Ionization and recombination processes

In the solar atmosphere there are many processes leading to ionization of the plasma elements, atoms gets stripped of electrons and interactions leading to the inverse processes, where ions catch electrons. The energies needed to carry out such processes are taken from the photons in the radiation field as absorption, at the same time these processes also contribute to the radiation by emission. We will here look closer at some of these processes.

2.4.1 Photo-ionization

This is a bound-free transition. A photon interacts with an ion X of ionization degree m. If the photon energy, $h\nu$, is larger than the ionization energy χ_i of a electron in energy state 'i' of the ion, the ion becomes ionized. The now free electron will carry the extra energy $\Delta E = h\nu - \chi_i = \frac{1}{2}m_e v_e^2$ as kinetic energy. The process can be described by

$$X_i^m + h\nu \Rightarrow X_j^{m+1} + e^-. \tag{2.29}$$

The photo-ionization rate is given by

$$I_{im}^{ph} = 4\pi n_e \int_{\nu_0}^{\infty} \frac{\sigma_{im}(\nu)}{h\nu} J_\nu d\nu, \tag{2.30}$$

where J_ν is the mean intensity and σ_{im} is the ionization cross section, ν_0 the threshold frequency for ionization, and n_e the electron density. For hydrogen-like ions the bound-free ionization cross section σ_{im} is given (Lang, 1999) as

$$\sigma_{im} = \frac{32\pi^2 e^6 R_\infty Z^4}{3^{3/2} h^3 \nu^3 n^5} g_{fb}(T,\nu), \tag{2.31}$$

where $R_\infty = 2\pi^2 e^4 m_e/(h^3 c)$ is the Rydberg constant, m_e the electron rest mass, e the electron charge, Z the ion charge number, ν the photon frequency and $g_{bf}(T,\nu)$ the bound-free Gaunt factor.

2.4.2 Radiative recombination

The process of radiative recombination is a free-bound transition. This is the opposite process of photoionization, where now a free electron (with kinetic energy $\frac{1}{2}m_e v_e^2$) is captured by an ion in to one of its available energy states 'i' (with energy χ_i). The excess energy is emitted as a photon $h\nu = \frac{1}{2}m_e v_e^2 - \chi_i$. This process can be described by

$$X_j^{m+1} + e^- \Rightarrow X_i^m + h\nu. \tag{2.32}$$

In TE, detailed balance is required. The number of particles involved in radiative recombination must balance the number of particles involved in photoionization. Denoting the radiative recombination rate coefficient with R_{rr}, the detailed balance equation is

$$R_{rr} n_i^{m+1} = I_{im}^{ph} n_i^m \tag{2.33}$$

$$R_{rr} = \frac{n_i^m}{n_i^{m+1}} I_{im}^{ph}. \tag{2.34}$$

We can further use Sahas equation (2.35) to find the population ratio of the number of ions in ionization stage $(m+1)$ to the number of ions in ionization stage m;

$$\frac{n_i^{m+1}}{n_i^m} = \frac{2}{n_e} \frac{(2\pi m_e k_B T)^{3/2}}{h^3} \frac{g_{m+1}}{g_m} \exp(-\frac{\chi_{i+1} - \chi_i}{k_B T}). \tag{2.35}$$

Where χ_{i+1} and χ_i is the ionization energy of stage $(i+1)$ and i, respectively. The statistical weight of $(m+1)$ times ionized atom is denoted by g_{m+1}, and the statistical weight of the m times ionized atom is g_m.

2.4.3 Collisional ionization

In collisional ionization a free electron with energy $\frac{1}{2}m_e v^2$ interacts with an ion X^m, removing a electron of energy level 'i' from the ion in the process, as described by

$$X_i^m + e^- \Rightarrow X_j^{m+1} + e^- + e^-, \tag{2.36}$$

and energy

$$\chi_i^m + \frac{1}{2}m_e v^2 \Rightarrow \chi_j^{m+1} + \frac{1}{2}m_e v_1^2 + \frac{1}{2}m_e v_2^2. \tag{2.37}$$

The ionization rate for this process can be describer in the same manner as the collisional rate,

$$I_{im}^{col} = \int_{v_0}^{\infty} \sigma_{im}^{col} v f(v) dv, \tag{2.38}$$

where $\sigma_i m^{col}$ is the collisional ionization cross section. From Mihalas (1978) we find the collisional cross section expressed in terms of the photoionization cross section σ_{im}

$$I_{im}^{col} = \frac{1.55 \times 10^{13} n_e T^{-1/2} \bar{w}_i \sigma^{im}(\nu_0) \exp(-\frac{\chi_0}{k_B T})}{\chi_0/(k_b T)} \tag{2.39}$$

where χ_0 is the ionization threshold energy and $\bar{w}_i$ is of order 0.1, 0.2 and 0.3 for ion charge Z = 1,2 and >2, respectively.

2.4.4 Three body recombination

The opposite process as collisional ionization. Here two electrons enters the volume of an ion (X^{m+1}) at the same time, but where only one of the electrons is captured by the ion to one of its available energy states 'i', so that the other electron can carry away the extra energy. The process can be described by

$$X_j^{m+1} + e^- + e^- \Rightarrow X_i^m + e^- \tag{2.40}$$

with energy

$$\chi_j^{m+1} + \frac{1}{2} m_e v_1^2 + \frac{1}{2} m_e v_2^2 \Rightarrow \chi_i^m + \frac{1}{2} m_e v^2. \tag{2.41}$$

We denote the coefficient for three body recombination by R_3. By the detailed balance argument we obtain

$$R_3 n_i^{m+1} = I_{im}^{col} n_i^m \tag{2.42}$$

$$R_3 = \frac{n_i^m}{n_i^{m+1}} I_{im}^{col}, \tag{2.43}$$

which hold for all cases as long as the velocity distribution function is Maxwellian. We get a more detailed derivation by inserting for Sahas equation (2.35) to find the population ratio of ionization stage m and $(m+1)$.

2.4.5 Autoionization and Dielectronic recombination

The process of deelectronic recombination is more complicated than the three body recombination. Now we have an incoming electron, which is captured by a ion in the ground state 'g'. The captured electron falls into an available energy level 'i', while a bound electron of the ion also becomes excited (to energy level 'j') by the extra energy of the free electron;

$$X_g^{m+1} + e^- \quad \Rightarrow \quad X_{ij}^m. \tag{2.44}$$

Dielectric recombination is accomplished when the highly unstable double excited configuration stabilizes. Resulting in either one or both electrons

falling down to the lowest available states and emitting a photon in the process, by the description

$$X_{ij}^{m} \quad \Rightarrow \quad X_{gj}^{m} + h\nu. \tag{2.45}$$

We denote the ionization rate for this process by R_d.
This step may also result in what is known as autoionization;

$$X_{ij}^{m} \quad \Rightarrow \quad X_{g}^{m-1} + e^{-}. \tag{2.46}$$

This is possible if the energy of the lowest excited electron is larger than the binding energy of the other excited electron, which results in that electron de-exciting to the ground state, while the other electron breaks free from the ion. The ionization rate for autoionization is I^a.

2.5 Solving the specific intensity equation

To solve the equation of specific intensity (2.3) we need to consider the environment of the transition region. We are interested in the EUV and UV portion of the solar spectrum, while we until now have derived the sources and sinks of the emission and species origin, we have not discussed scattering processes which change the path of a photon, for example Thomson scattering. The reason is that the plasma of the transition region is of such low density that we can assume that all emitted photons leave the atmosphere without being scattered, therefore we say that the plasma is *optically thin*. This is an important simplification of our calculations. But you can also have scattering in the transition involved. This will not happen often in the transition region and corona because the densities are low.

2.5.1 The corona approximation

We are interested in the extreme ultraviolet (EUV) and ultraviolet (UV) region of the solar spectrum. This is emitted from the transition region and the corona of the solar atmosphere where the temperatures are high ($T > 10^4$K) and the densities are low ($n_e < 10^{18} m^{-3}$). With these conditions we can make some simplifications according to the coronal approximation, which states that the typical timescales of collisional processes are shorter than for the ionization and recombination processes. We can therefore say that the collisional excitation determines the population of excited states. Spontaneous radiative de-excitation processes overwhelms the stimulated emission and collisional de-excitation processes. Because of the principle of detailed balance, we can approximate that the collisional excitations are balanced out by the spontaneous radiative de-excitation,

$$n_u A_{ul} = n_l C_{lu}. \tag{2.47}$$

Assuming that equation 2.47 is correct, we may substitute it in to the equation for specific intensity 2.3, where we now only need an expression for the population density of ions in state 'l', n_l.

2.5.2 The population density

The population density n_l^m of level 'l' in the ionized atom X^m can be expressed as a chain of ratios

$$n_l^m = \frac{n_l^m}{n^m}\frac{n^m}{n}\frac{n}{n_H}\frac{n_H}{n_e}n_e. \tag{2.48}$$

The first factor n_l^m/n^m refers to the level populations, and can be determined by solving the equations of statistical equlibrium assuming that the corona approximation is valid. This is a quite difficult task in dealing with many level atoms and ions, but has been pre-calculated as a function of electron density and temperature in the CHIANTI software (see section 2.5.4, Landi et al. (2006)).

The second factor n^m/n is the ionization ratio of the ion X^m relative to the total population density of the element X, where CHIANTI again is very useful. The third factor is the element abundance relative to hydrogen

$$Ab_x = n/n_H. \tag{2.49}$$

The last ratio involved in the chain is the hydrogen density relative to electron density. This is according to Aschwanden (2004) given as

$$\frac{n_H}{n_e} \approx 0.83. \tag{2.50}$$

Which is based on an abundance and complete ionization of both helium and hydrogen, with the abundance relation H:He=10:1.

This results in the population density

$$n_l^m = 0.83 Ab_X n_e \frac{n_l^m}{n^m}\frac{n^m}{n}. \tag{2.51}$$

2.5.3 The equation of statistical equilibrium

With the equation of statistical equilibrium we calculate the occupation numbers of bound and free states of atoms, while the surrounding environment changes. The equation is given by

$$\frac{\partial n_i^m}{\partial t} + \nabla \cdot (n_i^m \vec{v}) = \sum_{i \neq j} (n_i^m P_{ij} - n_i^m P_{ji}) \tag{2.52}$$

where the total rate from level 'i' to 'j' is P_{ij}, that is all processes involved in an upward transition versus all processes involved in the downward transitions. In a static atmosphere this results in

$$n_j^m \sum_{i \neq j} P_{ij} - \sum_{i \neq j} n_i^m P_{ji} = 0. \tag{2.53}$$

Process	**Rate** (s^{-1})	**Characteristic Time** (s)
Collisional excitation	C_{ij}	2×10^{-3}
Collisional de-excitation	C_{ji}	2×10^{-3}
Spontaneous radiative decay	$A_i j$	4×10^{-9}
Collisional ionization	I_{col}	107
Autoionization	I^a	
Total ionization rate	$I^{tot} = I^a + I^{tot}$	107
Radiativ recombination	R_{rr}	88
Dielectric recombination	R_d	
Total recombination rate	$R_{tot} = R_{rr} + R_d$	88

Table 2.1: Characteristic times of important atomic processes in the transition region for C IV, calculated by Mariska (1992).

Considering the low density and the low radiation field of the transition region and by looking at characteristic time scales of the transitions (see example on table 2.1), we can make further approximations.

With the excitation and de- excitation processes we arrive at what is known as the corona approximation discussed in section 2.5.1.

Because the radiation field is to weak to produce significant photoionization, the main ionization process is collisional ionization. Radiative recombination together with the dielectric recombination are the main recombination processes. Because of the low density plasma the three body recombination is highly unlikely. Denoting the recombination processes by $R = (R_{rr} + R_d)$ and ionization process $I = I^{col}$ we get the following rate equation

$$n^{m-1} I^{m-1} + n^{m+1} R^{m+1} = n^m (I^m + R^m) \tag{2.54}$$

From this equation we can calculate the ionization ratio of the ion X^m relative to the total population density of the element X, as needed in the second factor of equation 2.51.

2.5.4 CHIANTI

CHIANTI (Landi et al., 2006) is an atomic database for spectroscopic diagnostics of astrophysical plasmas. It provides us with up-to-date atomic data

together with several programs for spectra calculations and analysis. This will be a useful tool in our research.

2.5.5 Emission line spectroscopy

From the specific intensity given by equation 2.3, we choose the line of sight s to be equal to the depth axis z, so that

$$I_\nu = \frac{h\nu}{4\pi}\int_0^z n_u A_{ul}\mathrm{d}z \tag{2.55}$$

By substituting with the population density equation (2.51) into equation 2.55 , the emission line intensity is the given by

$$\begin{aligned} \mathrm{I}_\nu &= \frac{h\nu}{4\pi}\int_0^z 0.83 A b_X n_e \frac{n_u^m}{n^m}\frac{n^m}{n}A_{ul}\mathrm{d}z \\ &= A b_x \int_0^z n_e^2 C(T,\nu,n_e)\mathrm{d}z \end{aligned} \tag{2.56}$$

where $C(T,\nu,n_e)$ is the **contribution function** defined as

$$C(T,\nu,n_e) = 0.83\frac{h\nu}{4\pi}\frac{n_u^m}{n^m}\frac{n^m}{n}\frac{A_{ul}}{n_e} \tag{2.57}$$

which is tabulated as used in the CHIANTI code (see section 2.5.4).
The contribution function is strongly dependent on the electron temperature an weakly dependent on the electron density. We can see this because the function is dependent on both the collision rate through the corona approximation (eq. 2.47) and through the ionization fraction. The contribution function gives information about the temperature regimes in the solar atmosphere. Giving us the information of which elements contributes to the emission line formation.

A measure of the amount of plasma along the line of sight that contributes to the emitted radiation in the temperature interval between T and $T + \Delta T$ is the **differential emission measure** defined as

$$DEM = n_e^2\frac{dz}{dT} \tag{2.58}$$

which result in the specific intensity

$$I_\nu = A b_x \int_0^T C(T,\nu,n_e)DEM\mathrm{d}T \tag{2.59}$$

To be able to calculate the emission measure and the contribution function we need to find the time-dependent thermodynamic properties of the

transition region since $C(T, \nu, n_e)$ and DEM has such a strong dependence on the electron temperature and density. To get a good enough description we need to take a closer look at Maxwell's equations of electromagnetism and the fluid equations, resulting in the magneto-hydrodynamic equations of the plasma.

2.6 The Magneto-hydrodynamic equations (MHD)

From observations we see that the magnetic field plays an important role in the dynamics of the solar atmosphere. This relation can be described by the ratio parameter β between the magnetic pressure and the gas pressure

$$\beta = \frac{4\pi P}{B^2} \tag{2.60}$$

where the magnetic field shapes the plasma if $\beta \leq 1$. From the photospheric levels of the atmosphere the plasma is dominated by the gas pressure but as we travel up in the atmosphere, the magnetic pressure starts to dominate as the gas pressure and density decrease exponentially with a scale height of a few hundreds of kilometers, while the magnetic pressure falls off muss less rapidly.

2.6.1 The Maxwell equations

We can describe the magnetic behavior in the plasma by taking a closer look at the Maxwell equations

$$\nabla \times \mathbf{B} = \frac{4\pi}{c}\mathbf{j} \tag{2.61}$$

$$\nabla \times \mathbf{E} = -\frac{1}{c}\frac{\partial \mathbf{B}}{\partial t} \tag{2.62}$$

$$\nabla \cdot \mathbf{B} = 0 \tag{2.63}$$

$$\eta \mathbf{j} = \mathbf{E} + \frac{\mathbf{u} \times \mathbf{B}}{c} \tag{2.64}$$

where magnetic field and the electric are represented by $\mathbf{B}$ and $\mathbf{E}$, respectively, and η it the viscosity of the fluid. We eliminate the electric field $\mathbf{E}$ and the current density $\mathbf{j}$ from the equations by substituting equation 2.61 and 2.64 into 2.63, resulting in

$$\frac{\partial \mathbf{B}}{\partial t} = \nabla \times (\mathbf{u} \times \mathbf{B}) - \frac{\eta c^2}{4\pi}\nabla \times (\nabla \times \mathbf{B}) \tag{2.65}$$

which by substitution of equation 2.63 becomes the magnetic diffusion equation;

$$\frac{\partial \mathbf{B}}{\partial t} = \nabla(\mathbf{u} \times \mathbf{B}) + \frac{\eta c^2}{2\pi}\nabla^2 \mathbf{B}. \tag{2.66}$$

This equation describes the magnetic variation with time, where the first term describes the gas motion contribution to the field and the second term describes how the diffusion destroys the field.

2.6.2 The Navier -Stokes equations

The Navier-Stokes equations describes the behavior of a fluid. Viscous, gravitational, pressure and other forces acting internally in the fluid results in change of its momentum and energy.

Conservation of mass

$$\frac{\partial \rho}{\partial t} + \nabla \cdot (\rho \mathbf{u}) = 0 \tag{2.67}$$

where ρ is the density of the fluid and $\mathbf{u}$ is its velocity.

Conservation of momentum

$$\frac{\partial \mathbf{u}}{\partial t} + (\mathbf{u} \cdot \nabla)\mathbf{u} = -\frac{\nabla P}{\rho} + \frac{\eta}{\rho}(\nabla^2 \mathbf{u}) + (\eta + \xi)\nabla(\nabla \cdot \mathbf{u}) \tag{2.68}$$

where both dynamic (η) and compressional (ξ) viscosity are taken into account, with P representing the gas pressure.

Conservation of energy

$$\frac{\partial \epsilon}{\partial t} + \nabla(\epsilon \mathbf{u}) = -\frac{P}{\rho} - \frac{1}{\rho}\nabla \mathbf{q} + \frac{Q}{\rho} \tag{2.69}$$

where the equation of state is $\epsilon = \epsilon(\rho$,P) and viscous heating rate is Q.

2.6.3 The MHD equations

We derive what is known as the MHD equations by combining the Maxwell equations with Navier-Stokes equations. If we assume the the atmospheric plasma is incompressible ($\nabla \cdot \mathbf{u} = 0$) and neglect the viscosity we arrive at the basic equations of MHD;

$$\frac{\partial \rho}{\partial t} + \nabla \cdot (\rho \mathbf{u}) = 0 \tag{2.70}$$

$$\frac{\partial \epsilon}{\partial t} + \nabla(\epsilon \mathbf{u}) + \mathbf{u} \cdot \nabla P = \nabla \mathbf{F_r} + \nabla \mathbf{F_c} + Q_{joule} \tag{2.71}$$

$$\frac{\partial \mathbf{B}}{\partial t} - \nabla \times (\mathbf{u} \times \mathbf{B}) = 0 \tag{2.72}$$

$$\frac{\partial \mathbf{u}}{\partial t} + (\mathbf{u} \cdot \nabla)\mathbf{u} + \frac{1}{\rho}\nabla P = \frac{1}{4\pi\rho}(\nabla \times \mathbf{B}) \times \mathbf{B} - g\hat{z} \tag{2.73}$$

where $\mathbf{F_r}$ and $\mathbf{F_c}$ represent the radiative flux and the conductive flux, respectively, replacing $\mathbf{q}/\rho$ in equation 2.69. The Joule heating is denoted by Q_{joule}. For the solution of this set of equations, an equation of state $\epsilon = \epsilon(\rho,P)$ is needed.

This is the model of which we base our research on. We will look further into this in chapter four.

Chapter 3

EIS - Apparatus and observations

The Extreme ultraviolet Imaging Spectrometer (EIS) on Hinode can observe solar corona and upper transition region emission lines in the two wavelength bands of 170-210Å and 250-290Å.

The instrument measures line profiles; line intensities, centroid positions and widths, so that plasma velocities and line broadening can be calculated. Spectroscopic diagnostics such as these will help us identify and characterize several mysteries, including the basic heating and dynamic properties in the upper solar atmosphere.

The emission lines formed within the wavelength bands of EIS, are mainly from highly ionized elements, such as Fe XII 195.119 Å and Fe XV 284.160 Å characterizing plasma at ∼1 MK or greater, but also a fewer number of lines such as He II 256.317 Å and Si 275.350 Å which are formed in the transition region at some ∼ 100 kK. This gives us the opportunity to measure detailed plasma properties from a wide range of temperatures (0.04MK,0.25 MK, 1.0 MK $<$ T $<$ 20MK). Figure 3.1 and 3.2 show the expected emission spectrum of these wavelength bands with the strongest lines marked, in quiet Sun and active region. These plots are made using CHIANTI assuming a constant density of 1.0×10^9 cm^{-3} and ionization fraction provided by Arnaud and Rothenflug (1985), as well as 'active region' and 'quiet Sun' emission measures, for the respective active region and quiet Sun plots.

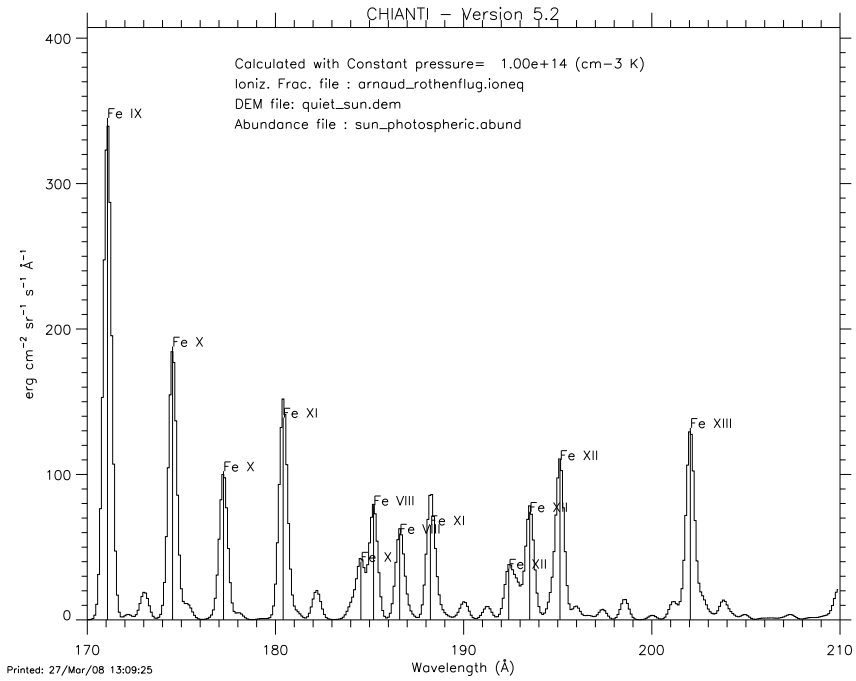

(a) Quiet sun

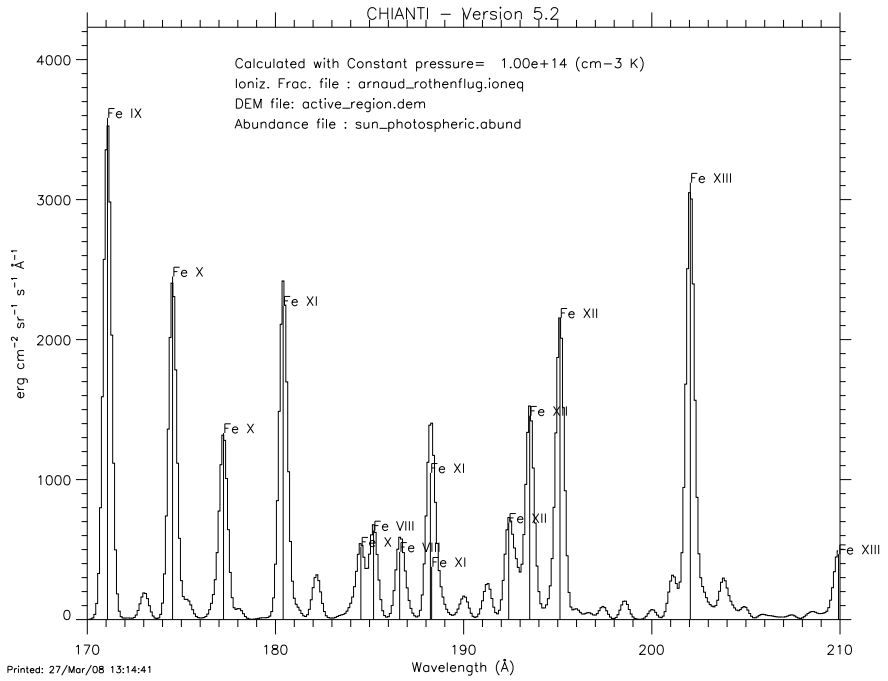

(b) Active Region

Figure 3.1: Active Region and Quiet Sun emission spectrum for the 170-210 Å wavelength band

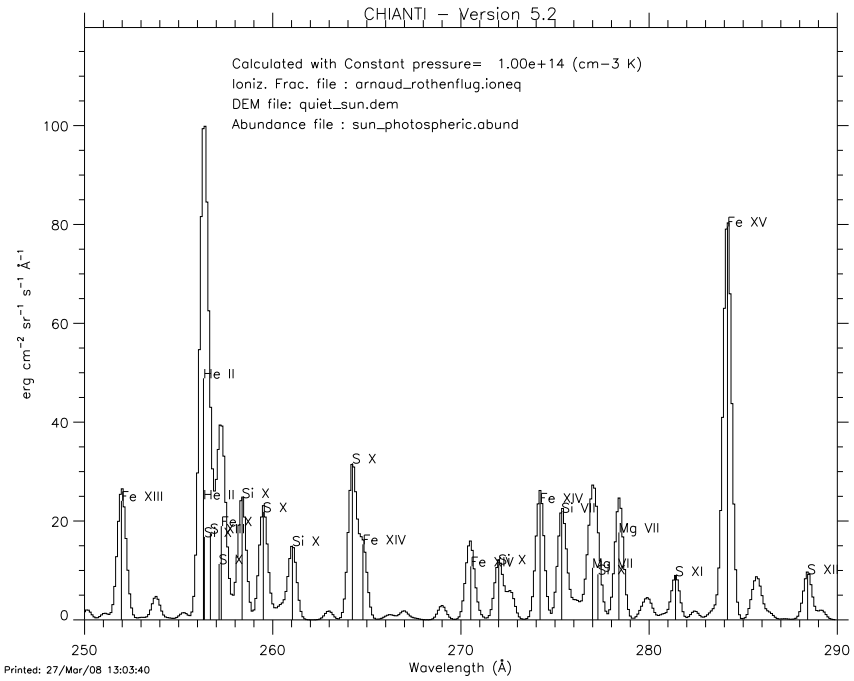

(a) Quiet sun

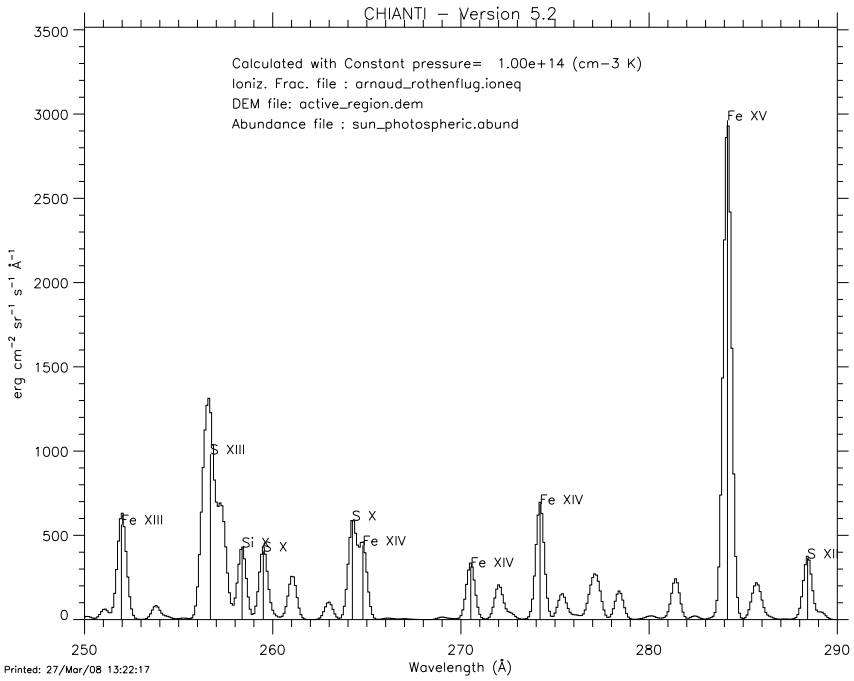

(b) Active Region

Figure 3.2: Active Region and Quiet Sun emission spectrum for the 250-290 Å wavelength band

3.1 The EIS Instrument

3.1.1 Instrument Overview

The EIS instrument design use multilayer coating applied to both mirrors and grating to allow normal incidence operation of the optical elements. The use of thinned back-illuminated CCD cameras register the diffracted photons with high quantum efficiencies (QE) and good spatial resolution.

The layout of the EIS instrument is as shown in figure 3.3. The solar radiation enters through the entrance filter composed of a thin Al filter which stops the transmission of visible radiation. The primary mirror focuses the photons onto a slit/slot mechanism. This exchange mechanism allows the choice of four possible apertures; two slits and two imaging slots. The instrument field of view is set by the raster scan range of 6 arcmin in the dispersion direction and slit height of 8.5 arcmin.

The radiation path continues through a rotating shutter which controls the exposure times, followed by a Al filter providing redundancy in blocking any remaining visible light. The ray is then incident on a toroidal concave grating; splitting and reflecting the beam into a pair of thinned back illuminated CCD cameras, one for each wavelength band. The instrument properties are summarized in table 3.1.

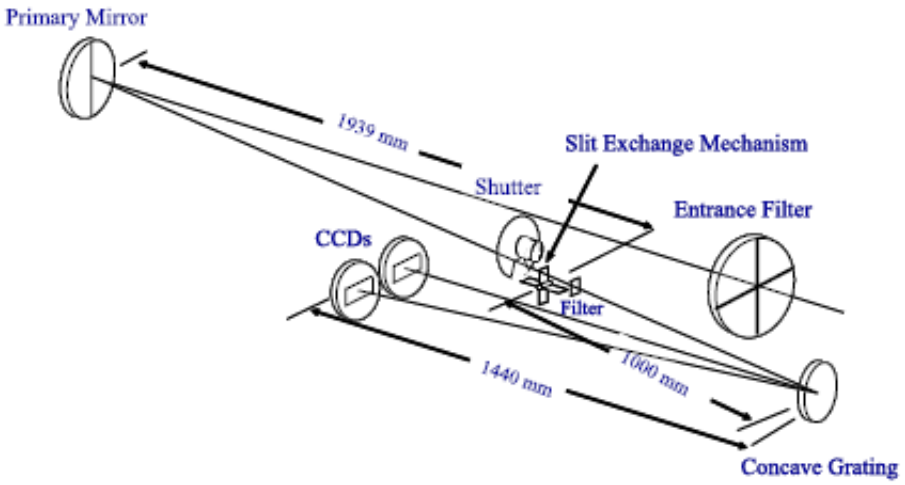

Figure 3.3: Optical layout for EIS. S/SW and L/LW refer to short and long wavelength bands.

Wavelength bands	170-210 Å and 250-290 Å
Peak effective areas[a]	0.30 cm^2 and 0.11 cm^2
Primary mirror	15 cm diameter: two Mo/Si multilayer coatings
Grating	Toroidal/laminar, 4200 lines/mm two Mo/Si multilayers
CCD cameras	Two back thinned e2v CCDs, 2048 ×1024×13.5 μm pixels
Plate scales[a]	13.53 μm/arcsec (at CCD); 9.40 μm/arcsec (at slit)
Spatial resolution(pixel)	2 arcsec (1 arcsec)
Field of view	6 arcmin×8.5 arcmin, offset center: ± 15 arcmin E-W
Raster	1 arcsec in 0.7s[b](Minimum step size: 0.123 arcsec)
Slit/Slot widths[a]	1, 2, 40 and 266 arcsec
Maximum Spatial hight	512 arcsec
Spectral resolution[a]	47 mÅ (FWHM) at 185 Å; 1 pixel=22 mÅ or approx 25 km s^{-1} $pixel^{-1}$
Temperature coverage	log T=4.7, 5.6[c], 5.8[c], 5.9[c],6.0-7.3 K
CCD frame read time	0.8 s
Line observations	Simultaneous observation of up to 25 lines

[a]Measured values.

[b]Raster steps occurred during CCD readout sequences.

[c]Quiet Sun lines of Fe VII, Si VII, Si VIII; count rates≈0.5 -1.0 counts $s^{-1}pixel^{-1}$.

Table 3.1: EIS performance parameters (*J.L. Culhane et al., 2007*).

3.1.2 The Slit/Slot mechanism

As mentioned in section 3.1.1 the EIS imaging spectrometer has a slit/slot interchange mechanism.

There are two slit apertures best appropriate for emission line spectroscopy. The best spatial resolution is gained by using the 1 arcsec wide slit giving a field of view (FOV) of 1 arcsec $\times$ 512 arcsec. With the 2 arcsec wide slit the FOV becomes 2 arcsec $\times$ 512 arcsec, resulting in lower resolution but higher throughput. There are also two slot apertures best appropriate for imaging EIS emission lines, with lower resolution but much larger FOVs without requiring rastering. This setup can only be used for lines which are strong and isolated (no nearlying strong lines). The corresponding FOVs are 40 arcsec $\times$ 512 arcsec and 250 arcsec $\times$ 512 arcsec. The slit and slot FOVs are superimposed on a solar disk image in figure 3.4.

The mirror can be rotated in steps of $\approx$ 0.125 arcsec about the Y axis (the solar N-S, see figure 3.4), with between 600 and 3200 step numbers, it is possible to cover a region up to 3200 $\times$ 0.125 arcsec= 400 arcsec.

Raster images (spectroheliograms) are formed by tilting the mirror in fine increments on the slit, which moves the image in the E-W direction (see figure 3.4) meanwhile taking exposures at each raster position. The motion pattern and possibilities of raster size selection is shown in figure 3.5 with the maximum possible field of view.

3.1.3 Communications

Communications with the spectrometer are done by upload of observation tables to the EIS Instrument control unit(ICU) by the spacecraft Mission Data Processor (MDP).

The observation tables organize the readout of spectral and imaging data from the CCD cameras for up to 25 user selected spectral windows.

Execution of appropriate sets of observing studies with different parameters and commands for the shutter, scanning and slit/slot mechanism are also generated by the ICU. A total overview of the electronics and communications of the subsystem interconnections can be seen in figure 3.6. A detailed description may be found in J.L. Culhane et.al, 2007.

3.1.4 Memory and capacity

The EIS instrument currently has a 15 % share of the downlink telemetry rate of 4Gbps and the 7 Gbits spacecraft main memory. The Norwegian Svalbard ground station (by ESA and The Norwegian Space Agency) allows 15 ground station contacts each day, in addition to four ground station contacts with the JAXA station (Uchinoura Space Senter, USC) for downloading scientific data. With the instrument data throughput set by the number of ground

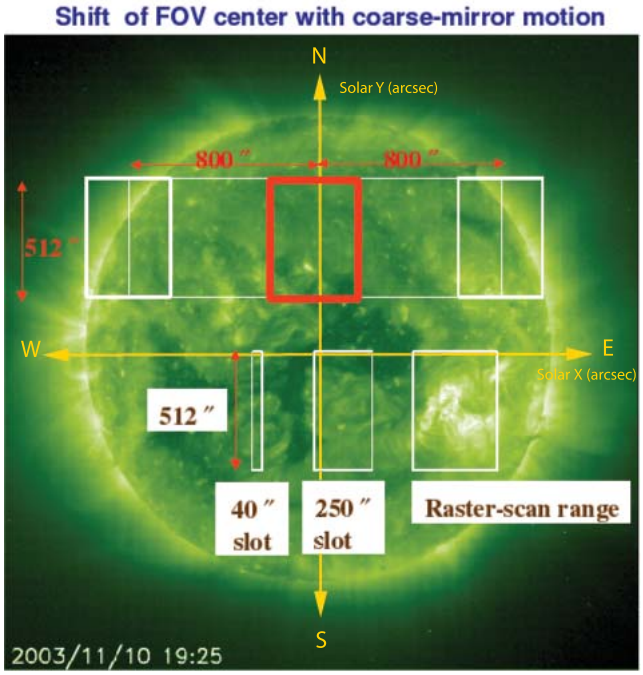

Figure 3.4: Two slot FOVs superimposed on an EIT image together with the raster size at each of the coarse motions. A coordinate system of the solar X and Y is also drawn in for orientational purposes.

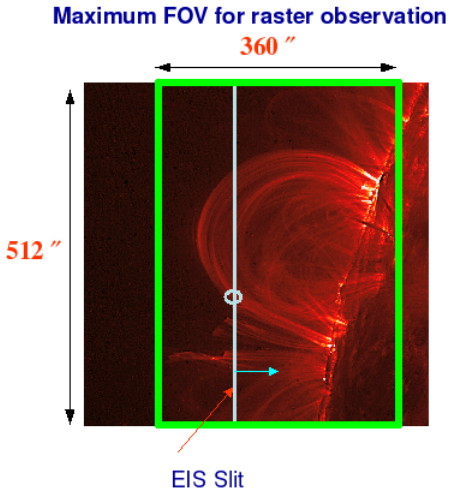

Figure 3.5: The raster selection range and mirror tilt possibilities. Raster observations are made by tilting the mirror in fine increments on the slit. This result in a E-W motion, as the arrow on the figure indicates.

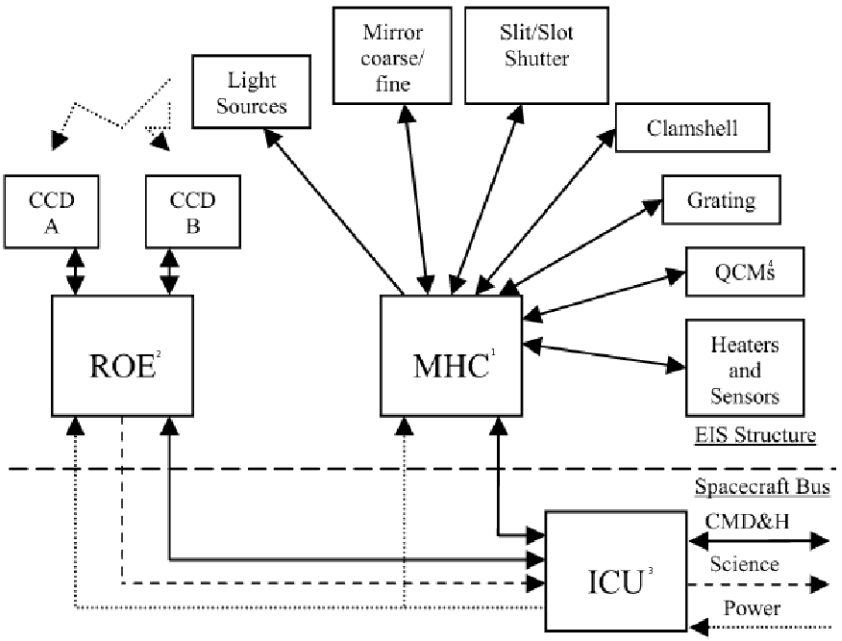

[1]MHC: Mechanism and Heater Control unit. [2]ROE: Read Out Electronics (for camera). [3]ICU: Instrument Control Unit. [4]QCM: Quartz Crystal Microbalances.

Figure 3.6: EIS subsystem interconnections.

station contacts per day and average contact time of 11.5 min, approximately 6.3 Gbits of EIS data are downloaded every day.

3.1.5 The dual CCD camera

CCD is an abbreviation for Charge-Coupleded Device, with the detection mechanism strongly related to the photoelectric effect. Electron hole pairs are produced when photons hit a semiconductor, trapping the free electrons in potential wells produced by numerous small electrodes. The trapped electrons accumulate until their total number is read out by charge coupling the detecting electrodes to a single read out electrode. The performance of a CCD detector is dependent of the quantum efficiency (QE) - the ratio of the total number of photons detected to the number of incident photons, the change in the output signal as a function of the photon wavelength (spectral response) and several other factors which we will not go further into in this text, but can be looked up in a textbook by *e.g.* Kitchin (2003, Astrophysical Techniques).

The EIS camera consist of two CCDs and the Read-Out Electronics (ROE) unit. The CCDs are backilluminated and thinned to maximize the quantum efficiency. There are 1024 pixels in the spatial direction and 2048 in

the dispersion direction, with a pixel size of 13.5 μm $\times$ 13.5 μm, equivalent to 1 arcsec in the spatial direction and 0.0223 Å in the spectral direction. The read out time for the dual CCD camera is around 2μs/pixel.

The CCDs of EIS has a full well capacity of 90k electrons, and a amplifier gain of 6.6±0.03 electrons per Data number (DN), defined by

$$DN = \frac{N_e}{G} + \mathrm{DC} \tag{3.1}$$

where G is the gain, and DC the Dark Current, or bias. The bias is set to roughly 500 counts, in the long range band this corresponds to approximately 7500 photons.

The EIS camera has a total signal chain noise, composed of the photon-shot noise, thermal noise and quantization noise. The Photon-shot noise is caused by the fluctuations of detected photons, a consequence of discretization of the energy carried by the individual photons. Thermal noise is the electronic noise generated by the thermal vibration of the electrons in the CCD. The quantization noise is a rounding error between the analogue input voltage to the analog-to-digital conversion (ADC) and the output digitized value, introduced in the ADC process. In sum these effects amount to a total signal noise effect of about 10 root-mean-square (RMS) read out electrons.

3.1.6 Instrument performance and inefficiencies

While using optics such as shown in figure 3.3 we have to consider the effectiveties and photon interaction of all the different parts of the instrument interacting with the incoming radiation. We use this section to summarize this point.

EIS has two 1500 Å thick Al entrance filters so to reject visible light. The radiation of interest incident on the filter will only partly be transmitted through the filter, depending on which wavelength the incident photon carries. Measurements of the transmission rates show that the filter is much more effective in blocking the visible light and transmitting the desired EUV light for the long wavelength band.
Because nearly all materials absorb strongly at short wavelengths, it is difficult to manipulate light in these wavelength ranges, but by using multilayer coatings on the optics the reflectivity can increase dramatically. This is because multilayer coating consists of several layers of high-mass metals and low-mass metals in pairs, resulting in constructive interference of the scattered light, causing the mirror to reflect in the desired wavelength band (Windt et al., 2004). The EIS mirror is an off-axis paraboloid, consisting of two D shaped parts, one of each wavelength band, as shown in figure 3.3. Two Mo/Si multilayer coatings were applied to both halves of the mirror so to achieve maximum reflectively. This makes it possible to reflect light at

normal incidence even at short wavelengths of the EUV, but the reflectivity is still less than 100 %. The coating achieves peak reflectivities of 32% and 23% for the short and the long wavelength bands, respectively: Even though the reflectivity is improved by the multilayered coating, there still remain considerable reduction of reflectivity in the EUV wavelength bands.

A geometric image blur is formed by the mirror. This error, calculated by a ray trace spot diagram showing that the spot diameter, which is a result of spherical aberration, has a slow degradation (i.e. the image blur varies with the mirror tilt to the field of view) as a function of field angle and mirror position.

The mirror mechanism has both a coarse movement and fine scan capability. While it travels (± 10 mm in the X direction), the motion changes the portion of the mirror that is obstructed by the support in front of the filter assembly, changing the area of mirror being exposed to radiation.

The slit/slot assembly causes vignetting of the long wavelength end of the 250-290 Å wavelength band. The CCD housing also causes vignetting for some mirror positions, which here is wavelength dependent for wavelengths greater than 272 Å.

The radiation is reflected from the mirror to a toroidal concave grating, one half (D shaped grating) for each band. To optimize the grating a ray tracing code was used, which provided the smallest average RMS spot size over the spectral bands of interest. The spot size is a result of aberration in the grating. Measurements show that the spot size is much more wavelength dependent for the long wavelength band then for the short one.

The effects discussed so far;

- Filter transmission
- Mirror reflectivity
- Image blur
- Assembly blocking
- Vignetting
- Grating efficiency, aberration

are all calculated and summed to give a graph of the total effective area for the EIS instrument in the two desired wavelengths bands, as seen on figure 3.7.

To calculate instrument performance, the number of photons entering the slit/slot assembly per second is required. For an ideal system with no losses, the equation

$$N_\lambda = \phi_\lambda A \frac{a}{f^2} \frac{1}{n_{pix}} \tag{3.2}$$

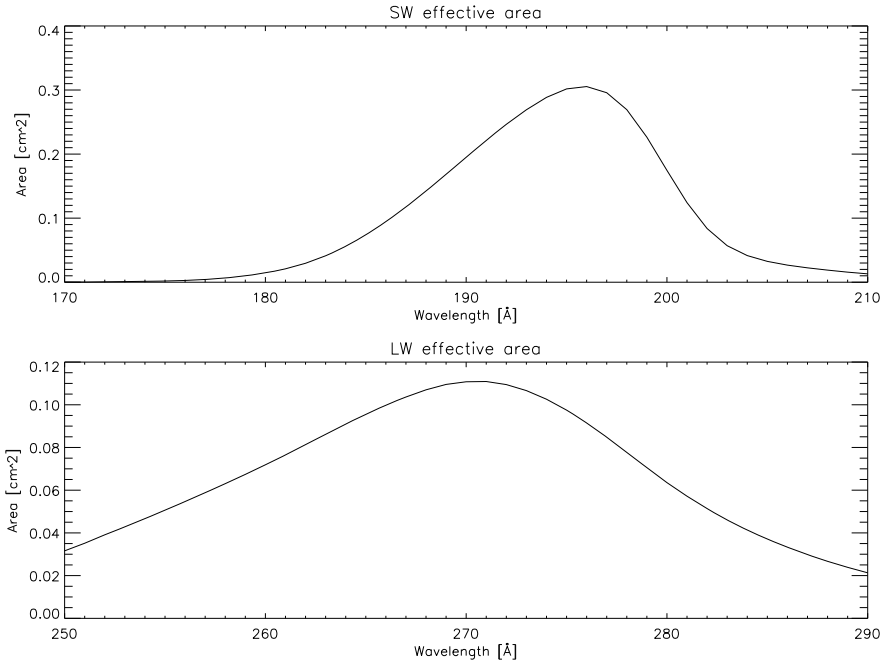

Figure 3.7: Efficiencies of the different optical elements (filters, mirror, grating, CCDs, vignetting) result in the effective area for the short wavelength band (LW) and long wavelength band (LW) presented in this plot.

represent the number of photons per second registered on a pixel of each CCD: ϕ_λ represents the photon flux from the solar radiation (photons $\mathrm{cm}^{-2}\mathrm{s}^{-1}$ sr^{-1}), A (cm^2) the mirror area, a (cm^2) the area of the slit (CCD pixel height times the with of the slit) and f the focal length of the mirror. n_{pix} represent the pixel density on the on the narrow slit.

While the plan was to have the narrow slit match the pixel size, the actual narrow slit widths turned out to be different, resulting in n_{pix} equal to 1.067 and 1.087 for the 1 arcsec wide slit, and 2.080 and 2.119 for the 2 arcsec wide slit for detector A and B, respectively. This gives the same solid angle ω_d subtended by a pixel for the to detectors, defined as $\omega_d = \frac{a}{f^2}\frac{1}{n_{pix}}$.

Considering the above effects it is clear that in describing the EIS optical system we must make a number of modifications to 3.2. The number of registered photons will therefore be reduced by the addition error factors due to front filter and spectrometer entrance filter transmission ($\mathrm{T}_{\mathrm{ff}}(\lambda)$ and $\mathrm{T}_{\mathrm{rf}}(\lambda)$), the fractional area of the front filter assembly that is blocked by supporting structural members $\mathrm{T}_{\mathrm{spider}}$, the reflectivity of the mirror $\mathrm{R}_m(\lambda)$, the grating efficiency $\mathrm{E}_g(\lambda)$, the vignetting $\mathrm{V}_d(\lambda)$ and the quantum efficiency $\mathrm{E}_{\mathrm{det}}(\lambda)$. The expression for the number of registered photons in each detector

pixel per second becomes

$$N_\lambda = \phi_\lambda A \omega_d T_{\rm ff}(\lambda) T_{\rm rf}(\lambda) T_{\rm spider} R_m(\lambda) E_g(\lambda) V_d(\lambda) E_{\rm det}(\lambda) \tag{3.3}$$

3.2 Conversion from DN to physical quantities

The apparatus area illuminated varies with the illumination source. The change of illumination from a small source filling a small part of the aperture to full solar illumination, as well as the effect of coarse movement of the mirror, contributes to the change in area. Therefore the apparatus area A ($\rm cm^2$) and the area A_S of the spectrometer slit/slot ($\rm arcsec^2$) illuminated by the incident radiation has to be a part of the conversion equation, for DN/sec to photon flux.

The digital signal in a spectrum line $\rm D_L$ (DN/sec) registered by the spectrometer, has to be corrected by the responsivity $\rm D_P$ (DN/photon) of the spectrometer obtained from a calibrated source (Culhane et al., 2007). The responsivity is derived from the effective area of the spectrometer as shown in figure 3.7. Resulting in the following equation for the conversion;

$$\phi_\lambda = \frac{D_L}{D_P}\frac{1}{A}\frac{1}{A_s}\left(\frac{180.0 \times 60.0^2}{\pi}\right)^2 \text{ photons cm}^{-2}\text{ s}^{-1}\text{ sr}^{-1} \tag{3.4}$$

where the factor $(\frac{180.0\times 60.0^2}{\pi})^2$ originates from the unit conversion from $\rm arcsec^2$ to sr.

3.3 Post-processing of the solar observations

The errors in observations due to instrument errors and inefficiencies such as mentioned in section 3.1.6 have all to be accounted for in the post processing treatment of the observed data. There are also additional errors such as cosmic radiation, dark current, and detector damage that should be corrected.

The EIS Quick Look program (QL) is a data analysis widget program that provides the user several functions for imaging, calibration and analysis of EIS data. This reduction of data is done by the QL, and the **eis_prep.pro** routine.

3.3.1 Data calibration

For a unprocessed file, we has the possibility of choosing the calibration definitions which will be performed on the data by pressing the **EIS Prep** button, where the definitions are as follows:

Dark current subtraction
There is a current in the CCD detectors when there is no radiation incident on the detectors, a so called Dark Current (DC). This extra signal will result in some reduced space in the potential well for the photoelectrons (see section 3.1.5). To compensate for this extra signal, the dark current is measured in the absence of radiation , saved in a file and then subtracted from the final signal. The user has the possibility of choosing between different correction files.

Hot pixels
There are some permanently lit pixels on the CCD detector, so called hot pixels (HP) and the less intense warm pixels (WP) that must be considered when calibrating the observations. These pixels are registered by recording without exposing the CCD and saved in a error file. During the post-processing this file is used one the observation data, making a new individual error file where the hot pixels are registered with the pixel value of -100, and set so not to be used in further calculations.

This individual error file containing error registrations is further removed from the observations, leaving empty pixels. The empty pixels are replaced by the median of the surrounding pixel values in the post-processed data so that the resulting observation image is approximately correct.

Saturated data registration
There are some cases where the the maximum signal (ND $\approx$ 14136) is saturated. Photons incident on the detector are not able to further produce electron pairs. The **EIS Prep** function register the saturated pixels and writes to the error file, marking these pixels with the value -100. Nothing is done to the image data by this process.

Dusty pixels
Under the assembly of the EIS Spectrometer there was some dust trapped in the optical paths of the radiation. The intensity is reduced in the area covered by a dust grain. **EIS Prep** marks the pixels exposed to dust hindering as bad and saved the pixel positions in the Error file with the value -100.

Cosmic ray removal
There is always the chance that the CCD detectors are struck by radiation from the cosmic background. This feature revels itself in the observed data by a pixel with much higher intensity then its neighbors. **EIS Prep** calls the **eis_despike** which removes cosmic ray spikes from the pixel data.

For few exposures (up to three) per raster position this function calls the routine **clean_exposure**, which identifies cosmic rays by comparing pixels with the median of the surrounding pixels inside a rectangular box. The cosmic ray struck pixel value is then changed to the median of the surround-

ing pixel value or by an already-identified missing data value. Otherwise the **new_spike** function is called, which identifies pixels that have a significant strength when compared with neighboring exposures. By checking the continuity in the brightening in the X and Y detector directions, we are able to differ between a cosmic ray and a strong natural Solar brightening. In addition this routine also compares a pixel value with the median value of a 5×5 array of pixels. The identified cosmic ray is replaced by the median value of its neighbors, and its position is marked with -100 in the Error file.

Absolute calibration
As discussed in section 3.1.6 there are some measurement errors due to optical and instrument performance. The responsivity D_P is calculated from the effective area of the spectrometer as shown in figure 3.7, so that we have a function of wavelength representing the amount of DN per photon registered in each pixel on the ccd. The correction is made by **EIS Prep**. Absolute calibration files are calculated for all the different errors accounted for in equation 3.3 and used to correct with by **EIS Prep**. For more information on the absolute calibration see *Culhane et.al,2007*.

3.3.2 Line fitting

Once the calibration has been done the different emission lines have to be fit to a line profile. Due to line broadening the emission of a particular line is smeared over a larger wavelength range, and not as a point source. Within this wavelength range there might also be other lines and thus the line may be blended. The intensity registered by the detector also play a crucial role as to how well we are able to define the line of interest. A continuum is always present.

The intensity amount registered is something we cannot do anything about, but the rest can be improved by a line fitting, where we try to define the line to a certain profile and remove the other artifacts. We may either calculate moments to the line profile or assume Gaussian fits.

Fit by Moments
The emission line and the continuum is defined through a line profile widget which further subtracts the continuum from the line. Physically relevant moments of the new defined line profile are then calculated. The moments calculated are described below.

- The zeroth moment is the line intensity integrated over the depth z.

$$M_0 = I_\nu = \int_0^z I_\nu(z)dz \tag{3.5}$$

- The first moment defines the mean line shift (Doppler effect) due to

relative velocities between the gas and the observer,

$$M_1 = \Delta\nu = \frac{\int I_\nu(\nu - \nu_0)d\nu}{\int I_\nu d\nu}, \tag{3.6}$$

where ν_0 is the original frequency of the line, and ν is the Doppler shifted line.

- The second moment is part of the line width due to Doppler broadening, defined as;

$$M_2 = \frac{\int I_\nu(\nu - \nu_0)^2 d\nu}{\int I_\nu d\nu}. \tag{3.7}$$

The width is the standard deviation between the first and second moment, measured in frequency;

$$\langle w \rangle = \sqrt{M_2 - M_1^2} \tag{3.8}$$

Gaussian fit
It is also possible to choose a Gauss, broadened Gauss or a Voigt profile to fit the mean line profile. If the profile is blended we can in principle separate the lines using a model of the blends. For the case of the Gaussian profile one uses

$$I(\nu) = a\ \exp(\frac{(\nu - b)^2}{2c^2}) \tag{3.9}$$

where a represent the amplitude or maximum intensity, b is the position of the line center and c is the line width.

3.4 Raster observations

Now that observational apparatus, field of view and post processing has been discussed it is time to present raster observations obtained during a one week period,01-07/12/07, from the Japan Aerospace Exploration Agency (JAXA) at the Institute of Space and Astronautical Science (ISAS). The chief observer was Viggo Hansteen, with assistance by Kosovare Olluri. The raster observations are presented in table 3.2 with the raster specifications in table 3.3.

Raster acronym	**First raster obs.**	**Last raster obs.**	**NOAA nr.**	**nr. of obs.**	FOVX	FOVY	NWIN
HH_FWHM_CAL_Norikura	2007-12-01 11:19:41	2007-12-04 19:06:13	10976	13	179.712	512.0	25
HH_FWHM_CAL_Norikura	2007-12-05 00:14:40	2007-12-07 11:26:44	10977	15	179.712	512.0	25
HH_FWHM_CAL_Norikura	2007-12-06 18:03:13	2007-12-07 22:33:43	10978	3	179.712	512.0	25
HPW004_QS_RAST_120m	2007-12-04 04:00:40	2007-12-02 02:15:06	10976	7	127.795	512.0	17
HPW004_QS_RAST_120m	2007-12-07 01:15:13		10977	1	127.795	512.0	17
Romano_v2	2007-12-01 16:00:19	2007-12-03 19:00:42	10976	9	359.424	512.0	5
Romano_v2	2007-12-05 16:03:13	2007-12-07 18:08:13	10977	7	359.424	512.0	5
DRW_CLBRT_SCAN_5as	2007-12-02 07:11:11	2007-12-02 09:54:55	10976	32	4.992	240.0	20
Detailed_AR_map	2007-12-04 10:24:23		10976	1	329.472	304.0	21
CAM_ARTB_RHESSI_b_2	2007-12-04 22:20:33	2007-12-04 23:03:33	10976	12	39.936	144.0	22
CAM_ARTB_RHESSI_b_2	2007-12-05 04:32:26	2007-12-05 05:07:37	10977	10	39.936	144.0	22
CAM_ARTB_RHES_b_2_HI	2007-12-03 14:47:55	2007-12-03 22:15:01	10976	51	39.472	368.0	22
CAM_ARTB_RHES_b_2_HI	2007-12-06 00:25:24	2007-12-06 01:40:28	10977	20	39.472	368.0	22
CAM_AR_LIMB_V1	2007-12-06 19:00:26	2007-12-06 21:21:40	10978	2	359.424	512.0	24
DRW_CLBRT_SCAN_5"_v2	2007-12-05 12:34:43	2007-12-07 22:18:04	10977	165	4.992	240.0	20
AR_230x360_30s_s1	2007-12-04 10:20:34		10976	1	227.635	360.0	24

Table 3.2: Raster observations using the EIS spectrometer onboard the HINODE satellite. Observations were made during the period 2007/12/01-2007/12/07. (FOVX:Field of view in Solar X (arcsec), FOVY:Field of view in Solar Y (arcsec), NWIN:Number of line windows)

Raster acronym	**Spectral windows**	**Nr of unique raster positions**	**Mirror step nr**	**Nr of exposures**	**Exposure time**
HH_FWHM _CAL_ Norikura	25	60	12	60	50 s
HPW004_ QS _RAST_ 120m	17	128	4	128	60 s
Romano_ v2	5	360	4	360	10 s
CAM_ ARTB_ RHESSI_ b_ 2	22	20	8	20	10 s
CAM_ ARTB_ RHES_b_ 2_HI	22	20	8	20	10 s
DRW_ CLBRT_ SCAN_ 5”_ v2	20	5	4	5	30 s
DRW_ CLBRT_ SCAN_ 5as	20	5	4	5	60 s
AR_ 230×360_ 30s_ sl	24	6	152	6	30 s
Detailed_ AR_ map	21	330	4	330	40 s
CAM_ AR_ LIMB_ V1	24	180	8	180	45 s

Table 3.3: Raster specifications for the raster acronyms mentioned in table 3.2. Each mirror step is $\sim$ 0.125arcsec in size.

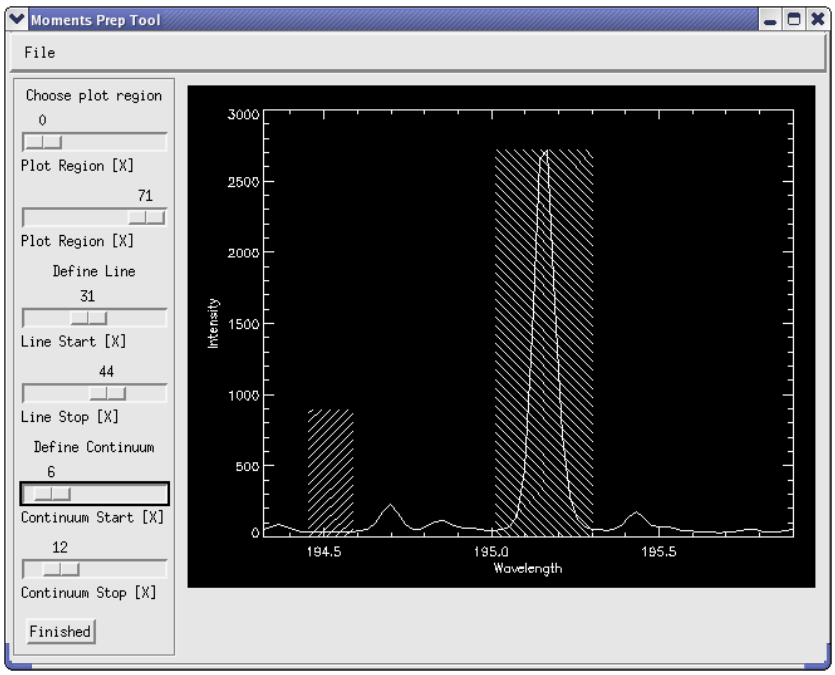

Figure 3.8: The *eis_prep moments* widget, which displays the intensities a function of wavelength, here displaying the Fe 195.120 Å line profile with the continuum and spectrum line defined.

3.4.1 Intensity maps and calculations

The reduced data are stored in FITS (Flexible Image Transport System), which is a data format designed to provide a means for convenient exchange of astronomical data between installations whose standard internal formats and hardware differ. The files contain all the necessary data as listed in table 3.2 and 3.3. Each file is then read in to a data object, which the EIS software manipulates to extract relevant data.

From the object we are able to retrieve the number of line windows, line ids, positions, lengths, intensities and so on for that specific raster. A routine *comp_int* which takes as input the data object and an array containing the line window numbers of interest is run. This routine returns intensity maps for the lines of choice, as well as a data file containing line data for each line window.

For each chosen line window the line profile and continuum pixels are defined, using the *eis_prep moments* widget program as displayed in figure 3.8, (which is a part of the EIS data analysis software). The intensities are

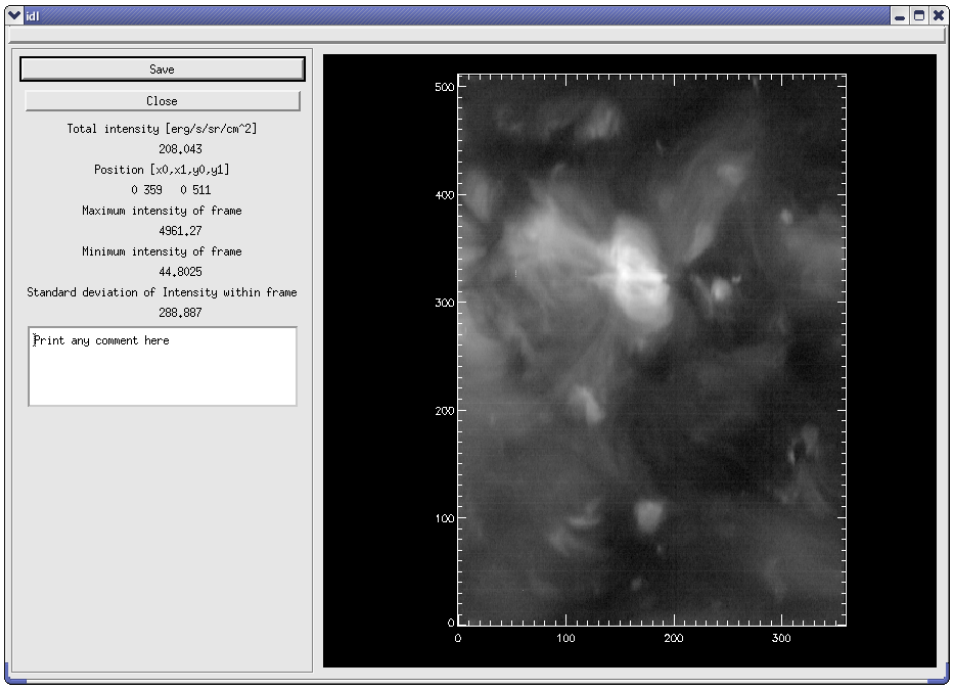

Figure 3.9: The *intdisplay* widget, were the user can choose a specific region within the intensity map for which line data are calculated.

integrated for these wavelength regions; the total intensity of the line is then defined as

$$I_{tot} = \int (I_\lambda - I_{cont}) \mathrm{d}\lambda, \tag{3.10}$$

where the continuum intensity is

$$I_{cont} = \frac{\int I_{cont} \mathrm{d}\lambda}{\Delta\lambda_{cont}} \tag{3.11}$$

After the total intensity has been computed, a widget function *'intdisplay'* as shown in figure 3.9 is developed, making it possible to define regions of interest within a intensity map. This widget displays a intensity map of the observed data, along with data values (position, mean-, maximum-, minimum- intensity and standard deviation) of the chosen region in the display window. The data values can be saved to file or one can choose a better region of interest before saving the data. The file also contains the time of the observation and the filename of the raster file. The *intdisplay* function

defines the region of interest for the first line only, after which the following lines use the same position values to calculate new intensity data. The new data is appended to the first line data file, resulting in a line data file for each raster.

3.5 Results

Table 3.3 displays spectral windows observed, all of which are interesting for coronal and transition region study. Unfortunately some of the spectral lines listed are blended and therefore not appropriate for our purposes. Other spectral lines are too weak. Therefore we confine attention to a set of strong, well defined lines which cover a large temperature range, displayed in table 3.4.

Ion	λ_{obs} (Å)	T_{max}
Fe X	184.540	6.0
Fe VIII	185.250 (185.210)	5.9
Fe X	190.040	6.0
Fe XII	195.120	6.2
He II	256.320	4.9
Mg VI	269.000	5.7
Mg VI	269.800	5.7
Si VII	275.350	5.8
Fe XV	284.160	6.3

Table 3.4: Selected spectral lines covering a large temperature range. The temperatures displayed in logarithmic values are given by CHIANTI.

Intensity maps displaying the emergent intensity in the different wavelengths and for the different raster types are made, making it possible to define subregions within an intensity map. Examples of the intensity maps are displayed in figure 3.12 and 3.13.

For each intensity map three subregions are marked, one for the active region and two for the quiet Sun region. This makes it possible to study the intensity variations within the same regions as a function of time. A set of subregion definitions is needed for each raster type, since the area (field of view) covered by the different raster types differ.

For each subregion the mean intensity, maximum intensity, minimum intensity and standard deviation are calculated for the spectral lines listed in table 3.4. Figure 3.12 and 3.13 show intensity maps with the subregion definitions marked for the Romano_v2 and the HPW004_QS_RAST_120m raster, respectively. The subregion definitions differ between the two NOAAs for the same raster type, as displayed for raster HPW004_QS_RAST_120m,

where the definitions for the Si VII 275.350 Å map on figure 3.12 differ from the subregion definitions on figure 3.13.

On table 3.2 all the raster observations are divided into their respective NOAA number. For NOAA 10978 we only have 5 observations, and therefore choose not to look further into this dataset because of the lack of data amount. We present the data for the mean intensity for these lines in figure 3.28 to 3.16 for NOAA 10976, and figure 3.29 to 3.17 for NOAA 10977.

3.5.1 Intensity maps

An active region, such as NOAA10976, is a result of a magnetic flux consentration in a particular area of the solar surface. The magnetic field is formed by two nearby magnetic poles of opposite polarity. A magnetogram made by the SOT (Solar Optical Telescope on Hinode) team dated December 1st 2007 12:01:34 UT is displayed on the left side in figure 3.10. The magnetic poles are positioned within -550 arcsec to -490 arcsec in solar x and -140 arcsec to -170 arcsec in solar y, which is within the NOAA 10976 active region area shown in figure 3.12. We observe the same area in Ca II H (dated December 1st 2007 12:01:53 UT, using SOT), displayed on the right hand side in figure 3.10. The Ca II H line emerges from the upper photosphere and chromosphere, where we see reverse granulation in the quiet Sun, and two small pores just above the magnetic poles, which are surrounded by a

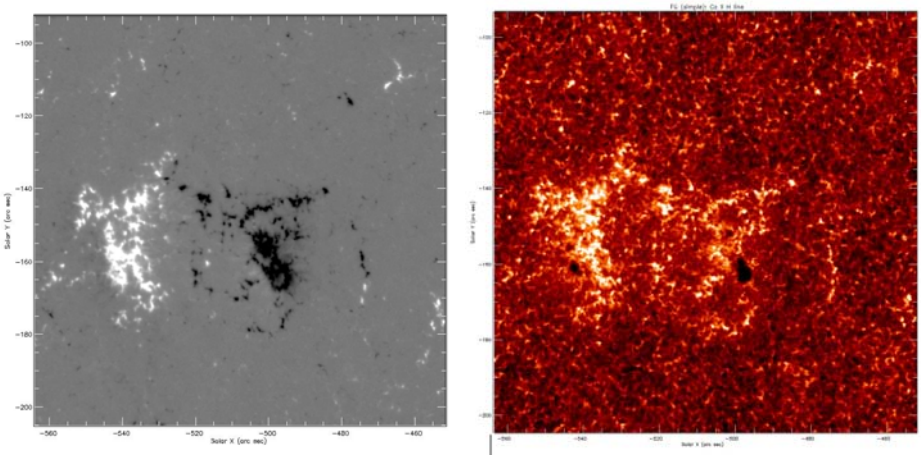

Figure 3.10: The magnetic poles beneath the active region NOAA 10976 displayed on the left image, and NOAA 10976 observed in Ca II H spectral window. The observations are made by the Solar Optical Telescope (SOT) onboard Hinode. The magnetogram is dated December 1st 2007 12:01:34 UT and the Ca II H image is from December 1st 2007 12:01:53 UT.

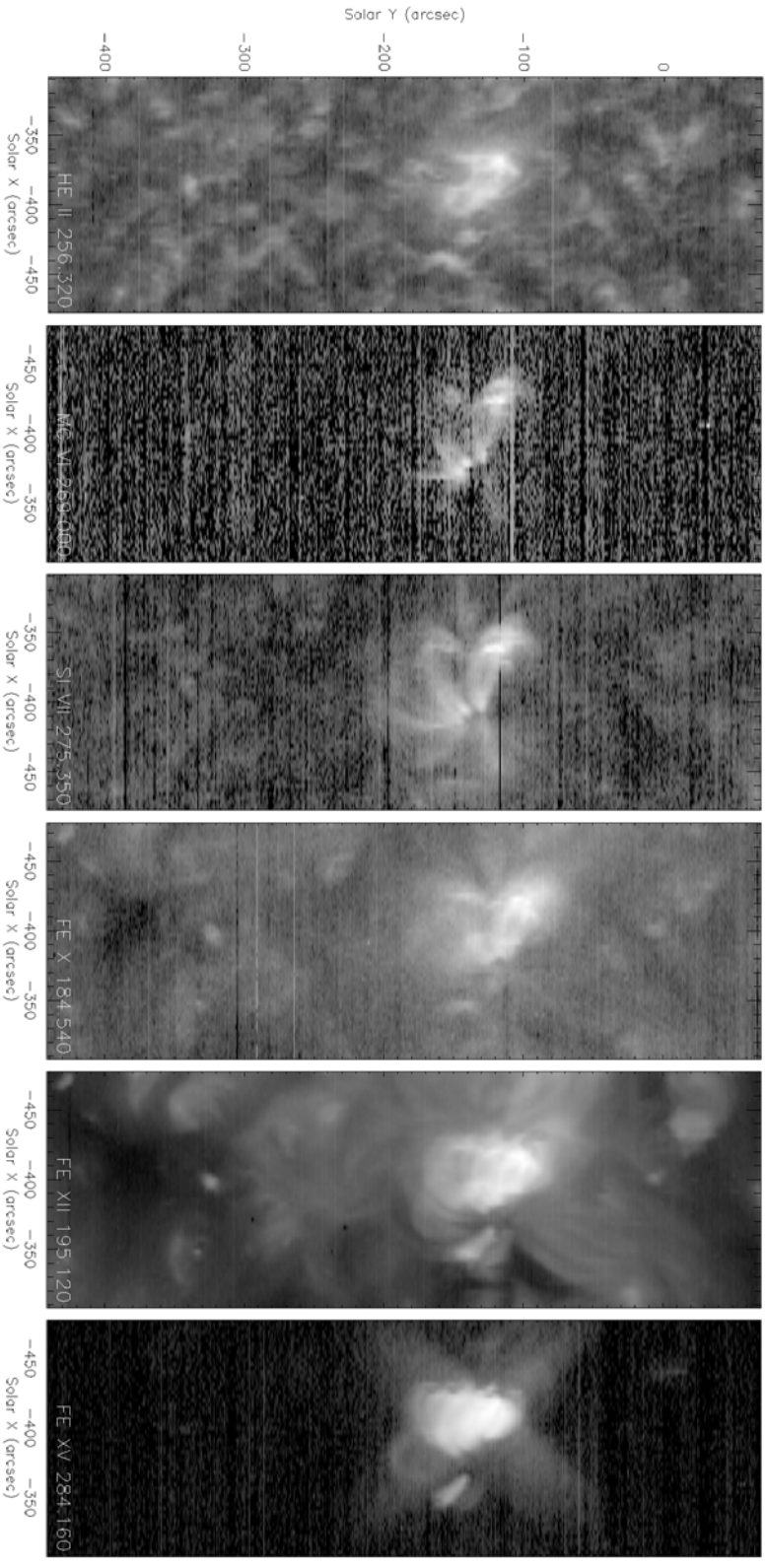

Figure 3.11: Intensity maps for some of the spectral lines emerging from the solar atmosphere for NOAA nr. 10976. The maps are arranged according to temperature of $\log T$; 4.9, 5.7, 5.8 , 6.0, 6.2 and 6.3, respectively.

bright area of high intensity. We clearly see that the highest intensity within the observational frame is above regions of high magnetic flux.

The intensity maps (see figure 3.11) show features of the differing layers of the outer solar atmosphere, including the upper chromosphere/solar transition region and the corona, where the intensity maps are lined up with increasing temperature. Starting with the He II 256.320 Å line, which is the coolest ion investigated ($\log T = 4.9$), we see both aspects typical of both the chromosphere and the overlying corona. In the dimmer, quiet Sun, regions of the He II map we find structures with spatial scales typical of the supergranular network - *i.e.* some 20 Mm. Comparisons with SOT magnetograms as well as images formed in the Ca II H line show that the He II emission is relatively bright where the magnetic field in the underlying photosphere is strong. The active region (NOAA 10976 in figure 3.12) stands out clearly as a region of high intensity, right above an area of strong magnetic field measured in the photosphere, is clearly distinguishable form the supergranular patches in the quiet Sun.

As the line formation temperature rises, the supergranular pattern evident in He II fades and has almost disappeared in the Mg VI lines formed in the upper transition region ($\log T = 5.7$). In this relatively weak line, only the active region has clearly evident structures in intensity. Continuing upwards the transition region lines of Si VII 275.350 Å and Fe VIII 185.250 Å, which are formed at temperatures of $\log T = 5.8$ and $\log T = 5.9$, display no supergranular patterns, but have a bright active region with clear, visible magnetic loop structures stretching from one side of the active region to the other, parallel to the solar X axis, spreading out in the southward direction The quiet Sun regions for these lines show no particular outstanding features.

In the coronal lines from $\log T = 6.0$ and beyond, we see the well defined loops increase in width and intensity, evolving to an envelope of loops from one side to the other of the active region.

The coronal line of Fe XII 195.120 Å is strong, and the active region is well defined in the intensity map. For this reason we choose the intensity maps from this line to define quiet Sun and active Sun sub regions. These are marked '2, 3' (quiet Sun) and '1' (active region) as shown in figure 3.12 and figure 3.13. These definitions are then used for the remaining lines from an given raster. We use two quiet Sun areas to better be able to do a comparison with the active region.

NOAA 10976

An intensity map of the He II 156.320 Å line is displayed on the left frame in figure 3.12. This observation was made on December 1st 2007 at 16:00:19 UT using the raster type Romano_v2. The frame displays a large field of view of 350 arcsec×371 arcssec, -295 arcsec to 644 arcs in solar x, and -441 arcsec to 70 arcsec in solar y. The map is displayed in logarithmic intensity

values to better see the emerging patterns.

This intensity map shows a clear super granular pattern, spread out approximately uniformly in the quiet Sun environment surrounding the active region. On this map the active region is identified as NOAA 10976 positioned between -431.35 arcsec to -484.813 arcsec in solar x, and -156.282 arcsec to -95.2816 arcsec in solar y, as shown on the left frame in figure 3.12.

At higher temperature in the atmosphere the remaining ions are created,

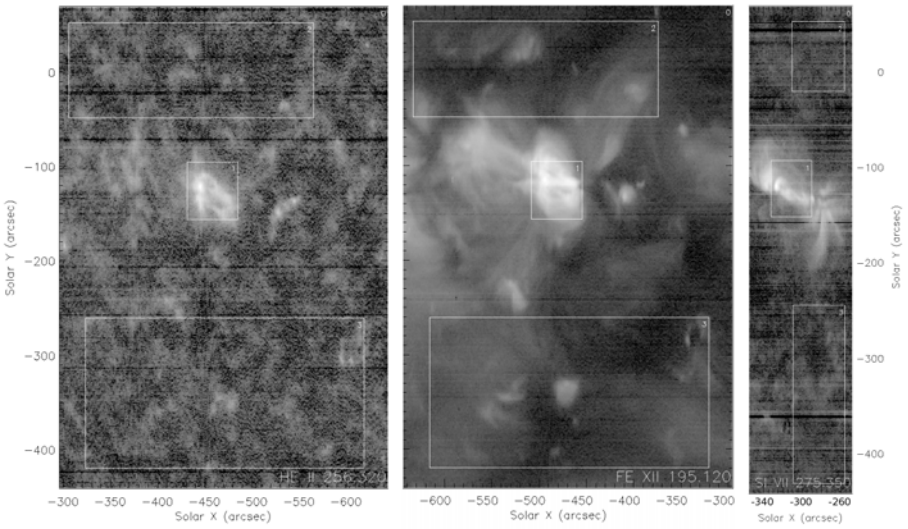

Figure 3.12: Intensity maps using Romano_v2 raster type for (left) He II 256.320 Å and (middle) Fe XII 195.120 Å from December 1st 2007 at 16:00:19 UT , and raster type HPW004_QS_RAST_120m on (right) Si VII 275.350 Å from December 2nd 2007 at 11:10:44 UT, displaying NOAA 10976 .
0: Entire Observation Frame, 1: Active Region, 2: Quiet Sun, 3: Quiet Sun

continuing with Si VII 275.350 Å, shown in on the right frame in figure 3.12. Here the raster type HPW004_QS_RAST_120m is used giving a close up of the NOAA 10976. This particular intensity map is defined in solar x from -248 arcsec to -355 arcsec, and solar y from -441 arcsec to 70 arcsec, observed on December 2nd 2007 at 11:10:44 UT. NOAA 10976 subregion is defined from -270 arcsec to -313 arcsec in solar x coordinates and -150 arcsec to -91 arcsec in solar y coordinates. As we see the field of view has shifted to more positive solar x values, a result of the solar rotation.

The Si VII 275.350 Å line is formed at $\log T$=5.7, representing the lower corona. We observe magnetic loop structures emerging from $\sim$ - 150 arcsec in solar y direction. The active region defined as (1) in the intensity map

seem to be outside the strongest intensity region in the Si VII 275.350 Å intensity map. The quiet Sun intensity values for the Si VII 275.350 Å line are very low and approximately constant, giving no particular outstanding features in the quiet Sun.

One of the strongest spectral lines detectable by EIS is the Fe XII 195.120 Å line. This line is formed at a temperature of $\log T = 6.2$. An intensity map of this line is displayed on the middle frame in figure 3.12, observed at the same time and position as the He II 256.320 Å line, and therefore has the same active region definitions. The intensity map show many intensity structures. We observe large structures of high intensity throughout the quiet Sun. These structures are within the quiet Sun definitions marked as (2) and (3) in the intensity map as well. The active region clearly stands out as the strongest region.

We see high activity in intensity structures surrounding the active region. The intensity emerging from the ions trapped by the magnetic field lines are very visible, forming loop structures.

NOAA 10977

Intensity maps of NOAA 10977 are displayed in figure 3.13. We have chosen to discuss the same spectral windows as for NOAA 10976 because these lines span a temperature range from the transition region to the corona, starting with the He II 256.320 Å which is our coldest line formed at $\log T = 4.9$ to Fe XII 195.120 Å, which is one of the hottest, formed at $\log T = 6.2$.

The intensity maps displayed in figure 3.13 are from observations made on December 7th 2007, at 01:15:13 UT, using the HPW004_QS_RAST_120m raster type.

The He II 256.320 Å spectral window displays (see left frame in figure 3.13) a similar structure in quiet Sun as the He II 256.320 Å intensity maps does, for NOAA10976 on the left frame in figure 3.12, clearly observing the super granular pattern emerging as high intensity patches. The active region identified as NOAA 10977 is quite dynamic, spreading out from approximately 10 arcsec to 65 arcsec in solar x and -140 arcsec to -20 arcsec i solar y, where we only have used the area of highest intensity to define the subregion marked with (1) in the intensity map of He II 256.320 Å. The active region seems to be divided into two main parts, with a connecting point in between at approximately -80 arcsec in solar y. We observe two intensity loops emerging from the the magnetic poles on the solar surface. One small extending in the positive Solar y direction and a larger one extending in the negative solar y direction.

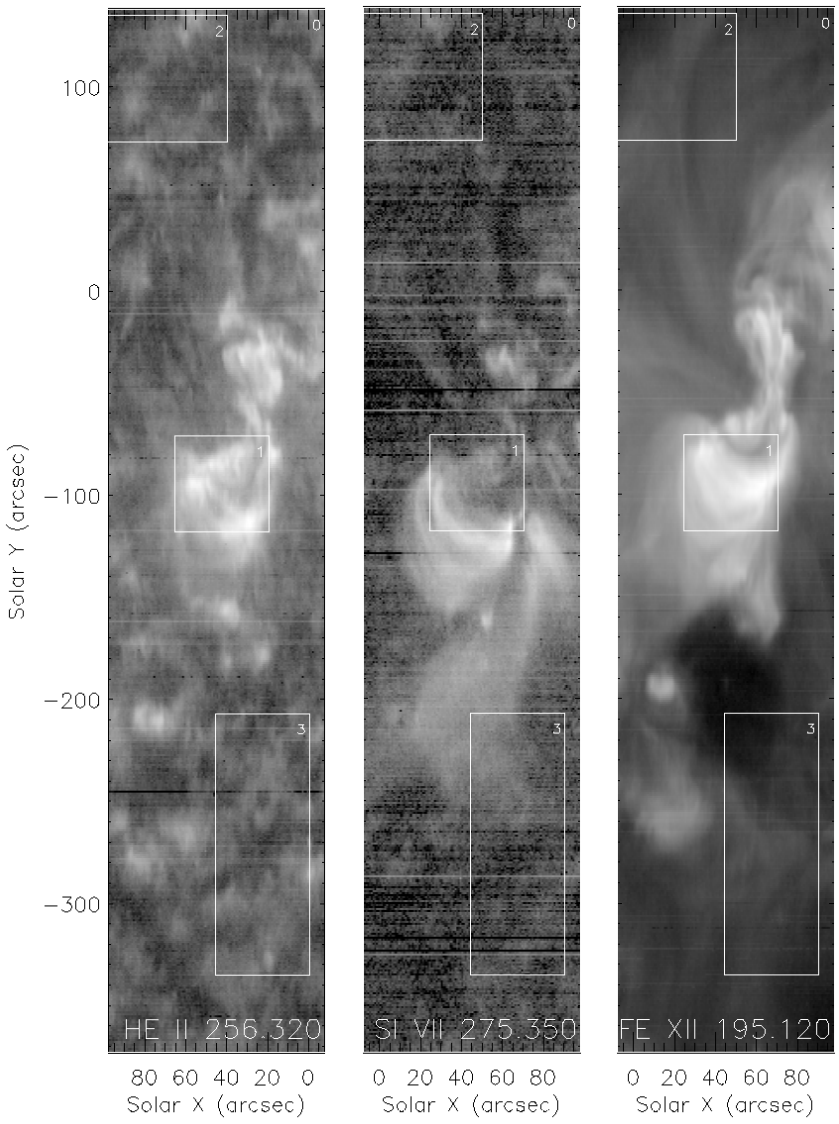

Figure 3.13: Intensity maps using HPW004_QS_RAST_120m, values in units of ergs cm^{-2} s^{-1} sr^{-1}. The intensity maps are from December 7th 2007, at 01:15:13 UT, displaying NOAA 10977 .
0: Entire Observation Frame, 1: Active Region, 2: Quiet Sun, 3: Quiet Sun

When observing the intensity map of the Si VII 275.350 Å line in the middle frame in figure 3.13, we see many intensity features emerging from the active region. The magnetic loop on the lower part of the connecting point mentioned above has clear loop structures, as well as a another loop

structure beneath this, on the right side, with a foot-point in the active region and the other presumably outside the observation frame.

While the smaller loop observed in He II 256.320 Å, seem to be vanishing in this spectral window. The active region marked with (1) for this particular raster is quite off for the Si VII 275.350 Å line, where the area of highest intensity is on the outside of this box. This because the subregion definitions are made using the Fe XII 195.120 Å intensity map, and the Si 275.350 Å emits the strongest in another area then the Fe XII 195.120 Å line.

There are only faint features in the quiet Sun, just like there were for NOAA 10976 in this spectral window. One thing worth noticing is that the area in the quiet Sun marked as (3), with a high intensity structure from the active region in the quiet Sun frame. This might lead to small intensity deviations when comparing the different line intensities in the upcoming section and the following chapters. This probably is a feature of the selection method which reappears in other lines as well, resulting in many misleading intensity values for the different ions selected.

An intensity map of the Fe XII 195.120 Å line is shown in the right frame in figure 3.13, where we see large structures throughout the intensity map. The active region structures discussed for the He II 256.320 Å map emerge here as lobes of high intensity stretching out in an area of approximately 200 arcsec×100arcsec. The area marked as the active region (1) seems to be a small part of the NOAA 10977, where only the area of the highest intensity is marked. This might lead to a high intensity result when calculating mean values in the upcoming section.

We also observe large, faint loops of non-quiet Sun intensity in the upper part of NOAA 10977. Because of the generic subsection selection, this part is marked as quiet Sun, which might lead to intensify values higher than expected in this subregion (2).

3.5.2 Intensity variations with time

Intensity maps such as these discussed above, help us define the active region and the quiet Sun for further investigations. After such a selection, the intensities are calculated for the specific region for all the raster observations of the same type. As we see in the intensity maps from 3.12 the definitions are not exactly the same between to different rasters. This turned out to be a problem when comparing the intensity in chapter five.

The intensity from the different subregions within a intensity map, is dependent on the field of view, which is defined by the raster types of the observations. The subregions are defined in the first observation and used for the entire observational period. This might result in intensity jumps between the observational sequences as stated in figure 3.17. An effect which is visible in all the resulting intensity plots. These discrepancies are a result of the

fact that the subregions are defined by visual inspections. Regions which are seemingly the same are marked and then used for the intensity calculations.

Observational sequences with strong deviations are recalculated with new subregion definitions. This is done in order to obtain the best subregion fit. However, the discrepancies are still present. In particular, this is necessary for the observational sequence at $t = 53h$ and $t = 70h$for NOAA 10977.

The following plots display the intensity variations with time, where the active region, entire observational frame and quiet Sun are marked with '+', '$\cdot$', '$*$' and '$\diamond$', respectively. There are to set of quiet Sun intensities ('$*$' and '$\diamond$'), giving us another set of data, and therefore a better basis for comparison.

He II 256.320 Å

The mean intensities with the defined subregions are plotted in figure 3.14 and 3.14, for NOAA 10976 and NOAA 10977, respectively. We observe that the quiet Sun intensity is approximately constant for both NOAAs, with an average intensity $\sim$200 ergs $s^{-1}cm^{-2}sr^{-1}$, except for some deviations (at $t = 3.8 \cdot 10^3$ and $t = 5.8 \cdot 10^3$s) which seem to be a result of the raster type used in the observation sequence for NOAA 10977. The active region intensity reaches a value $\sim$1500 ergs $s^{-1}cm^{-2}sr^{-1}$ but generally decreases in intensity over time, ending at 650ergs $s^{-1}cm^{-2}sr^{-1}$. For NOAA 10977 there are some measurements standing out in the active region at $\sim$53 h and at $\sim$ 70 h. If this is a recurring tendency evident in the other spectral lines as well, this may be an error due to the active region definition and may be dropped to get a more realistic comparison basis.

Mg VI 269.800 Å

For the Mg VI 269.800 Å we have a three hour long observation sequence for NOAA 10976 (figure 3.16), while there are four such sets for NOAA 2=10977 (figure 3.17), distributed over a time period of 60 hours. The quiet Sun intensities are approximately constant over time for both NOAAs, with a value of $\sim$10 ergs $s^{-1}cm^{-2}sr^{-1}$. For the active regions, we observe time variation in the intensities, varying between 250 ergs $s^{-1}cm^{-2}sr^{-1}$ and 450 ergs $s^{-1}cm^{-2}sr^{-1}$. We see the same intensity discrepancies as observed for the He II 256.320 Å line.

Mg VI 269.000 Å

The EIS observations give a very low representation for Mg VI 269.000 Å line, both in quiet Sun and active region when observing NOAA 10976 and NOAA 10977, as displayed in figure 3.18 and figure 3.19. The quiet Sun intensity for this line are $\sim$ 3 ergs $s^{-1}cm^{-2}sr^{-1}$ for both NOAA 10976 and NOAA 10977, while the active region intensities lies between 5.0 ergs $s^{-1}cm^{-2}sr^{-1}$ and 25.0 ergs $s^{-1}cm^{-2}sr^{-1}$. Even though the active region intensities are varying, we see a clear decrease in intensity over time.

Si VII 275.350 Å
For the Si VII 275.350 Å line the intensity values for quiet Sun lie at ∼20 ergs $s^{-1}cm^{-2}sr^{-1}$ for both NOAA 10976 and 10977 (figure 3.20 and 3.21), while the active region intensities fluctuate over time. For NOAA 10976 there seems to be some deviations form the otherwise falling intensity in the time interval between 50 h and 60 h. Overall the intensity fall during the observation period, from ∼ 150 ergs $s^{-1}cm^{-2}sr^{-1}$ to ∼ 50 ergs $s^{-1}cm^{-2}sr^{-1}$. While for NOAA 10977 the fluctuations are evident throughout the observation period, with an overall fall in active region intensity from ∼ 120 ergs $s^{-1}cm^{-2}sr^{-1}$ to ∼ 30 ergs $s^{-1}cm^{-2}sr^{-1}$.

Fe VIII 185.250/185.210 Å
For NOAA 190976 (figure 3.22) the quiet sun intensities are approximately constant at 30 ergs $s^{-1}cm^{-2}sr^{-1}$, while the intensity increase for NOAA 10977 in the quiet Sun region (figure 3.23). This is most probably an effect of the raster type and with the difficulties of defining subregions within an intensity map. This raster problem is also present when evaluating the active region, but because of the intensity fluctuations give a mean intensity of ∼ 200 ergs $s^{-1}cm^{-2}sr^{-1}$ for both NOAA 10976 and NOAA 10977. We observe an increase in intensity for NOAA 10976, but because the observation sequence is relatively short, this may only be an effect due to overall active region fluctuations. For NOAA 10977 there is an observation sequence at 70 h which differ from the other active region intensities. This is the same observation sequence as mentioned for the Mg Vi 269.800 Å and He II 256.320 Å.

Fe X 190.040 Å
The intensity from the Fe X 190.040 Å line is in general low according to the EIS observations as displayed in figure 3.24 and figure 3.25 for NOAA 10976 and NOAA 10977, respectively. The quiet Sun values are of approximately 30 ergs $s^{-1}cm^{-2}sr^{-1}$, but differ between the two quiet Sun regions. The active region intensities decrease over time, from ∼ 250 ergs $s^{-1}cm^{-2}sr^{-1}$ to ∼ 100 ergs $s^{-1}cm^{-2}sr^{-1}$ for NOAA 10976 and , from ∼ 200 ergs $s^{-1}cm^{-2}sr^{-1}$ to ∼ 100 ergs $s^{-1}cm^{-2}sr^{-1}$ for NOAA 10977. There are fluctuations in intensity for both quiet Sun and active region values.

Fe X 184.540 Å
The observations show a similar intensity progression for the Fe X 184.540 Å line as for the Fe X 190.040 Å line, as figure 3.26 and figure 3.27 shows, for NOAA 10976 and NOAA 10977, respectively. The intensity from the Fe X 184.540 Å line is approximately two times larger than the Fe X 190.040 Å intensity.

The quiet Sun intensity is different for the two different quiet Sun regions,

with an average value of 100 ergs $s^{-1}cm^{-2}sr^{-1}$. The intensity from the active region decreases from $\sim$ 550 ergs $s^{-1}cm^{-2}sr^{-1}$ to 250 ergs $s^{-1}cm^{-2}sr^{-1}$ for NOAA 10976 and from $\sim$ 450 ergs $s^{-1}cm^{-2}sr^{-1}$ to 200 ergs $s^{-1}cm^{-2}sr^{-1}$ for NOAA 10977, with some fluctuations in the active region throughout the observation.

Fe XII 195.120 Å

The quiet Sun intensities are approximately constant for both NOAA 10976 and NOAA 10977 as displayed in figure 3.28 and figure 3.29, respectively, with a value $\sim$120 ergs $s^{-1}cm^{-2}sr^{-1}$.

For the active regions the intensities fluctuate with time. There seem to be some deviation from the trend for some observational sequences for NOAA 10976, with an overall fall in intensity over time, varying from $\sim$ 2500 ergs $s^{-1}cm^{-2}sr^{-1}$ to $\sim$ 1000 ergs $s^{-1}cm^{-2}sr^{-1}$. While for NOAA 10977 the intensities decrease from $\sim$ 2000 ergs $s^{-1}cm^{-2}sr^{-1}$ to $\sim$ 1000 ergs $s^{-1}cm^{-2}sr^{-1}$, with the same observation sequence at $\sim$ 70 h giving error values as mentioned before.

The Fe XII 195.120 Å line is one of the strongest spectral lines detected by EIS. Formed at $\log T = 6.2$K this represent a corona line. The high intensity observed for this line indicate that the active regions result in coronal emission.

Fe XV 284.160 Å 6.3

We observe that the error observational sequence at $\sim$ 70h for NOAA 10977 (figure 3.31) is evident for the Fe XV 284.160 Å line as well. We also observe that the same deviations hold for the Fe XV 284.160 Å line as for the Fe XII 195.120 Å line in NOAA 10976 (figure 3.31).

Quiet Sun intensities seem to be nearly constant over time, with values $\sim$ 50 ergs $s^{-1}cm^{-2}sr^{-1}$ and 150 ergs $s^{-1}cm^{-2}sr^{-1}$ for NOAA 10976 and 10977, respectively.

The Fe XV 284.160 Å line is strong in the active region, with intensities decreasing in time. For NOAA 10976 the intensity decrease from $\sim$ 4000 ergs $s^{-1}cm^{-2}sr^{-1}$ to $\sim$ 2000 ergs $s^{-1}cm^{-2}sr^{-1}$, twice as strong at the Fe XII 195.120 Å line. For NOAA 10977 the intensity $\sim$ 5000 ergs $s^{-1}cm^{-2}sr^{-1}$ to $\sim$ 3000 ergs $s^{-1}cm^{-2}sr^{-1}$.

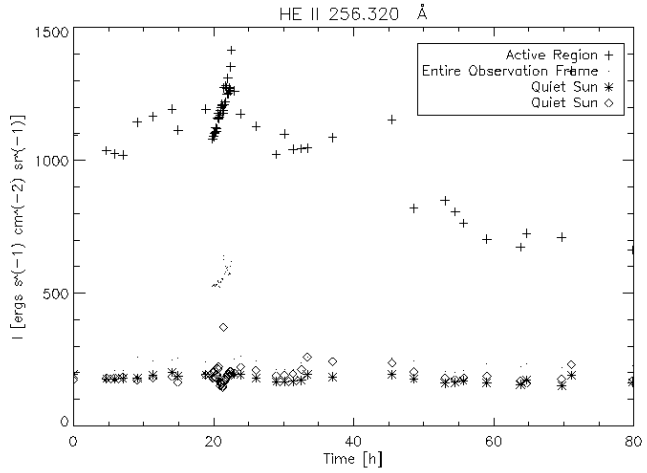

Figure 3.14: NOAA nr. 10976: The mean intensity for He II 256.320 Å, as a function of time. We observe a constant quiet sun intensity of 200 ergs $s^{-1}cm^{-2}sr^{-1}$ while the active region intensity decrease from a maximum of 1400 ergs $s^{-1}cm^{-2}sr^{-1}$ to a minimum of $\sim$ 650 ergs $s^{-1}cm^{-2}sr^{-1}$.

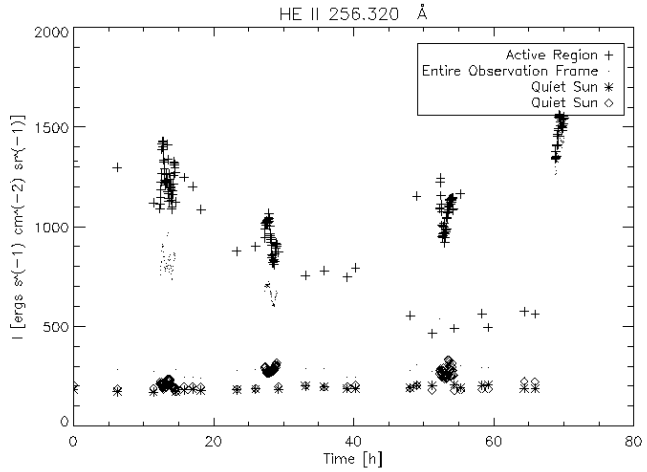

Figure 3.15: NOAA nr. 10977: The mean intensity for He II 256.320 Å as a function of time. The quiet sun intensities are constant in time ($\sim$ 200 ergs $s^{-1}cm^{-2}sr^{-1}$), except for some deviations which seem to be a result of the raster type used in the observation sequence, because the active region values over the same time period also differ from the trend. We observe a decreasing trend in intensity, from 1500 ergs $s^{-1}cm^{-2}sr^{-1}$ to $\sim$ 500 ergs $s^{-1}cm^{-2}sr^{-1}$.

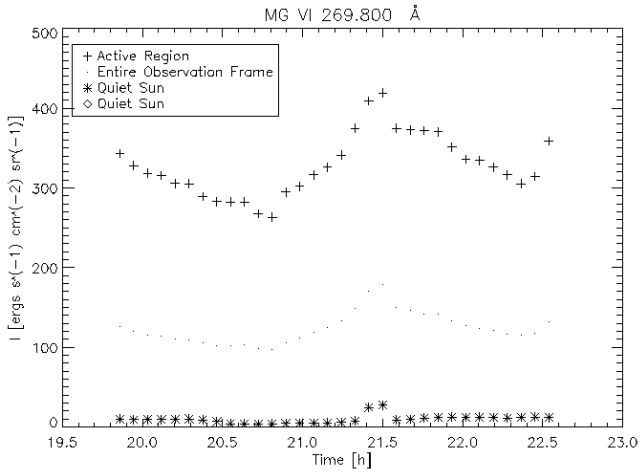

Figure 3.16: NOAA nr. 10976: The mean intensity for Mg VI 269.800 Å over a period of three hours. We observe a constant quiet Sun intensity of $\sim$10 ergs $s^{-1}cm^{-2}sr^{-1}$, while the active region intensity fluctuate with time between $\sim$ 200 and 420 ergs $s^{-1}cm^{-2}sr^{-1}$.

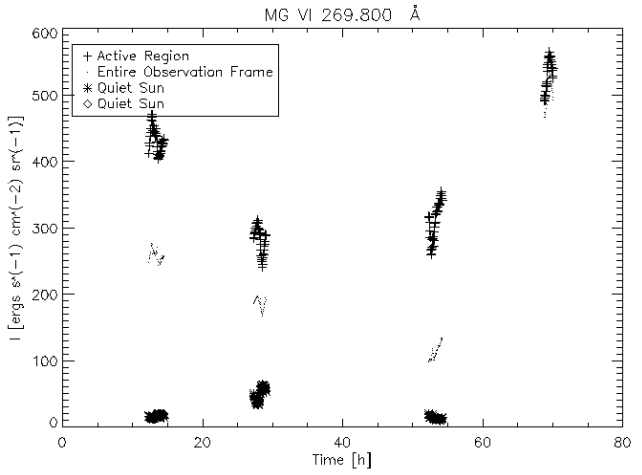

Figure 3.17: NOAA nr. 10977: The mean intensity for Mg VI 269.800 Å over four observation sequences. Notice the same deviation sequence as for He II 256.320 Å, if we ignore this observation sequence, the active region intensity seem to decrease in time, from a maximum value of $\sim$ 500 to a minimum of $\sim$250 ergs $s^{-1}cm^{-2}sr^{-1}$. The quiet Sun values are approximately constant at $\sim$10 ergs $s^{-1}cm^{-2}sr^{-1}$, except for some deviations resulting from the raster type used in the observation sequence.

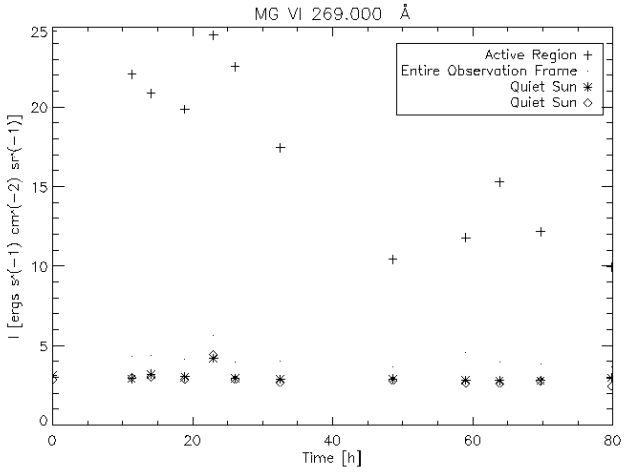

Figure 3.18: NOAA nr. 10976: For the Mg VI 269.000 Å line there are not that many observations, but we clearly see a intensity decrease over time, with some fluctuations, and a constant quiet Sun intensity of ∼3 ergs $s^{-1}cm^{-2}sr^{-1}$.

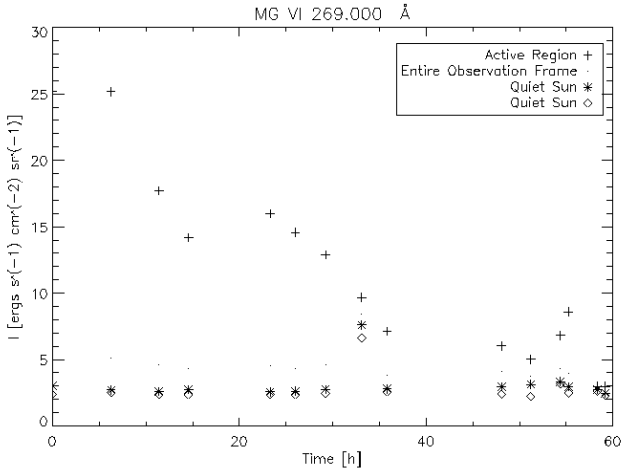

Figure 3.19: NOAA nr. 10977: We clearly see a decrease of active region intensity over time for the Mg VI 269.000 Å line, decreasing from 25 ergs $s^{-1}cm^{-2}sr^{-1}$ to $\sim$ 5 ergs $s^{-1}cm^{-2}sr^{-1}$. While the quiet Sun intensity is constant at ∼3 ergs $s^{-1}cm^{-2}sr^{-1}$.

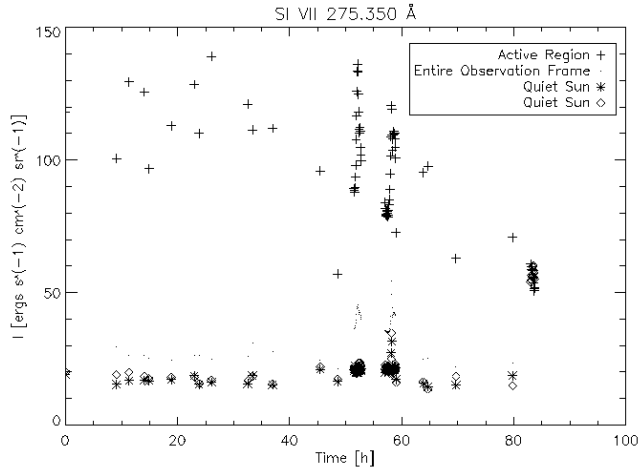

Figure 3.20: NOAA nr. 10976: The mean intensity for Si VII 275.350 Å fluctuate both in the quiet Sun region and in the active region. We observe an average quiet sun intensity of ~ 20 ergs $s^{-1}cm^{-2}sr^{-1}$, with some deviations due to the raster type. In the active region we observe a decrease of intensity over time.

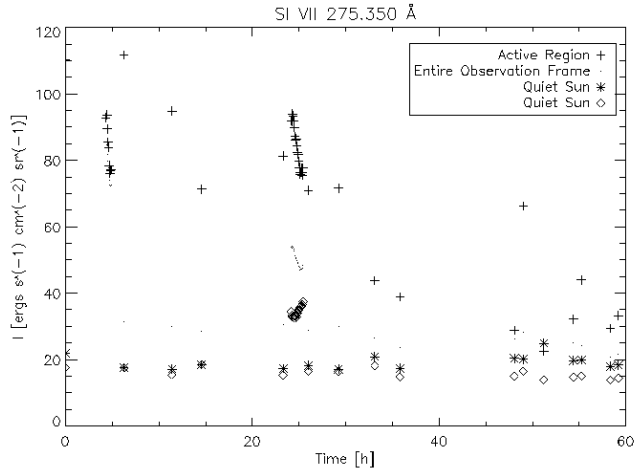

Figure 3.21: NOAA nr. 10977: The Si VII 275.350 Å intensity fluctuate in both quiet Sun and active region, while displaying a decrease in active region intensity and average quiet Sun intensity of ~ 20 ergs $s^{-1}cm^{-2}sr^{-1}$.

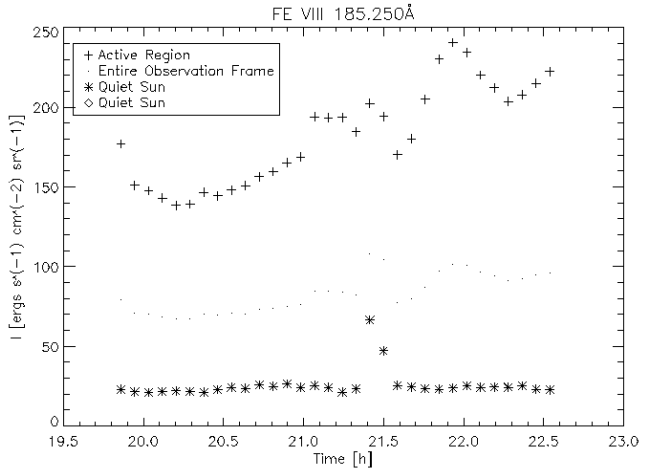

Figure 3.22: NOAA nr. 10976: The mean intensity for Fe VIII 185.250 Å within the active region, quiet Sun and the whole observation frame, as a function of time. Because of a short observational sequence is seems as if the intensity decreases in time for the active region, while the quiet Sun is approximately constant at 30 ergs $s^{-1}cm^{-2}sr^{-1}$.

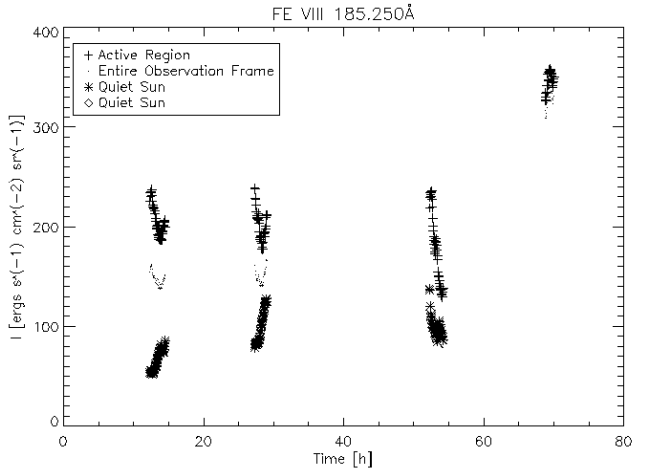

Figure 3.23: NOAA nr. 10977: Three of the observation sequences give the same maximum active region intensity of $\sim$ 240 ergs $s^{-1}cm^{-2}sr^{-1}$. while the active region intensities at 70 h differ from the trend, which is an error introduced by the raster type used. The quiet Sun values for Fe VIII 185.250 Å are varying in intensity, indicating a bad subregion definition.

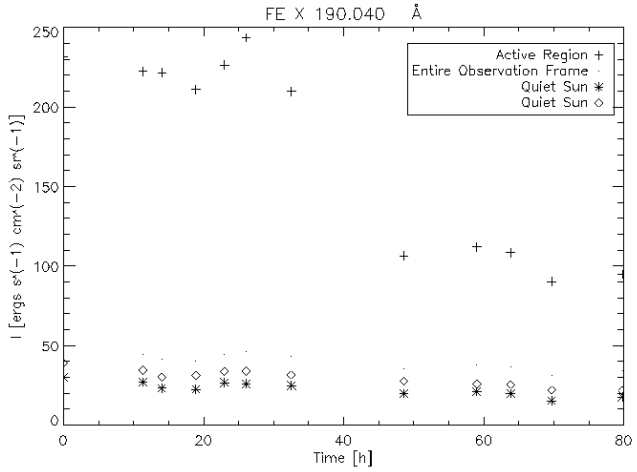

Figure 3.24: NOAA nr. 10976: We observe a decreasing intensity in the active region over time, while the quiet Sun values are approximately constant at ~ 30 ergs $s^{-1}cm^{-2}sr^{-1}$. within the active region, quiet Sun and the whole observation.

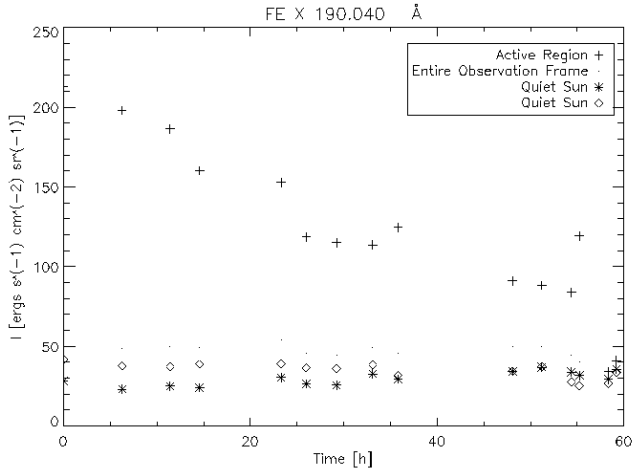

Figure 3.25: NOAA nr. 10977: The quiet Sun intensities for the Fe X 190.040 Å line are constant at $\sim$ 30 ergs $s^{-1}cm^{-2}sr^{-1}$, while the active region intensities are decreasing in time from 200 ergs $s^{-1}cm^{-2}sr^{-1}$ to $\sim$90 within the active region ergs $s^{-1}cm^{-2}sr^{-1}$.

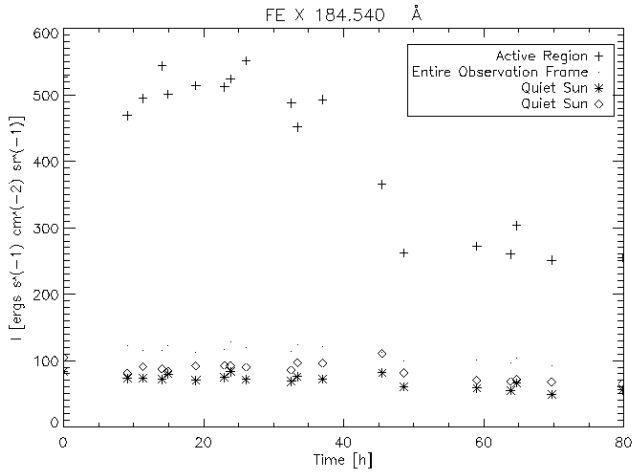

Figure 3.26: NOAA nr. 10976: The intensity for the Fe X 184.540 Å line is twice as strong as the Fe X 190.040 Å line intensity, but with similar intensity structure. Where the quiet Sun values are ∼80 ergs $s^{-1}cm^{-2}sr^{-1}$ and the active region intensity decrease from 550 ergs $s^{-1}cm^{-2}sr^{-1}$ to 250 ergs $s^{-1}cm^{-2}sr^{-1}$ during the observational period.

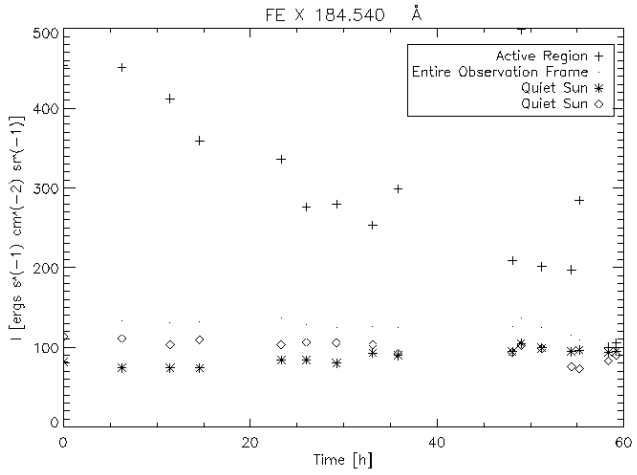

Figure 3.27: NOAA nr. 10977: The intensity for the Fe X 184.540 Å line is twice as strong as the Fe X 190.040 Å line intensity, but with similar intensity structure. Where the quiet Sun values are ∼100 ergs $s^{-1}cm^{-2}sr^{-1}$ and the active region intensity decrease from 450 ergs $s^{-1}cm^{-2}sr^{-1}$ to 200 ergs $s^{-1}cm^{-2}sr^{-1}$during the observational period.

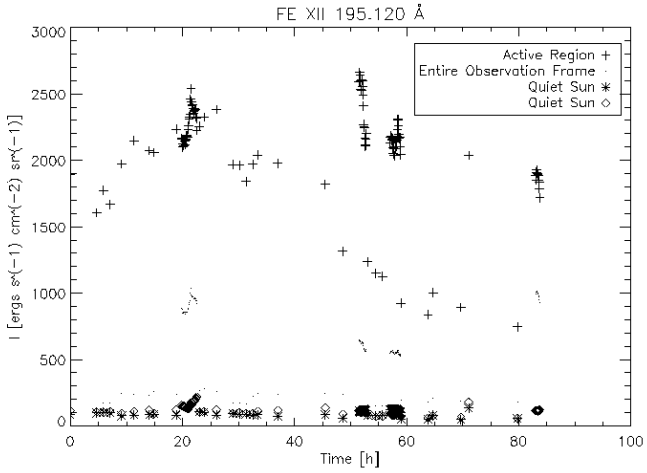

Figure 3.28: NOAA nr. 10976: This is one of the strongest lines observed reaching an active region intensity of ~ 2500 ergs $s^{-1}cm^{-2}sr^{-1}$. The active region intensity decreases in time, falling to 800 ergs $s^{-1}cm^{-2}sr^{-1}$ during the time period, while the quiet Sun intensity stays constant at ~ 100 ergs $s^{-1}cm^{-2}sr^{-1}$.

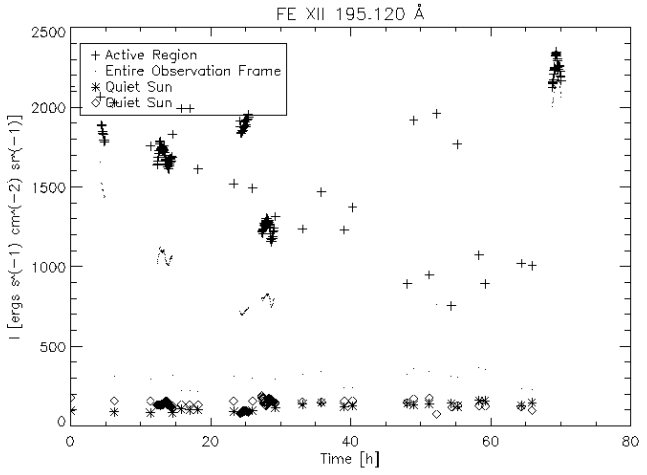

Figure 3.29: NOAA nr. 10977: The active region for the Fe XII 195.120 Å line fluctuates in time, but we observe a clear decrease, changing from 2000 ergs $s^{-1}cm^{-2}sr^{-1}$ to 1000 ergs $s^{-1}cm^{-2}sr^{-1}$ over the time of observation. Notice the deviating observation sequence at 70 h, as mentioned earlier. The quiet Sun intensities are constant at approximately 120 ergs $s^{-1}cm^{-2}sr^{-1}$.

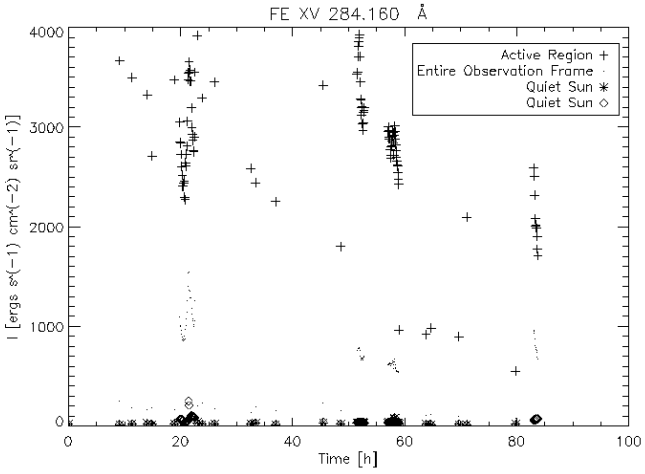

Figure 3.30: NOAA nr. 10976: The intensity structure for the Fe XV 184.160 Å line is similar to the Fe XII 195.120 Å structure, with active region intensities decreasing in time from 4000 ergs $s^{-1}cm^{-2}sr^{-1}$ to 500 ergs $s^{-1}cm^{-2}sr^{-1}$. while the quiet Sun intensities are approximately constant at 100 ergs $s^{-1}cm^{-2}sr^{-1}$.

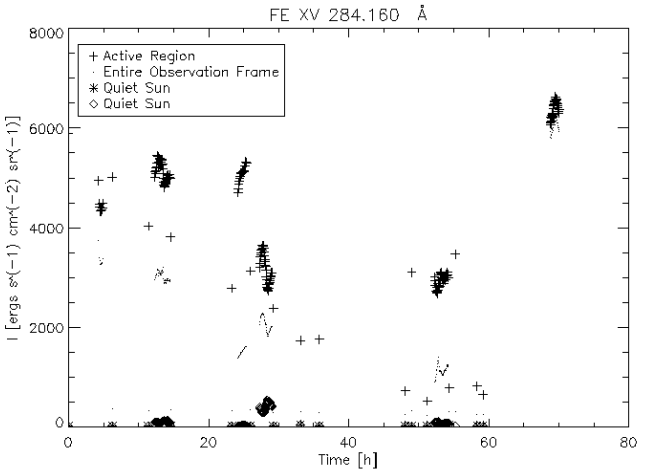

Figure 3.31: NOAA nr. 10977: We observe a intensity decrease from 5000 ergs $s^{-1}cm^{-2}sr^{-1}$ to $\sim$ 500 ergs $s^{-1}cm^{-2}sr^{-1}$ over the active region, when excluding the observation sequence at 70 h. The quiet Sun intensities are approximately constant at 100 ergs $s^{-1}cm^{-2}sr^{-1}$.

Chapter 4

The 3D Numerical Model

An alternate way, complimentary to observations, of studying the solar atmosphere is through numerical modeling.

The Oslo Stagger Code (OSC) is a three dimensional code that has been written to span the entire solar atmosphere from the upper convection zone to the lower corona. This chapter will go through the main ideas of this numerical model, and study the resulting synthetic observations.

4.1 The physical and mathematical problem

The model include non-gray, non-LTE radiative transport in the photosphere as well as magnetic field- aligned heat conduction in the transition region and corona. The basic idea is to solve the MHD equations already introduced in chapter 2:

$$\frac{\partial \rho}{\partial t} + \nabla \cdot (\rho \mathbf{u}) = 0 \tag{4.1}$$

$$\frac{\partial \epsilon}{\partial t} + \nabla(\epsilon \mathbf{u}) + \mathbf{u} \cdot \nabla P = \nabla \mathbf{F_r} + \nabla \mathbf{F_c} + Q_{joule} \tag{4.2}$$

$$\frac{\partial \mathbf{B}}{\partial t} - \nabla \times (\mathbf{u} \times \mathbf{B}) = 0 \tag{4.3}$$

$$\frac{\partial \mathbf{u}}{\partial t} + (\mathbf{u} \cdot \nabla)\mathbf{u} + \frac{1}{\rho}\nabla P = \frac{1}{4\pi\rho}(\nabla \times \mathbf{B}) \times \mathbf{B} - g\hat{z} \tag{4.4}$$

$$P = P(\varepsilon, \rho) \qquad \& \qquad T_g = T_g(\varepsilon, \rho) \tag{4.5}$$

The pressure and the temperature are retrieved from tabulated values given the particular ϵ and ρ , assuming LTE and solar abundances. The rest of the symbols and assumptions are defined in section 2.6.3.

The model involves a coupled system of nonlinear time-dependent PDEs, which have to be solved in a 3D plasma volume.

4.1.1 Radiative Processes in the OSC

Simulations of the lower solar atmosphere have to take into consideration the fact that the atmosphere is optically thick, where radiative transport is an important source and sink of energy in the photosphere and lower chromosphere. In the 3D simulation code used here one obtains this factor by angle and wavelength integration of the transport equation;

$$\frac{\mathrm{d}I_\lambda}{\mathrm{d}z} = j_\lambda - \chi_\lambda I_\lambda \tag{4.6}$$

where j_λ is the emissivity and χ_λ is the opacity, resulting in the radiative flux

$$\nabla \mathbf{F}_r = 4\pi \int_\lambda \varepsilon_\lambda \chi_\lambda (B_\lambda - J_\lambda) d\lambda \tag{4.7}$$

with ε_λ the photon distinction probability, J_λ the mean intensity and B_λ the Planck distribution. Isotropic opacity and emissivity are assumed.

Following Nordlund (1982), the spectrum is divided into four opacity bins based on magnitude. Four transport equations are derived based on these group mean opacities, defining integral intensities and source functions in a consistent manner, assuming opacities in LTE and coherent scattering. The resulting 3D scattering problems are solved using a method developed by Skartlien (2000), which uses iterations based on a one-ray approximation in the angle integral for the mean intensity.

For the upper chromosphere, transition region and corona where the atmosphere is optically thin, effectively thin radiative losses are assumed and the optical depth (τ) scale is chosen so as to confine the important terms involved,

$$\nabla \mathbf{F}_r \approx \rho^2 f(T) \exp(-\tau) \tag{4.8}$$

Additionally an *ad hoc* heating term is added to the energy equation, to prevent cooling below $\sim$ 2000 K in the upper chromosphere.

4.1.2 Coronal heating

Stress in the magnetic field is built up by photospheric and convective buffeting, resulting in growth of the energy density of the field, an energy which eventually must be dissipated. Dissipation can only occur when gradients in the magnetic field become large, because the magnetic diffusivity η is very small. The OSC operates with an η many orders of magnitude larger than that found on the Sun, hence the dissipation starts at smaller magnetic field gradients then those expected on the Sun. The dissipation energy is

$$Q_{Joule} = \eta \mathbf{J} \cdot \mathbf{J} \tag{4.9}$$

where $\mathbf{J} = \nabla \times \mathbf{B}$ is the current density. The dissipation energy and the coronal heating is described in greater detail by Hansteen and Gudiksen (2005).

4.2 The numerical solution

The the solution of the MHD equations is based on an extended version of the numerical code written by Nordlund and Galsgaard (1995). The extensions include the addition of optically thick and thin radiative losses, field aligned conduction and transparent boundary conditions (Hansteen and Gudiksen, 2005).

The model described here consists of a $16 \times 8 \times 16$ Mm^3 box, resolved on a grid of $256 \times 128 \times 160$ points, equidistant in x and y while the vertical grid zones in z increase in size in the corona with increasing height.

The equations are non-dimensionalized ($\bar{u} = u/u_0, \bar{\epsilon} = \epsilon/\epsilon_0$ *etc.*) using

$$\begin{aligned} u_0 &= l_0/t_0 \\ \epsilon_0 &= \rho_0 u_0^2 \\ B_0 &= u_0\sqrt{\mu_0\rho_0} \\ T_0 &= \mu u_0^2/R_0 \\ E_0 &= u_0 B_0 \\ j_0 &= B_0/(\mu_0 l_0) \end{aligned}$$

Where $\mu_0 = 4\pi \times 10^{-7}$V s A^{-1}m^{-1} is the magnetic permeability, $R_0 = 8.3143$ J mol^{-1} K^{-1} is the gas constant, $l_0 = 1$ Mm is the unit of length , $t_0 = 10^2$ s is the unit of time and $\rho_0 = 10^{-7}$ g/cm^3 is the unit of density.

In addition the magnetic permeability is set to $\mu_0 = 1$ and the gas constant is set to $R_0 = \mu$ (mean molecular weight) for the non-dimensionalization.

4.2.1 Discretization

The variables are represented by staggered meshes. The density ρ and the energy ϵ are volume centered, the magnetic field $\mathbf{B}$ and momentum $\rho\mathbf{u}$ are face centered, and electric field $\mathbf{E}$ and the currant density $\mathbf{j}$ are edge centered within a unit cube. A sixth order accurate method involving the three nearest neighbor points on each side is used for determining the partial derivatives, and a fifth order interpolation scheme is used when the variables are needed at positions other then their defined positions. This results in a total of twelve numerical operators, $3 \times 2 \times 2$, representing space, direction and operator types, with the derivative operator $\partial^{\pm}_{,[xyz]}()$ and the interpolation operator $T^{\pm}_{[xyz]}()$.

For example the $\partial_x^+()$ and $T_x^+()$ on the function $f_{i,j,k}$ returns the value shifted $+\frac{1}{2}$ a grid point in the x direction, as follows

$$\begin{aligned} T_x^+(f_{i,j,k}) &= f_{i+\frac{1}{2},j,k} = \\ & a(f_{i,j,k}+f_{i+1,j,k})+b(f_{i-1,j,k}+f_{i+2,j,k})+c(f_{i-2,j,k}+f_{i+3,j,k}) \end{aligned} \tag{4.10}$$

$$\begin{aligned} \partial_{,x}^+(f_{i,j,k}) &= f'_{i+\frac{1}{2},j,k} = \\ & \frac{c_1}{\Delta x}(f_{i,j,k}-f_{i+1,j,k})+\frac{c_2}{\Delta x}(f_{i-1,j,k}-f_{i+2,j,k})+\frac{c_3}{\Delta x}(f_{i-2,j,k}+f_{i+3,j,k}) \end{aligned} \tag{4.11}$$

where $a=\frac{1}{2}-b-c$, $b=-\frac{1}{16}-3c$, $c=\frac{3}{256}$, $c_1=1-3c_2-5c_3$, $c_2=-\frac{1}{24}-5c_3$ and $c_3=\frac{3}{640}$.

4.2.2 Time stepping

The courant conditions for the MHD equations scale as $\Delta t<\frac{\Delta z}{v}$ where v represent the various phase speeds of the system, e.g. sound, alfven or flow speeds. On the other hand the courant condition for thermal conduction scales as the grid size squared Δz^2, since conduction is a second order operator. This relation makes direct explicit solution of the equations very costly as the spatial resolution increases and Δz^2 becomes small. In the OSC one proceeds by operator spitting the energy equation: Given the operator L such that $L\mathbf{u}=\mathbf{f}$ where $\mathbf{u}$ is the array of independent variables and $\mathbf{f}$ the error, one write $L=L_{mhd}+L_{conduction}$ and solve these operators independently.

In treating the mhd operator the explicit 3rd order predictor-corrector procedure by Hyman (1976) is used, only here modified for the variable time steps. The method proceeds by extrapolating a polynomial fit to the time derivative from the previous time steps (n-1,n) to the new time step (n+1) (the predictor step), then using this result to interpolate the derivative (the corrector step).

The predictor is

$$f_{n+1}^{(*)}=a_1f_{n-1}+(1-a_1)f_n+b_1\dot{f}_n, \tag{4.12}$$

and the corrector

$$f_{n+1}=a_2f_{n-1}+(1-a_2)f_n+b_2\dot{f}_n+c_2\dot{f}_{n+1}^{(*)}, \tag{4.13}$$

where

$$\begin{aligned} a_1 &= r^2, \\ b_1 &= \Delta t_{n+1/2}(1+r), \\ a_2 &= 2(1+r)/(2+3r), \\ b_2 &= \Delta t_{n+1/2}(1+r^2)/(2+3r), \\ c_2 &= \Delta t_{n+1/2}(1+r)/(2+3r), \\ r &= \Delta t_{n+1/2}/\Delta t_{n-1/2}, \end{aligned}$$

The Hyman method has a fourth order truncation error in Δt.

Operator splitting leads to the following energy equation for the conduction

$$\frac{\partial e}{\partial t} = -\nabla(\kappa_{||}\nabla_{||}T), \tag{4.14}$$

where $\kappa_{||}$ is the heat conduction coefficient, defined as $\kappa_{||} = \kappa_0 T^{5/2}$, and the parallel signs represent the fact that the heat conduction is aligned with the magnetic field lines. This operator is solved by the Crank-Nicholsen method, which is an implicit scheme in time, using an average of the previous time step n and the next $n+1$, of some variable u. This gives the next time step $n+1$ when solving the operator equation $L_{conduction}$ $\mathbf{u}$= $\mathbf{f}$ as follows;

$$u_{n+\frac{1}{2}} = \frac{1}{2}(u_n + u_{n+1}) \tag{4.15}$$

$$f_{n+1} = \mathrm{L}_{conduction}(u_{n+\frac{1}{2}}) \tag{4.16}$$

The solution of equation 4.16 results in a residual equation, which has some small scale and some large scale errors, because $L_{conduction}$ is an elliptic like operator. The small scale errors can be smoothed out by iterative processes such as Gauss-Seidel. But Gauss-Seidel is ineffective on large scales, thus to smooth out the large scale errors we proceed by multigrid methods, in which we introduce a operator L_H on a coarser grid as an approximation to $L_{conduction}$. This makes the large scale errors from the *fine* grid smaller, making it possible to smooth them out iteratively.

For this procedure to work one needs to use a so called *fine-to-coarse* operator, which interpolates and defines the problem on the coarse grid. In addition an interpolation operator (*coarse-to-fine operator*) is used to return to the fine grid.

One such "coarsification" results in a two grid method. Repeating this process by making the new operator coarser for the solution of the residual

equation, regridding the problem on successively coarser scales, thus converting large scales to small scales, results in the multigrid method. (More on the multigrid method can be found in chapter 19 of *Numerical Recipes* by Press et al. (1992)).

4.2.3 Running the code

The models used in this work stretch from some 1.5 Mm below the photosphere to 14 Mm above.

An average temperature structure and an average density structure of the synthetic solar atmosphere are plotted in figure 4.2.3, where the solid line represents the temperature and the dotted line represents the density, displaying the evolution in the z direction. These temperature and density changes along z give us information of the synthetic atmosphere.

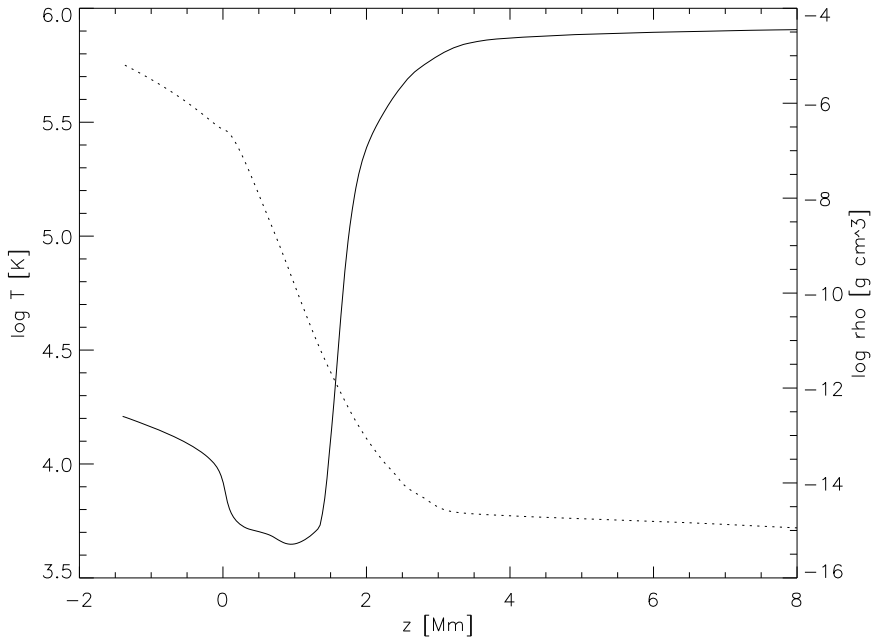

Figure 4.1: The average temperature(–) and the average density($\cdots$) along the z direction.

The convection zone is represented by the area beneath $z = 0$, starting at ∼-1.5 Mm, where the average temperature is $\log T \approx 4.2$ and the average density is $\log \rho = -5$. As z increases, we observe a constant fall in temperature and density over a 1.5 Mm interval.

The photosphere is evident in the plot by the steep drop in temperature and density at $z = 0$. The drop in temperature is a result of the synthetic

atmosphere becoming optically thin, allowing photons to travel unimpeded through space.

The photosphere is a short area in space, stretching over the area of the step temperature decrease of approximately 200 km along z. From this

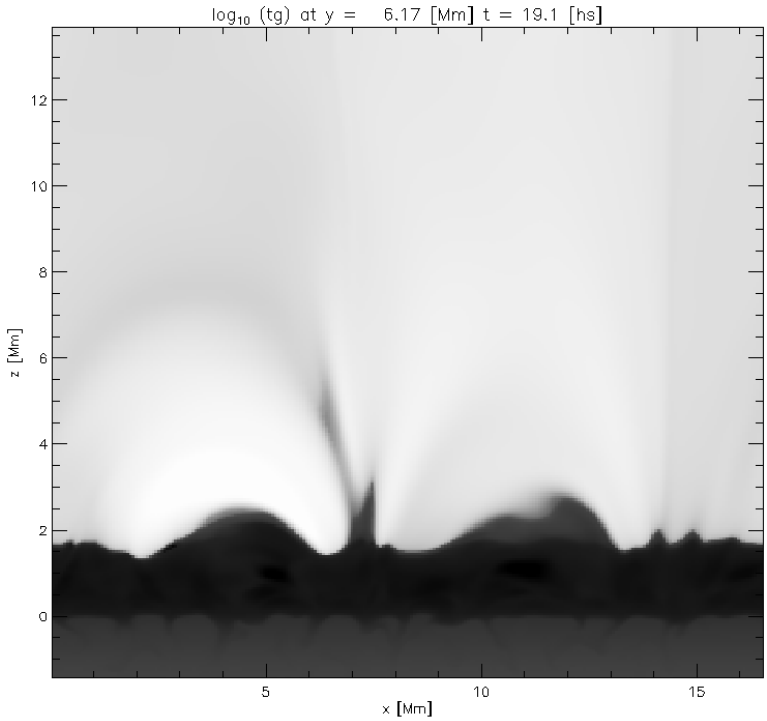

Figure 4.2: The temperature variation according to the z and x direction. The color scale represent the temperature, going from low to high with the color representation black to white, respectively.

point in the upper photosphere, the chromosphere stretches out some 2 Mm to the bottom of the transition region, where the temperature rises rapidly to coronal values of some 10^6 K over a few thousand kilometers. Both the chromosphere and corona are heated by a combination of magnetic dissipation and acoustic (and magnetosonic) waves. Chromospheric densities are sufficiently high such that this heating is radiated away and temperatures remain roughly constant, while coronal densities and thus radiative cooling rates are much lower, and the (primarily magnetic) heating causes high temperatures.

As the magnetic energy stored in the twisted field lines is dissipated, the temperature increases over 2 orders of magnitude within a region a few thousand kilometers, known as the the transition region.

The corona show itself as the area where the temperature rise decreases

and eventually becomes approximately constant, with a temperature of $\sim 10^6$ K and density of $\sim 10^{-15}$g cm^{-3}. This is because of the scale height, which is given by

$$H = \frac{k_B T}{\mu m_H g} \tag{4.17}$$

where $k_b = 1.380658 \cdot 10^{-16}$ erg K^{-1} is Boltzmann's constant, μ the mean moleculare weight and $g = 2.75 \cdot 10^5$ cm/s^2 the gravitational acceleration on the solar surface.

Equation 4.17 show that the scale height increase with temperature. We therefore observe a approximately constant density in the corona because the scale height is so large at corona temperatures.

We can also look at the temperature structure as a function of both the z and x direction, giving us a better view of the photosphere, chromosphere and corona variations. This is displayed in figure 4.2, where the temperature increases with the color scale dark to light.

The photosphere is represented in the boundary between the black area and the grey area at approximately $z = 0$.

The chromosphere is the area of lowest temperature in the atmosphere and therefore represented by the black area on the figure. This is where we observe high activity, varying in size from 1 Mm to 2.5 Mm.

We find evidence of cool gas even at grate heights such as observed in figure 4.3 at $x \approx 7$ Mm. Here we observe an area of low temperature stretching out to 6 Mm along the z direction, where we also see a looplike structure of low temperature bending toward more negative x values. We observe low temperature loop structure bending toward more positive x values as well. This low temperature structure has footprints at $\sim$7 Mm and $\sim$14 Mm in the chromosphere, stretching up to 5 Mm in the corona, which is represented by the high temperature in this figure, extended from $\sim$2 Mm all the way out of the simulation domain along the z direction.

The simulation is initialized by a random set of magnetic poles of opposite polarity at the bottom of the simulation box, where the poles have a strength of $\pm$1500 Mx/cm^2. A unsigned magnetic flux of $\sim$ 100 Mx/cm^2 is injected along the y direction. Field lines are formed between the poles of opposite polarity as the flux is injected, as displayed in figure 4.3.

We observe that the magnetic poles of different polarity eventually align, forming dark and light regions through the convective structure, as shown in figure 4.3. We see that three areas align along the y direction, of presumably positive, negative and again positive polarity. These areas stretch out from 1 Mm to 3 Mm, 6 Mm to 9 Mm, and 13 Mm to 15 Mm in x, respectively. This structure is also evident in figure 4.2, where gas of low temperature forms loop structures with base in the chromosphere at these similar x values.

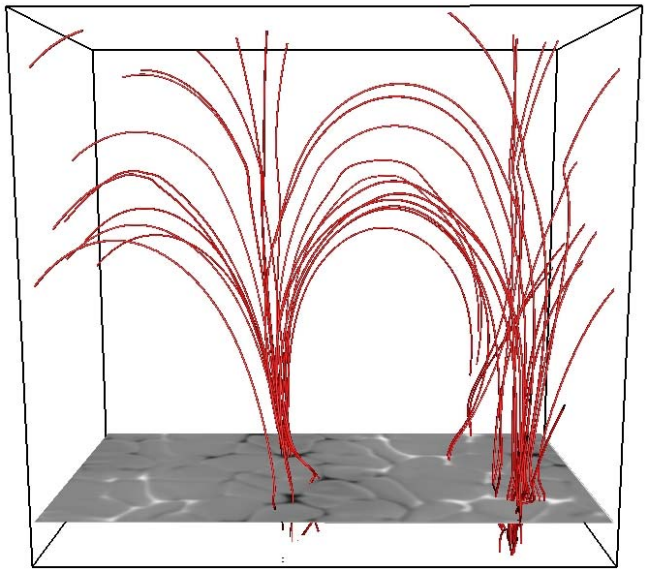

Figure 4.3: The magnetic field displayed in grey as viewed in the photosphere. The red loops are magnetic filed lines emerging between the two magnetic poles, which extend through the entire corona.

Hot material is transported to the surface ($z = 0$) by convection, where cool material falls back downward, toward more negative z values getting warmer as z decreases as we see in figure 4.2.3. Because the magnetic poles are fixed beneath the convection zone (see figure 4.3),we observe convective activity moving and twisting the magnetic field lines which have reached the photosphere.

This persistent moving and twisting of the field, increases the magnetic stress in the field lines to the point of dissipation, which is the cause of the high temperature in the corona.

4.3 Calculating the synthetic intensity

From the initial state described above, the 3D code is run for a certain amount of time. The state of the atmosphere is saved every 10 s. At each grid point the density ρ and the temperature T_g are retrieved, giving us the possibility to calculate the intensity of of this particular state.

int3d3 is a numerical integration routine made to study the intensity emerging from the three dimensional simulations of the upper solar atmosphere.

The routine uses the data objects to provide the density and temperature of a specific time step of the simulation as input values, as well as a list of the ions we wish to work with.

The CHIANTI (Landi et al., 2006) atomic database provides us with the necessary atomic data as well as spectroscopic analysis routines, which are integrated in the *ind3d3* routine.

4.3.1 Calculating the intensity

The intensity emerging from the synthetic spectra of the 3D simulation is obtained by integration along the z direction, where the line of sight is set to be parallel to the z axis, following equation 2.59;

$$\mathrm{I}_\nu = Ab_x \int_0^z n_e^2 C(T, \nu, n_e)\mathrm{d}z. \tag{4.18}$$

For the lines of interest temperatures are high enough such that we can assume that all H is ionized, we can assume LTE conditions when finding the densities $n_e(\rho, T)$ through ρ and T values from the simulations. The abundances Ab_x are obtained by Grevesse et al. (1996), where we use an abundance file provided by CHIANTI (sun_photospheric.abund).

The contribution function $C(T, \nu, n_e)$ is provided by the CHIANTI routine *g_of_t*, which is designed for this purpose. This routine calculates the contribution function for a specific ion over a logarithmic temperature rage from 4 to 8 in 0.1 dex intervals, for selected emission lines. The form of the function is;

$$C(T, \nu, n_e) = \Delta E \cdot 0.83 \cdot \frac{n_u}{n_e} \cdot A_{ul} \cdot F(T_e) \tag{4.19}$$

Where $\Delta E = h\nu/4\pi$ is the energy, A_{ul} the Einstein coefficient, n_u the density of the upper energy state of the ion, n_e the electron density, 0.83 the hydrogen to electron ratio and $F(T_e)$ is a function strongly dependent on the electron temperature. This function also takes the atomic number and spectroscopic number of the ion as input values.

We interpolate to the temperature values of the model, since $C(T)$ is tabulated on a course temperature grid, using the routine *ion_interp*, also provided by CHIANTI.

The new $C(T, \nu, n_e)$ is then used to calculate the intensity (equation 4.18). The trapezoidal method of numerical integration is used to integrate along the z direction at each point in the x and y plane, resulting in a intensity map from the snapshot produced by the OSC simulation code.

The *ind3d3* routine also utilizes the *intdisplay* widget function to define subregions in the intensity maps, and continues as in the *comp_int* routine, with some modifications, to make line data files. The line data files containes the time step, the line id, mean intensity in the sub region, maximum intensity, minimum intensity and a comment about the region marked in intensity map.

4.4 Results

The ions we are interested in are tabulated in table 4.1 where the observed lines are identified with theoretical lines by CHIANTI. There are some spectral lines which are worth noticing; the Mg VI lines and the He II lines. From the observations we have two Mg VI spectral lines with the respective wavelengths 269.00 Å and 269.8 Å. The CHIANTI database identifies these lines with the theoretical lines of Mg VI with wavelengths 268.9912 Å and 270.3906 Å. We assume that the observed 269.00 Å line is a representative of the 268.9912 Å line and that the observed 269.8 Å line is represented by the theoretical line of 270.3906 Å. We assume that the He II line observed is a blend of the two theoretical He II lines, 256.3170 Å and 256.3180 Å, respectively, where the 257.3170 Å line is two times stronger in intensity than the 256.3180 Å line. We therefore use the contribution from both these lines when calculating the synthetic intensities of He II 256.320 Å.

The other lines are easily identified by CHIANTI.

Ion	λ_{obs} (Å)	λ (Å)	Transition	T_{max}
Fe X	184.540	184.5370	$3s^2\ 3p^5\ {}^2P_{3/2}$ - $3s^2\ 3p^4\ ({}^1D)\ 3d\ {}^2S_{1/2}$	6.0
Fe VIII	185.120	185.2130	$3p^6\ 3d\ {}^2D_{5/2}$ - $3p^5\ 3d^2\ ({}^3F)\ {}^2F_{7/2}$	5.9
Fe X	190.040	190.0370	$3s^2\ 3p^5\ {}^2P_{1/2}$ - $3s^2\ 3p^4\ ({}^1D)\ 3d\ {}^2S_{1/2}$	6.0
Fe XII	195.120	195.1190	$3s^2\ 3p^3\ {}^4S_{3/2}$ - $3s^2\ 3p^2\ ({}^3P)\ 3d\ {}^4P_{5/2}$	6.2
He II	256.320	256.3170	$1s\ {}^2S_{1/2}$ - $3p\ {}^2P_{3/2}$	4.9
		256.3180	$1s\ {}^2S_{1/2}$ - $3p\ {}^2P_{1/2}$	4.9
Mg VI	269.000	268.9912	$2s^2\ 2p^3\ {}^2D_{3/2}$ - $2s\ 2p^4\ {}^2P_{1/2}$	5.7
Mg VI	269.800	270.3906	$2s^2\ 2p^3\ {}^2D_{5/2}$ - $2s\ 2p^4\ {}^2P_{3/2}$	5.7
Si VII	275.350	275.3536	$2s^2\ 2p^4\ {}^3P_2$ - $2s\ 2p^5\ {}^3P_2$	5.8
Fe XV	284.160	284.1630	$3s^2\ {}^1S_0$ - $3s\ 3p\ {}^1P_1$	6.3

Table 4.1: Theoretical lines given by CHIANTI, the maximum temperature is displayed in logarithmic values.

We use a 740 s long period from the simulation, starting at simulated time 1370 s with a 10 s interval between each state. Intensity maps from the first snapshot are displayed in figure 4.4.

The color scale of the intensity map is one that displays the highest

intensity as white, in such a way that the color darkens as the intensity declines. We have chosen to display the intensity maps of He II 256.320 Å, Si VII 275.350 Å and Fe XII 195.120 Å because these lines represent a large temperature range, as table 4.1 shows. Gas trapped by the magnetic field can be seen in the intensity maps as intensity structures which follow the magnetic field lines, as displayed in figure 4.3 and discussed in section 4.2.3. The He II 256.320 Å line, which is formed at $\log T = 4.9$ K, displays many intensity structures. The magnetic poles are observed as two lines with approximately constant intensity and constant position along x, at $\sim$7 Mm and $\sim$15 Mm. As we go higher up in the atmosphere we observe that the structures fade, and the areas where the magnetic poles lie gets clearer as the gas get trapped by the magnetic field lines, as observed in the intensity maps of the Fe XII 195.120 Å line in figure 4.4 and 4.5. When reaching temperatures of $\log T = 6.2$ K, where the Fe XII 195.120 Å line is formed, we clearly see footprints of the magnetic loops. These are also displayed in figure 4.3, where the highest intensity is emitted furthest away from the magnetic poles along the x direction.

We define regions of 'quiet Sun' and 'active region' with the intensity map. As we observe on the intensity maps in figure 4.4 and 4.5 there are no areas standing out as an active region or quiet Sun in the same way as we observed with EIS in chapter three, *i.e.* no semi-isotropic quiet Sun with a welldefined active region. The whole intensity maps of the synthetic spectra are in a way an active region, because of the underlying magnetic poles. Even though this is the case, we still have to define a quiet Sun region and an active region within the synthetic intensity map. We choose to define the area of highest intensity within the intensity map as the active region, marked with (1) in the intensity map. The region of lowest intensity is defined as quiet Sun, marked with (2) in the intensity map. As mentioned in section 4.2.3, the unsigned magnetic flux within the simulation domain is high (100 Mx/cm^2), typically of a weak plague region on the Sun, which might lead to high quiet Sun intensities.

Following the definitions of the subregions, mean values of the intensity in these areas are calculated, and plotted over time in figure 4.4 to 4.4, where (+), ($*$) and ($\diamond$) represent the active region, entire observation frame and quiet Sun, respectively. These plots show similar characteristics as the observation data presented in figure 3.14 to 3.31 for NOAA 10976 and NOAA 10977, where the active region intensity is much higher than the intensity of the quiet Sun. The intensities from the active regions also show high variations in intensity while the intensity in the quiet Sun is relatively constant, similar to the observations made with EIS. A discussion of the synthetic intensity structure for the lines of interest follows.

He II 256.320 Å

The He II 256.320 Å line (top frame in figure 4.4) gives approximately

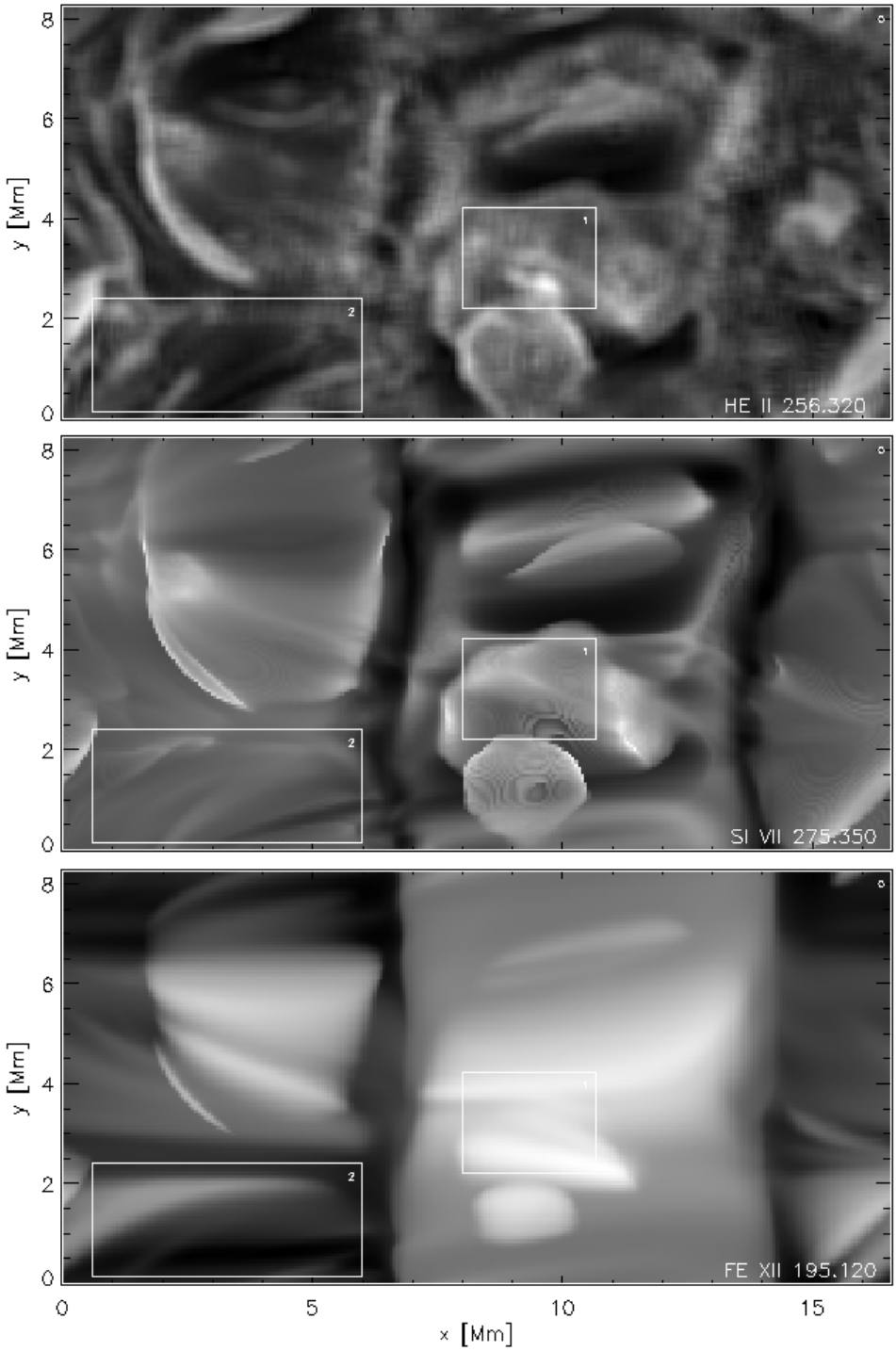

Figure 4.4: Intensity maps for He II 256.320 Å, Si VII 275.350 Å and Fe XII 195.120 Å at 13.5 hs with the interesting subregions defined; 0: Entire Observation Frame, 1: Active Region and 2: Quiet Sun, for time $13.7 \cdot 10^2$s

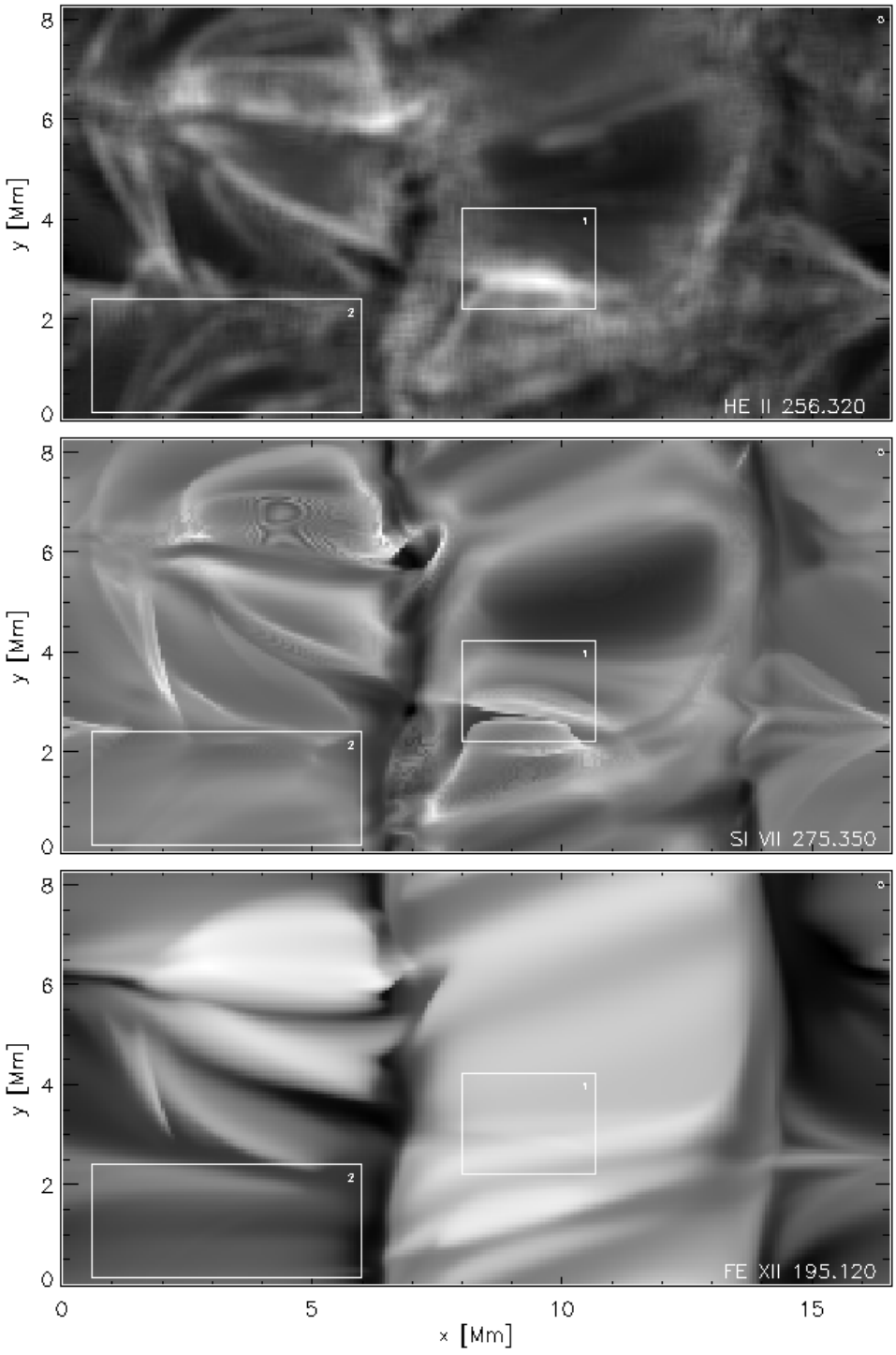

Figure 4.5: Intensity maps for He II 256.320 Å, Si VII 275.350 Å and Fe XII 195.120 Å at 19.1 hs with the interesting subregions defined; 0: Entire Observation Frame, 1: Active Region and 2: Quiet Sun.

constant quiet Sun values over time, with an average value of 200 ergs $s^{-1}cm^{-2}sr^{-1}$. For the active region we observe an intensity increase towards a maximum value of 1927 ergs $s^{-1}cm^{-2}sr^{-1}$ at 1910 s, followed by an intensity decrease for the remaining time. We observe a small increase of intensity with time for the entire simulation domain as well.

Mg VI 269.000 Å

This is a relatively week line emerging from the simulation as we see in the middle frame in figure 4.4, with approximately constant quiet Sun values at $\sim$40 ergs $s^{-1}cm^{-2}sr^{-1}$. The active region intensity is quite dynamic, but with an intensity peak following the He II 256.320 Å line, at 1930 s, with a value of 112 ergs $s^{-1}cm^{-2}sr^{-1}$. The total intensity emerging from the simulation domain remains constant in time.

Mg VI 269.800 Å

The Mg VI 269.800 Å intensity structure is similar to the Mg VI 269.000 Å line structure for this simulation, as shown in the bottom frame in figure 4.4. The Mg VI 269.800 Å intensity is $\sim$ 2 times larger than the Mg VI 269.000 Å intensity, both in quiet Sun and active region. Quiet Sun values are at approximately 70 ergs $s^{-1}cm^{-2}sr^{-1}$. The active region has an average intensity of 130 ergs $s^{-1}cm^{-2}sr^{-1}$, with an intensity peak at 1930 s, reaching the value of 193 ergs $s^{-1}cm^{-2}sr^{-1}$.

Si VII 275.350 Å

The simulations give quiet Sun values which are increasing in time , starting at $\sim$ 20 ergs $s^{-1}cm^{-2}sr^{-1}$, and ending at $\sim$ 360 ergs $s^{-1}cm^{-2}sr^{-1}$ - values which are much higher than the EIS observation results. We observe similar intensity structure for the active region as for the Mg VI lines discussed above (see the top frame in figure 4.4), where we have a peak intensity at 1930 s, with the intensity value of 541 ergs $s^{-1}cm^{-2}sr^{-1}$.

Fe VIII 185.250/185.210 Å

This is the strongest line emerging from the simulation, with an average quiet Sun value of 1100 ergs $s^{-1}cm^{-2}sr^{-1}$ and active region value of $\sim$ 2000 ergs $s^{-1}cm^{-2}sr^{-1}$, as displayed in the middle frame on figure 4.4. There are quite large variations in the active region intensities; between 1500 and 2500 ergs $s^{-1}cm^{-2}sr^{-1}$, as we also observe with EIS, where the variations are from 150 to 250 ergs $s^{-1}cm^{-2}sr^{-1}$. The simulation values are approximately 10 times larger then the intensity values from the EIS observations. We also observe that the intensity structure for the active region is similar to the previous lines discussed, but with the peak value at 1940 s with intensity 2369 ergs $s^{-1}cm^{-2}sr^{-1}$. That the peak comes at a later time is a result of the fact that this line is formed at higher temperatures($\log T = 5.9$) K.

The intensity of the entire simulation domain increase with time, follow-

ing the curve of the quiet Sun intensity.

Fe X 184.540 Å
The intensity structure changes for this spectral line, compared to the previously discussed structures, as we can observe in the bottom frame of figure 4.4. The results from the simulation show a small increase in quiet Sun intensities over time, with an average intensity of 120 ergs $s^{-1}cm^{-2}sr^{-1}$, as well as for the active region which increase with small fluctuations, having a mean intensity of ∼900 ergs $s^{-1}cm^{-2}sr^{-1}$. For this spectral line we clearly see that the intensity of the entire observational domain increase with time. This may be a result of the increased intensity of the active region, but it may also be an indication that the simulation have not reached a stable situation for the temperature of $\log T = 6.0$ K.

Fe X 190.040 Å
We observe the same intensity structure for the Fe X 190.040 Å line as we did for the Fe X 184.540 Å line, which both are lines formed at $\log T = 6.0$ K. However, the Fe X 190.040 Å intensity is 4 times weaker than the Fe X 184.540 Å. The quiet Sun intensity has a small increase over time, with a mean intensity of only ∼35 ergs $s^{-1}cm^{-2}sr^{-1}$, and an active region mean intensity of ∼260 ergs $s^{-1}cm^{-2}sr^{-1}$, with a maximum value of 390 ergs $s^{-1}cm^{-2}sr^{-1}$ at 2040 s.

Fe XII 195.120 Å
We observe an approximately constant quiet Sun intensity over time. The active region values are a factor of approximately 2 smaller than that of the EIS observations, with mean intensity of ∼ 730 ergs $s^{-1}cm^{-2}sr^{-1}$. The main reason for this seems to be that the simulation values have not stabilized as a function of time, as the previous intensity plots show, where the mean intensity of the entire observational frame increases over time. If we compare the maximum intensity values reached at the end of our simulation, we observe that they are reaching the same size as the intensities from the EIS observations.

Fe XV 284.160 Å
The quiet sun intensities for the Fe XV 284.160 Å are approximately zero for this line. We observe similar intensity structures for the Fe XV 284.160 Å line in the active region as for the Fe XII 195.120 Å line, but with intensity values which are 32 times smaller. These are the lowest intensity values of all the lines studied, suggesting that the simulation does not reach the high temperatures of $\log T$=6.3 K, which are necessary for the formation of the Fe XV 284.160 Å line. The plot of the mean intensity in figure 4.4 shows an increase of intensity for the entire observational frame after some time, where we observe that the intensity of the entire frame eventually exceeds the

intensity of the active region, indicating that we have chosen a bad definition of active region within the intensity map. This might also indicate that the simulation need some more time to stabilize, implying that we might have gotten results of similar nature as the EIS observations if the simulation were run for a longer time period.

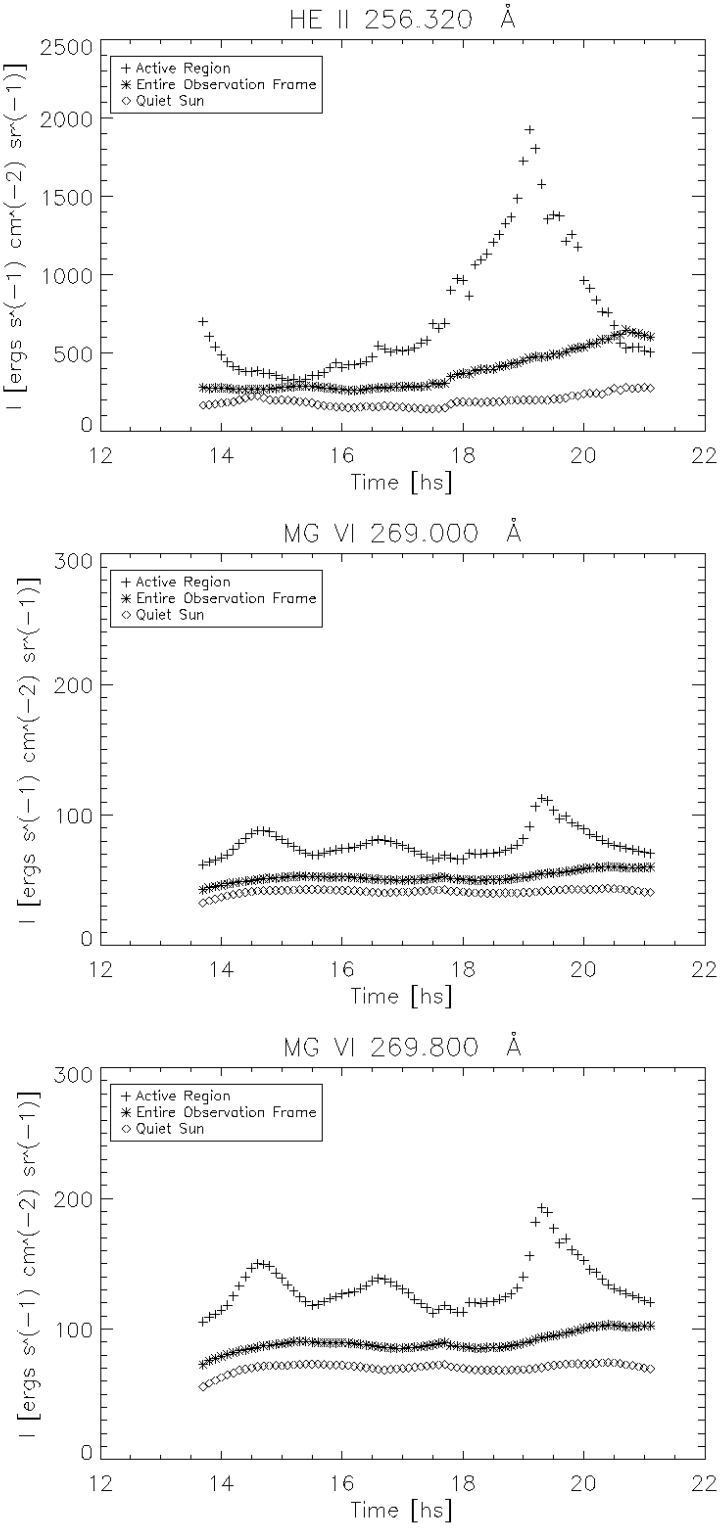

Figure 4.6: Synthetic spectra intensities for He II 256.320 Å, Mg VI 269.000 Å and Mg VI 269.800 Å lines. (+), (∗) and (◇) represent the active region, entire observation frame and quiet Sun, respectively.

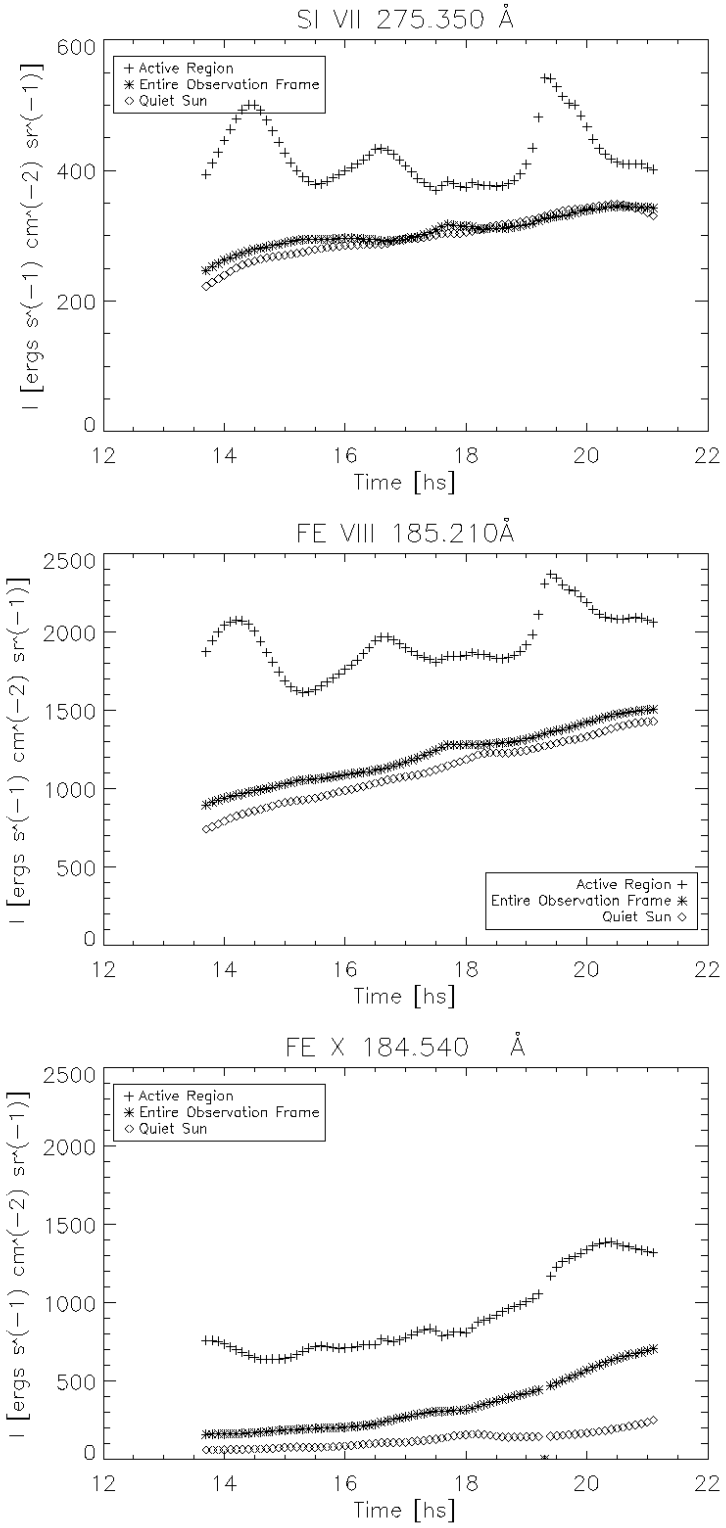

Figure 4.7: Synthetic spectra intensities for Si VII 275.350 Å, Fe VIII 185.210 Å and Fe X 184.540 Å lines. (+), (∗) and (⋄) represent the active region, entire observation frame and quiet Sun, respectively.

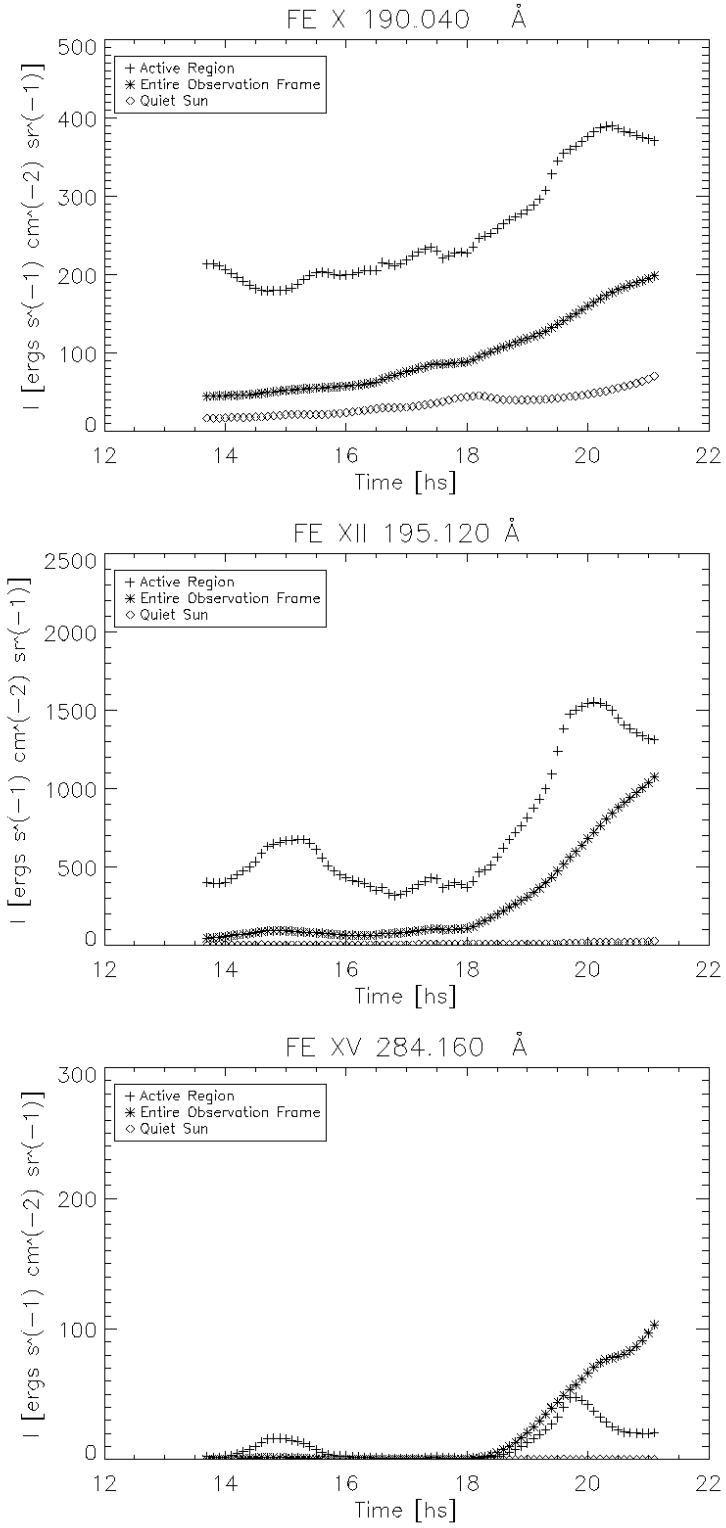

Figure 4.8: Synthetic spectra intensities for Fe X 190.040 Å, Fe XII 195.120 Å and Fe XV 284.160 Å lines. (+), (∗) and ⋄() represent the active region, entire observation frame and quiet Sun, respectively.

Chapter 5

EIS versus OSC

In chapter 3 we splited the average intensity observations into quiet Sun and active region bins based on the morphology of the Fe XII 195 line. The areas defined where then used for all the other lines observed, both those formed in the transition region and those formed in the corona. This procedure was shown to be difficult as the region associated with enhanced active region emission differs from line to line. The same goes for regions that seem very quiet in *e.g.* He II 256 can be somewhat more active in upper transition region and coronal lines. Nevertheless, we feel that the choices made still give a reasonable representation of the span of active region and quiet Sun intensities.

The simulated data obtained through the OSC also presents difficulties in defining 'active region' and 'quiet Sun' intensities. The region modelled is fairly small, only 16×8 Mm, and thus does not really contain good examples of either purely active nor purely quiet Sun regions. We have attempted to compensate for this by choosing one small bright region in Fe XII 195 as an example of active Sun and a small dark region in the same line to represent quiet Sun.

This chapter will be used to compare the results from the real observations using EIS and the synthetic intensities from the simulations using the OSC. With the difficulties mentioned above in mind it should not be surprising if the observed and simulated intensities differ. On the other hand, a comparison and analysis of the relative intensities should give some indication of whether or not the model presented in chapter 4 can reproduce the behavior of the Sun, and in particular the connections between convection zone, photospheric motions, magnetic fields and transition region and coronal emission, with any fidelity.

5.1 Intensity comparison

In order to compare the synthetic intensities and the real intensities we include the standard deviation in the comparison. As seen from both the EIS observations and the OSC results there are large variations in intensity. We choose to plot the mean intensity from the simulation from 18.9 hs to 20.7 hs, with the standard deviation of this particular region as function of the temperature. For the comparison we include the mean intensity of a 20 hour period from the EIS observations. Intensity value are selected from t=10 h, as displayed in figure 3.14 to figure 3.31, for both NOAA 10976 and NOAA 10977, with the standard deviation in intensity from this time period. The results for quiet Sun values are presented in figure 5.1 and the active region results in figure 5.3.

5.1.1 Quiet Sun

From figure 5.1 we observe that the He II 256.320 Å line is approximately the same in intensity for the OSC simulation and for the EIS observations of NOAA 10976 and NOAA 10977, with a value of $\log\langle I\rangle \approx 2.3$ ergs $s^{-1}cm^{-2}sr^{-1}$. This shows that the OSC may be a good representation for the solar atmosphere in the lower transition region.

The intensities for the Mg VI 269.800 Å and the Mg VI 269.000 Å lines from the OSC are quite similar in magnitude, with values of $\log\langle I\rangle \approx 1.85$ ergs $s^{-1}cm^{-2}sr^{-1}$ and $\log\langle I\rangle \approx 1.7$ ergs $s^{-1}cm^{-2}sr^{-1}$. In the observation of NOAA 10976 and NOAA 10977 we see a difference of $\log\langle I\rangle \approx 1.1$ ergs $s^{-1}cm^{-2}sr^{-1}$ in intensity between these lines, where the standard deviation for the respective spectral lines are large. We observe that the Mg VI 269.800 Å line, with a value of $\log\langle I\rangle \approx 1.4$ ergs $s^{-1}cm^{-2}sr^{-1}$, is much stronger for NOAA 10977 then for NOAA 10976. The EIS intensity is here $\log\langle I\rangle \approx 1$ ergs $s^{-1}cm^{-2}sr^{-1}$, which is almost as strong as the synthetic intensity of Mg VI 269.800 Å line. CHIANTI predicts that the Mg VI 269.800 Å line should be 1.7 times larger than the Mg VI 269.000 Å line, which is approximately what we get from the simulations. This is not the case for the observations, where the difference is $\sim$3 for NOAA 10976 and $\sim$ 13 for NOAA 10977.

Analyses of CHIANTI spectra show that the observed Mg VI 269.800 Å line is a blend of the corona line Fe XIV 270.520 Å ($\log T = 6.2$) line and the Mg VI 270.3906 Å ($\log T = 5.7$) line, as presented in figure 5.1.1. For the simulations CHIANTI identified the Mg VI 269.000 Å line with the theoretical line Mg VI 270.3906 Å.

This may be a reason for the big intensity difference between the simulation and the observations. The intensity from the simulations is from the intended line (Mg VI 270.3906 Å) while the observed intensity is of the blend of the Mg VI 270.3906 Å line and the Fe XIV 270.520 Å line.

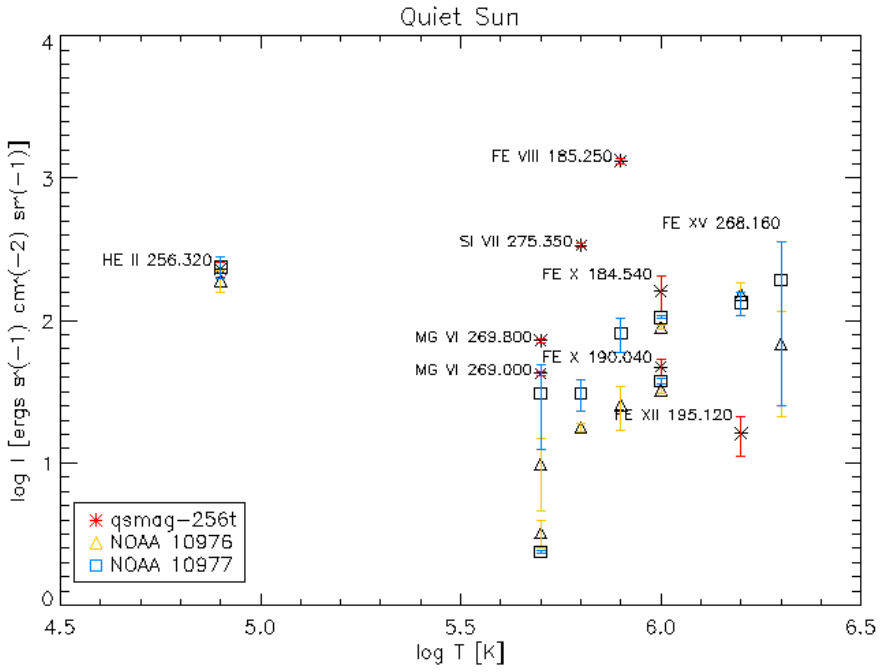

Figure 5.1: Mean intensity versus temperature for quiet Sun intensities. The standard deviation is shown in red for the qsmag-256t run, in yellow for NOAA 10976 and in blue for NOAA 10977. where the standard deviation is in the respective color. The mean intensity for Fe XV 268.160 Å is very low for the simulated quiet Sun intensities and falls below the lower range of this plot; $\log I = -2.07$ ergs $\mathrm{s}^{-1}\mathrm{cm}^{-2}\mathrm{sr}^{-1}$ with a standard deviation of $\log \sigma = -2.26$.

CHIANTI predicts that the Fe XIV 270.520 Å line is twice as strong as the Mg VI 270.3906 Å line. We therefore choose not to include the line of Mg VI 269.800 Å in the comparison of the EIS observations and the OSC results.

Continuing on with the upper transition region line Si VII 275.350 Å ($\log T = 5.7$), we observe that the synthetic intensity from the simulation is over ten times larger than the observed intensities. The difference in intensity between the observations of NOAA 10976 and 10977 is small, where NOAA 10977 is to some extent stronger.

The synthetic intensity from the Fe VIII 185.250 Å line is much stronger than the one emerging from the observations, where we observe a maximum of $\sim 10^3$ ergs $\mathrm{s}^{-1}\mathrm{cm}^{-2}\mathrm{sr}^{-1}$ difference. The synthetic intensity of the Fe VIII 185.250 Å line is the strongest quiet Sun intensity line observed. The mean

intensity plotted here is 1321.42 ergs $s^{-1}cm^{-2}sr^{-1}$, where as CHIANTI predicts a quiet Sun intensity of 42.3 ergs $s^{-1}cm^{-2}sr^{-1}$.

The spectral line intensities of Fe X 184.540 Å and Fe X 190.040 Å are similar in strength when comparing the simulations and the observations.We see that the synthetic intensities are somewhat stronger than the observed intensities.

Observations show that intensities from NOAA 10977 are stronger than the intensities of NOAA 10976.
Up to this point (*i.e.* Fe XII formed at $\log T = 6.2$) the synthetic intensities are stronger than the observed ones, this trend changes when we reach the temperatures needed to form Fe XII 195.120 Å. We see that the observed quiet Sun intensities for NOAA 10977 and NOAA 10977 are approximately identical with an intensity of $\log\langle I\rangle \approx 2.1$ ergs $s^{-1}cm^{-2}sr^{-1}$, at the same time as the synthetic intensity from the OSC is an order of magnitude smaller.

The synthetic intensity is also smaller than the observed intensity for the

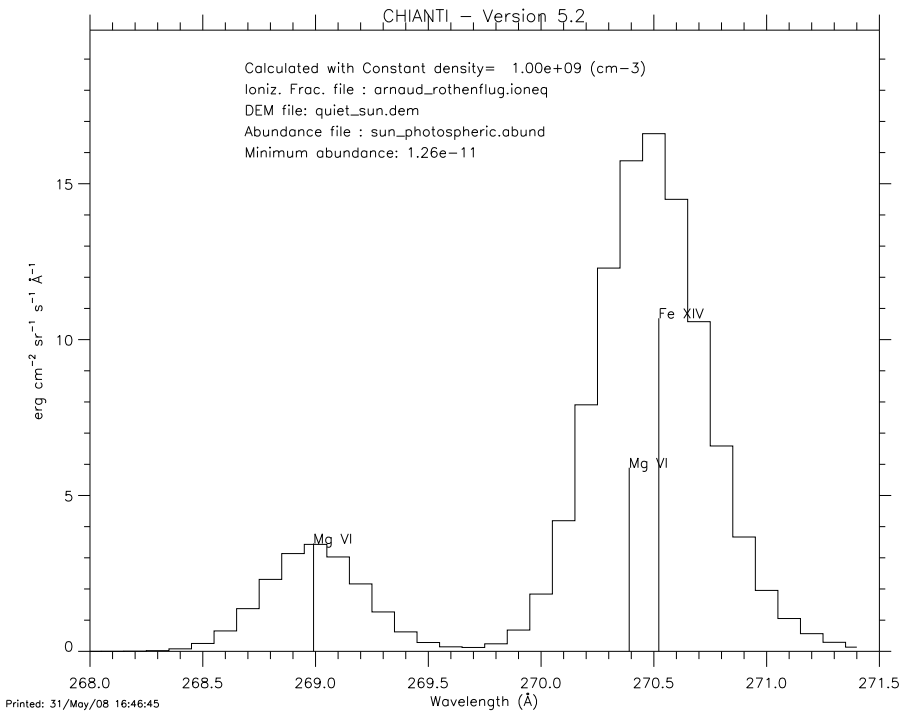

Figure 5.2: The observed spectral lines of Mg VI 260.000 Å and Mg VI 369.800 Å, as predicted by CHIANTI. CHIANTI data show that the observed line of Mg 369.800 Å is a blend of the theoretical lines Mg VI 270.3906 Å and Fe XIV 270.520 Å, as suspected due to observed Mg 369.800 Å intensities.

Fe XV 268.160 Å line. The standard deviations from the observed intensities are large. The synthetic intensity is underestimated by ∼4 orders of magnitude.

5.1.2 Active region

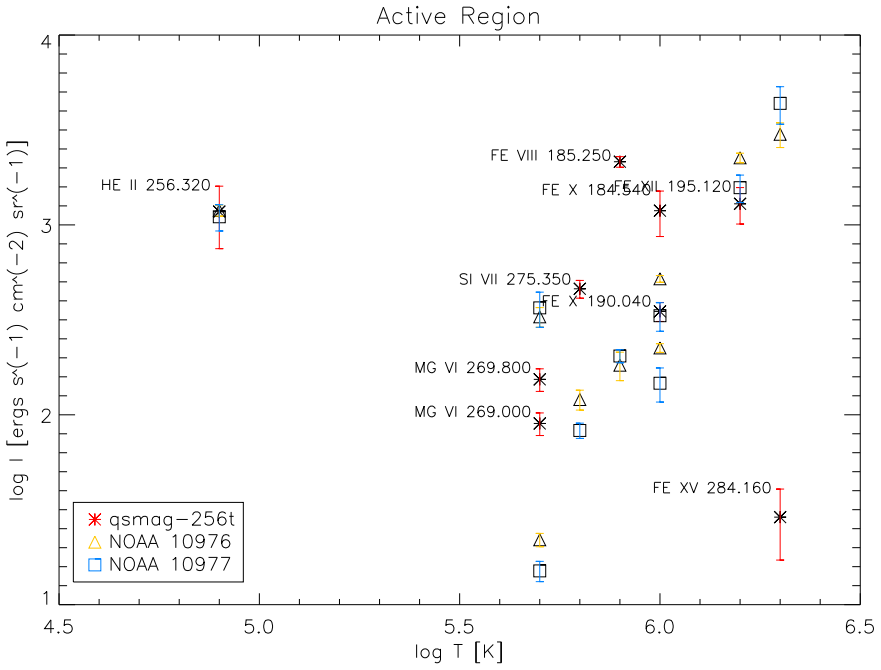

Figure 5.3: Mean intensity versus temperature for active region intensities.

Figure 5.3 displays the intensities from the active regions NOAA 10976 and NOAA 10977, as well as the active region values from the run qsmag-256t from the OSC.

We observe that the He 256.320 Å intensity is approximately the same for NOAA 10976, NOAA 10977 and qsmag-256t, with an intensity value of $\sim 10^3$ ergs $s^{-1}cm^{-2}sr^{-1}$. The standard deviation for the qsmag-256t run is quite large because of the active region peak as displayed in the upper frame of figure 4.4 of the active region curve. The intensities from the EIS observations, including their standard deviations, fall within the standard deviation of the OSC He 256.320 Å intensity, showing that the OSC is a good representation for active regions in the solar atmosphere at temperatures needed to form the He 256.320 Å line ($\log T = 4.9$).

The Mg VI 269.800 Å intensity for the observations is 10 times stronger in the active region than the quiet Sun. The standard deviation of the

active region intensity is also smaller for the observations of NOAA 10976 and NOAA 10977, than for the quiet Sun regions. The simulations give only a factor 2 in intensity difference between the active region and quiet Sun values for this line. For the observations this difference is of a factor 10.

For the Mg VI 269.000 Å line there are no significant differences between the active region intensities and the quiet Sun intensities, as discussed in the previous section. The only difference is that the standard deviation is smaller for the active region for the EIS observations and larger for the OSC simulations.

In the observations of NOAA 10976 and NOAA 10977 we see a difference of $\log\langle I\rangle \approx 2.5$ ergs $s^{-1}cm^{-2}sr^{-1}$ in intensity between the Mg VI 269.800 Å line and the Mg VI 269.000 Å line. The Mg VI 269.800 Å line is similar in intensity for the different NOAAs, with a intensity of ~ 345 ergs $s^{-1}cm^{-2}sr^{-1}$. The Mg VI 269.000 Å line intensity is also similar between the NOAAs, with a value of ~ 20 ergs $s^{-1}cm^{-2}sr^{-1}$.

As earlier, CHIANTI predicts that the Mg VI 269.800 Å line should be 1.7 times larger than the Mg VI 269.000 Å line, which is approximately what we get from the simulations of the active region intensities. This agreement is not the case for the observations, where the difference is $\sim$15 for NOAA 10976 and $\sim$ 24 for NOAA 10977. This makes our suspicion of a blend between the Mg VI 269.800 Å line and the Fe XIV 270.520 Å line in the observations mentioned earlier stronger. The Fe XIV 270.520 Å line is created at temperatures of $\log T = 6.2$. This line is therfore a corona line and will emit strongly in an active region. This blend may be way the Mg VI 269.800 Å line is so much stronger in the active region. Because of this we choose not to include it in the comparison.

The synthetic intensity of the Si VII 275.350 Å line is about an order of magnitude larger than the observed intensities of NOAA 10976 and NOAA 10977, while the intensity difference between the two active regiond is small. We also see that the synthetic intensity of this line has not increased significantly in the active region. Notice that the quiet Sun intensity of NOAA 10976 is smaller than the quiet Sun intensity of NOAA 10977, this is the opposite case in the active region, where the NOAA 10976 intensity of this line is 7 times larger, while the NOAA 10976 intensity have only increased by a factor of 3.

For the Fe VIII 185.250 Å line we observe that the synthetic intensity emerging from the active region is more than 10 times the intensities emerging from the EIS observations of NOAA 10976 and NOAA 10977, which is also the case for the quiet Sun intensities. As for the Si VII 275.350 Å line, the active region intensity for NOAA 10976 is much stronger than the active region intensity of NOAA 10977. The quiet Sun to active region intensity difference are a factor of 3 and 7 for NOAA 10977 and NOAA 10976, respectively.

The synthetic intensity of the Fe X 184.540 Å line is 7 times greater in

the active region than the quiet Sun region, as discussed in the previous section. This is the case for the NOAA 10976 intensity as well, the intensity is only a factor of 3 greater for NOAA 10977. We observe that the values of intensities from this line are more spread out, compared to the quiet Sun values. We observe that NOAA 10976 is stronger in active region intensity for this line as well, when compared to the NOAA 10977 intensity.

Because the lines Fe X 184.540 Å and Fe X 190.040 Å are formed at the same temperature of $\log T = 6.0$, it might be difficult to separate them from one another on the plot in figure 5.3. The three lower points$(*, \triangle, \diamond)$ at temperatrue $\log T = 6.0$ are the intensities of the Fe X 190.040 Å line.

We see that the synthetic intensity of the Fe X 190.040 Å line is similar to the observed intensity of the NOAA 10977 for the Fe X 184.540 Å line.

We observe that the intensities for the Fe X 190.040 Å line differ more from one another than the quiet Sun intensities, as displayed in figure 5.1. The active region intensities for NOAA 10976 are larger than the NOAA 10977 intensities, as for the other lines. The intensity difference between the EIS observations are similar in size as the difference between the simulated intensity and the closest EIS intensity. This shows that the OSC code is a good representation for the solar atmosphere when dealing with this spectral line.

For the Fe XII 195.120 Å line, the synthetic intensity from the OSC is smaller than the observed intensities from NOAA 10976 and NOAA 10977. We see that the intensity from the OSC is within the standard deviation of NOAA 10977, making the OSC intensity a good representation for real observations.

For the Fe XV 284.160 Å line on the other hand, the synthetic intensity is approximately 3 orders of magnitude smaller than the NOAA intensities, showing that the simulation might not reach the high temperature of $\log T = 6.3$ needed for the formation of the Fe XV 384.160 Å line. Thus we can not compare it to real observations.

5.2 Summary

If we summarize the contents of figure 5.1 and figure 5.3, it looks as if the atomic data provided by CHIANTI may be wrong for the Fe VIII 185.250 Å and the Si VII 275.350 Å lines, because these synthetic intensities are much larger than the observed ones. While most of the other lines are good approximations. The fact that these lines behave similarly for the active region as well, strengthens this suspicion.

We observe that most of the upper chromosphere and transition region lines are similar in intensity in NOAA 10976, NOAA 10977 and qsmag-256t. The intensity difference between the real observations from EIS and the synthetic intensity from the OSC is to a large extent similar to the intensity

difference between the EIS observations. This shows that the OSC code is a good representation for the solar atmosphere for the temperatures needed to procuse these lines.

The EIS observations for the corona lines Fe XII 195.120 Å and Fe XV 284.160 Å are much stronger in intensity than the synthetic observation from the OSC for quiet Sun intensities. While this effect disappears for the Fe XII 195.120 Å line when reaching active region intensities, it still remains for the Fe XV 284.160 Å line.

The reason for this may be that the simulation does not reach the temperatures needed to form these lines at a rate comparable to real observations for quiet Sun regions. In the active regions this effect disappears for the Fe XII 195.120 Å line, but is still visible for the Fe XV 284.160 Å line.

Chapter 6

Conclusion

6.1 Summary

Spectral line investigation may yield great insight. This thesis aim to compare intensities of transition region and corona spectral lines retrieved from real observations up against synthetic intensities from simulations. The observational data is provided using the EIS instrument onboard Hinode, while the synthetic data is results of three dimensional simulations of the solar atmosphere as provided by the OSC.

We choose a set of strong and well defined spectral lines from within the effective areas of the EIS spectral band for the analysis; He II 256.320 Å, Mg VI 269.000 Å, Mg VI 269.800 Å, Si VII 275.350 Å, Fe VIII 185.250 Å, Fe X 184.540 Å, Fe X 190.040 Å, Fe VII 195.120 Å and Fe XV 284.160 Å. These spectral lines cover a temperature range from $\log T = 4.9$ to $\log T = 6.3$, providing information about the solar atmosphere; transition region to corona.

The emergent intensity maps show many interesting features of the solar transition region and corona.

With a temperature of $\log T = 4.9$, the He II 256.320 Å line is the coolest line investigated. Intensity maps of this ion show aspects typical both for the chromosphere and the overlying corona. The dimmer quiet Sun regions display structures with spatial scales typical of the supergranular network. Comparison with SOT observations of the underlying magnetic field and upper photospere show that the He II emission is bright where the magnetic field in the underlying photoshere is strong. Active regions, named NOAA 10976 and NOAA 10977, clearly stand out as regions of high intensity, directly above the area of high magnetic field measured in the photosphere. These bright regions are clearly distinguishable from the supergranular structure in the quiet Sun.

As the line formation temperatures rises the supergranular pattern fades,

and is almost non-present in the Mg VI lines which are formed at $\log T = 5.7$. Because these lines are relatively weak, the active regions of NOAA 10976 and NOAA 10977 are the only regions with clearly evident structures. The transition region lines of Si VII 275.350 Å and Fe VIII 185.250 Å, formed at $\log T = 5.8$ and $\log T = 5.9$, are much stronger in intensity. Intensity maps of these line show no evidence of a granular pattern. Instead the active regions are bright and clear, showing loops of high intensity stretching from one side of the active region to the other. These structures increase in intensity for the corona lines of Fe VII 195.120 Å and Fe XV 284.160 Å.

The intensity maps are used to select areas of quiet Sun and active regions. Following this selection plots of the intensity structure as a function of time are made for the respective spectral lines. The following results show that the intensity emerging from the quiet Sun regions are constant in time for all the spectral lines investigated, even though the intensity values might not be the same for the different lines. The intensities emerging from the active region show variations over short time periods, while the overall tendency show a smooth decrease in the intensity over the entire observation-period. This intensity structure is evident in all the observed spectral lines of both NOAA 10976 and NOAA 10977.

The results of the OSC shows a synthetic solar atmosphere; from the upper convection zone to the lower corona.

The lower 2 Mm of the model contains the convection zone. Above this we find the photosphere where the temperature drops rapidly as radiation escapes freely. The chromosphere stretches out some 2 Mm to the bottom of the transition region, where the temperature rises rapidly to coronal values of some 10^6 K over a few thousand kilometers.

Observing the temperature structures in both the vertical and the horizontal directions give us information about the temperature behavior in the different layers of the atmosphere. The most evident futures are the steep temperature changes between the different layers. High temperature variations results in the chromosphere varying in size between 1 Mm to 3 Mm. These variations show themself as arcs in the chromosphere-corona division (the transition region). Investigating the magnetic field of this region, show magnetic field lines following these arcs. The footpoints of the magnetic field lines are located at regions where the corona extend down to low heights. Low temperature loops can be found at great heights, following the magnetic field lines from the chromosphere. This may be to cold, charged ions from the chromosphere being trapped along the field lines due to the Lorentz force, carrying the gas up to the corona.

The intensities of the respective lines are calculated using temperature and density values from the simulation as well as atomic data provided by CHIANTI.

Intensity maps of the synthetic data give us a overview of the intensity

distribution of the different lines over the area simulated. We observe that the intensity distribution to some extent follows the magnetic field of the simulation. The highest intensity is emitted furthest away from the underlying magnetic poles of opposite polarity in the simulation. The temperature range covered at from $\log T = 4.9$ to $\log T = 6.3$. When observing the intensity maps from the lowest temperature for the He II line, to the highest, represented by the Fe XV line, we see that the intensities display many structures.

As the temperature increase these structures seem to fade, displaying the intensity structures aligned to the magnetic field more clearly, showing footpoints of the underlying magnetic loops.

For each intensity map an active region and a quiet Sun region is defined. The mean intensities of these regions are plotted as a function of time, for each spectral line. These intensity structures display the same characteristics as the results from the EIS observations. All the spectral lines give a approximately constant quiet Sun intensity. The active region intensities are all varying in intensity over time. We observe that the active region intensities display several peaks over time. Such intensity peaks evident at low temperatures, emerge at later times for spectral lines of higher temperatures. We observe a displacement in time for the peak as the creation temperature of the spectral line increase.

For the comparison of the intensities emerging from the OSC data and the observational data from EIS we make log-log plots of intensities versus the creation temperatures of the spectral lines. For the He 256.320 Å line($\log T = 4.9$) the synthetic intensity is a very good match for the observed intensities for both quiet Sun and active region values. We discover that the Mg VI 269.800 Å line observed by EIS is a blend, and is therefore excluded from the comparison. The following spectral lines Mg VI 269.000 Å ($\log T = 5.7$), Si VII 275.350 Å($\log T = 5.8$) and Fe VII 195.250 Å ($\log T = 5.9$) show great intensity difference between the observations and the synthetic values. The reason for this may that some fundamental physical process is missing in the OSC numerical model or it could be caused by erroneous atomic data in CHIANTI. The synthetic intensities from the OSC are over two orders of magnitude larger than the EIS intensities.

The quiet Sun and the active region intensities from the OSC for the Fe X lines are good representations for the observed intensities. We observe that the synthetic intensity is somewhat stronger than the observed values. The quiet Sun intensities for NOAA 10977 are stronger than the NOAA 10976 intensities, while the active region intensities are stronger for NOAA 10976 than for NOAA 10977. This is still a good representation, because the intensity difference between the two NOAA observations is similar to the intensity difference between the synthetic intensity and the highest observed intensity.

For quiet Sun intensities, the EIS observations of the corona lines Fe XII 195.120 Å and Fe XV 284.160 Å are much stronger than the synthetic intensity from the OSC. While this effect disappears for the Fe XII 195.120 Å line when reaching active region intensities, it still remains for the Fe XV 284.160 Å line.

The reason for this may be that the simulation does not reach the temperatures needed to form these lines at a rate comparable to real observations for quiet Sun regions. In the active regions this effect disappears for the Fe XII 195.120 Å line, but is still visible for the Fe XV 284.160 Å line.

6.2 Further work

Still more work is needed to get a proper intensity comparison of the real observations as provided by EIS and the OSC. As we have discussed so fare, there are some deviations for the spectral lines of Mg VI 269.000 Å, Si VII 275.350 Å and Fe VII 195.250 Å. The suspicion of atomic data errors due to CHIANTI contributions have to be investigated. Abundance and ionization rates for these lines should be recalculated, and the comparison redone.

We also observed that the synthetic intensity values for the corona lines of Fe XII 195.120 Å and Fe XV 284.160 Å grew over time. The simulation should be run for a longer time period, to observe if this intensity increase continues or stabilizes. The fact that the Fe XII and Fe XV intensities does not reach the observed quiet Sun intensities, while this significantly improves for the active region, indicates that the OSC does not reach the temperatures needed for producing these lines.

A better basis for comparison between real and synthetic observations may be to include more spectral lines from within the EIS spectral bands, specially in the temperature gap between $\log T = 4.9$ and $\log T = 5.7$. This may yield enough data point for a DEM analysis, which will give a better foundations for comparing.

For a better basis of comparison of the data from EIS and the OSC it would be conveniet to also studie other properties of the emergent spectral lines, such as doppler shifts, to get a better insight of the behaviour of the atmospheric gasses of the solar atmosphere.

Bibliography

Arnaud, M. and Rothenflug, R. (1985). An updated evaluation of recombination and ionization rates. *Astron. Astrophys. Suppl. Ser.*, 60:425–457.

Aschwanden, M. J. (2004). *Physics of the Solar Corona. An Introduction.* Physics of the Solar Corona.

Culhane, J. L., Harra, L. K., James, A. M., Al-Janabi, K., Bradley, L. J., Chaudry, R. A., Rees, K., Tandy, J. A., Thomas, P., Whillock, M. C. R., Winter, B., Doschek, G. A., Korendyke, C. M., Brown, C. M., Myers, S., Mariska, J., Seely, J., Lang, J., Kent, B. J., Shaughnessy, B. M., Young, P. R., Simnett, G. M., Castelli, C. M., Mahmoud, S., Mapson-Menard, H., Probyn, B. J., Thomas, R. J., Davila, J., Dere, K., Windt, D., Shea, J., Hagood, R., Moye, R., Hara, H., Watanabe, T., Matsuzaki, K., Kosugi, T., Hansteen, V., and Wikstol, Ø. (2007). The EUV Imaging Spectrometer for Hinode. *Solar Physics*, 243:19–61.

Grevesse, N., Noels, A., and Sauval, A. J. (1996). Standard Abundances. In Holt, S. S. and Sonneborn, G., editors, *Cosmic Abundances*, volume 99 of *Astronomical Society of the Pacific Conference Series*, pages 117–+.

Hansteen, V. H., Carlsson, M., and Gudiksen, B. (2007). 3D Numerical Models of the Chromosphere, Transition Region, and Corona. In Heinzel, P., Dorotovič, I., and Rutten, R. J., editors, *The Physics of Chromospheric Plasmas*, volume 368 of *Astronomical Society of the Pacific Conference Series*, pages 107–+.

Hansteen, V. H. and Gudiksen, B. (2005). 3D Numerical Models of Quiet Sun Coronal Heating. In *Solar Wind 11/SOHO 16, Connecting Sun and Heliosphere*, volume 592 of *ESA Special Publication*.

Hebb, M. H. and Menzel, D. H. (1940). Physical Processes in Gaseous Nebulae. X. Collisional Excitation of Nebulium. *Astrophysical Journal*, 92:408–+.

Hyman, A. (1976). *Computing. A dictionary of terms, concepts and ideas.* Arrow Reference Series, London: Arrow Books, 1976.

Kitchin, C. R. (2003). *Astrophysical techniques.* Astrophysical techniques, by C.R. Kitchin. 4th ed. Bristol; Philadelphia: Institute of Physics Publishing, 2003.

Kosugi, T., Matsuzaki, K., Sakao, T., Shimizu, T., Sone, Y., Tachikawa, S., Hashimoto, T., Minesugi, K., Ohnishi, A., Yamada, T., Tsuneta, S., Hara, H., Ichimoto, K., Suematsu, Y., Shimojo, M., Watanabe, T., Shimada, S., Davis, J. M., Hill, L. D., Owens, J. K., Title, A. M., Culhane, J. L., Harra, L. K., Doschek, G. A., and Golub, L. (2007). The Hinode (Solar-B) Mission: An Overview. *Solar Phys.*, 243:3–17.

Landi, E., Del Zanna, G., Young, P. R., Dere, K. P., Mason, H. E., and Landini, M. (2006). CHIANTI-An Atomic Database for Emission Lines. VII. New Data for X-Rays and Other Improvements. *apJS*, 162:261–280.

Lang, K. R. (1999). *Astrophysical formulae.* Astrophysical formulae / K.R. Lang. New York : Springer, 1999. (Astronomy and astrophysics library,ISSN0941-7834).

Mariska, J. T. (1992). *The solar transition region.* Cambridge Astrophysics Series, New York: Cambridge University Press, |c1992.

Mihalas, D. (1978). *Stellar atmospheres /2nd edition/.* San Francisco, W. H. Freeman and Co., 1978. 650 p.

Nordlund, A. (1982). Numerical simulations of the solar granulation. I - Basic equations and methods. *Astronomy and Astrophysics*, 107:1–10.

Nordlund, Å. and Galsgaard, K. (1995). A 3D MHD code for parallel Computers. http://www.astro.ku.dk/ kg.

Ostlie, D. A. and Carroll, B. W. (2007). *An Introduction to Modern Stellar Astrophysics /2nd edition/.* An Introduction to Modern Stellar Astrophysics, by D.A. Ostlie and B.W. Carroll. Benjamin Cummings, 1996. ISBN 0-321-44284-9.

Press, W. H., Teukolsky, S. A., Vetterling, W. T., and Flannery, B. P. (1992). *Numerical recipes in FORTRAN. The art of scientific computing.* Cambridge: University Press, |c1992, 2nd ed.

Skartlien, R. (2000). A Multigroup Method for Radiation with Scattering in Three-Dimensional Hydrodynamic Simulations. *Astrophysical Journal*, 536:465–480.

Skogvoll, M. E. (2007). Hinode/eis spectroscopy and modeling. Solar physics, Institute of Theoretical Astrophysics, Univerity of Oslo.

Windt, D. L., Donguy, S., Seely, J. F., Kjornrattanawanich, B., Gullikson, E. M., Walton, C. C., Golub, L., and DeLuca, E. (2004). EUV multilayers for solar physics. In Citterio, O. and O'Dell, S. L., editors, *Optics for EUV, X-Ray, and Gamma-Ray Astronomy. Edited by Citterio, Oberto; O'Dell, Stephen L. Proceedings of the SPIE, Volume 5168, pp. 1-11 (2004).*, volume 5168 of *Presented at the Society of Photo-Optical Instrumentation Engineers (SPIE) Conference*, pages 1–11.